UNIVERSITY OF CALIFORNIA,
IRVINE

Modeling Connectivity in Multi-trial Brain Signals

DISSERTATION

submitted in partial satisfaction of the requirements
for the degree of

DOCTOR OF PHILOSOPHY

in Statistics

by

Lechuan Hu

Dissertation Committee:
Professor Michele Guindani, Chair
Professor Hernando Ombao
Associate Professor Yaming Yu
Associate Professor Zhaoxia Yu

2018

DEDICATION

To my mom and dad

TABLE OF CONTENTS

LIST OF FIGURES

LIST OF TABLES

LIST OF ALGORITHMS

ACKNOWLEDGMENTS

I would like to express my sincere gratitude to my advisors, Professor Michele Guindani and Professor Hernando Ombao, who have always been supportive of my study and research. Without their guidance this dissertation would not have been possible.

Besides my advisors, I would like to thank the rest of my thesis committee: Professor Yaming Yu and Professor Zhaoxia Yu, who have taught me many basic and important topics in statistics that have since greatly benefited my research. I would also like to thank Professor Norbert J. Fortin, who kindly provides the LFP data and shares his knowledge in the neuroscience field.

This work is supported by UCI Department of Statistics and the grants from the US NSF Division of Mathematical Sciences.

CURRICULUM VITAE

Lechuan Hu

EDUCATION

Doctor of Philosophy in Statistics **2018**
University of California, Irvine *Irvine, CA*

Master of Science in Statistics **2015**
University of California, Irvine *Irvine, CA*

Bachelor of Science in Applied Mathematics **2013**
Fudan University *Shanghai, China*

RESEARCH EXPERIENCE

Graduate Research Assistant **Jun,2014–Jul,2018**
University of California, Irvine *Irvine, CA*

TEACHING EXPERIENCE

Teaching Assistant **Jan,2017–Jul,2018**
University of California, Irvine *Irvine, CA*

WORK EXPERIENCE

Data Scientist Intern **Jun–Sep,2017**
Liberty Mutual Insurance *Boston, MA*

REFEREED JOURNAL PUBLICATIONS

Modeling High-Dimensional Multichannel Brain Signals **2017**
Statistics in Biosciences

ABSTRACT OF THE DISSERTATION

Modeling Connectivity in Multi-trial Brain Signals

By

Lechuan Hu

Doctor of Philosophy in Statistics

University of California, Irvine, 2018

Professor Michele Guindani, Chair

The hippocampus is critical to memory consolidation. To study the underlying neuronal mechanisms of hippocampus in sequential memory, we consider an experiment recording multi-trial local field potentials (LFPs) from hippocampal region CA1 of rats that performed a complex sequence of memory tasks in different experimental conditions. Our work aims at (1.) modeling and measuring functional and effective (directional) connectivity in multi-channel LFP data; (2.) quantifying and differentiating connectivity in rats hippocampus at condition-level in order to study heterogeneous hippocampal functions. Our work addresses multiple statistical and computational challenges for modeling and analyzing multi-channel LFPs since the parameter space is usually high dimensional. Also, our contribution allows to measure the effective connectivity between channels in frequency domain with inferring directionality. Thirdly, we successfully incorporate within-conditions connectivity similarity with between-conditions connectivity heterogeneity in modeling and provide a natural way to conduct trial- and condition-level inference on effective connectivity.

To model multi-channel LFPs, we propose two approaches. The first one is to fit a vector autoregressive (VAR) model with potentially high lag order so that complex lead-lag temporal dynamics between the channels can be captured. Estimates of the VAR model will be obtained by our proposed hybrid LASSLE (LASSO+LSE) method which combines regulariza-

tion (to control for sparsity) and least squares estimation (to improve bias and mean-squared error). One of the novelties of our approach is the use of a frequency-specific measure, partial directed coherence (PDC), to characterize effective connectivity. More specifically, PDC allows us to infer directionality and explain the extent to which the present oscillatory activity at certain frequency in a sender channel influences the future oscillatory activity in a specific receiver channel relative to all possible receivers in the brain network.

The second approach is using a Bayesian hierarchical vector autoregressive (BH-VAR) model to characterize brain connectivity and make inference on the difference of connectivity across experimental conditions. Within-conditions connectivity similarity and between-conditions connectivity heterogeneity are accounted by the priors on trial-specific models. In addition to the fully Bayesian framework, we also propose an alternative two-stage computation approach which still allows straightforward uncertainty quantification of between-trial conditions via MCMC posterior sampling, but provides a fast approximate procedure for the estimation of trial-specific VAR parameters.

Our proposed approaches provided key insights into both trial- and condition-level hippocampal connectivity among simultaneously recorded sites during performance of rats in a complex memory task. Specifically, this novel method was successful in quantifying patterns of effective connectivity across electrode locations, and in capturing how these patterns varied across trial epochs and trial types.

Chapter 1

Introduction

1.1 Scientific Background

The hippocampus is a critical component of brains for memory formation. It is involved in certain kinds of memory – short-term memory, long-term memory and memory for sequence of events. Attention to the hippocampal function was raised by a number of patients, who suffered severe neurological and memory diseases such as Alzheimers disease, short-term memory loss and disorientation. However, the neuronal mechanisms underlying hippocampal function is still elusive. Connectivity between populations of neurons in the hippocampus could be implicated in hippocampal function [37]. To address how the hippocampal activity influences the memory for sequence of events, our collaborators in the Fortin Laboratory (UC Irvine) conducted complex non-spatial sequence memory tasks of rats since there is strong memory behavioral parallels in rats and humans [1]. In their experiments, rats were presented with repeated sequences of odors in two different conditions - "in sequence" (InSeq) and "out of sequence" (OutSeq), and were required to make a judgment whether each odor was presented "in sequence" or "out of sequence". Multi-trial neural activity signals (including

local field potentials) were recorded from tetrodes located in rat's hippocampal region CA1.

Motivated by our collaborators, this dissertation will focus on studying the hippocampal connectivity in a particular type of brain electrophysiological data: local field potentials (LFPs). LFP signals are being widely used in learning and memory experiments of animals along with electroencephalograms (EEGs) [6, 40, 51]. They both have excellent temporal resolution (e.g., LFPs in this study are 1000 observations per second activity of the neurons). However, LFPs are recorded invasively as these are obtained from electrodes that are chronically implanted inside the brain. Consequently they have less non-neuronal physiological activity (e.g., from muscle movement and eye movement artifacts) compared to scalp EEGs and therefore possess a higher signal-to-physiological-noise ratio. One disadvantage of LFPs is its limited utility in humans due to its invasive nature. However, this doesn't affect the consideration that LFPs continue to be a valuable tool for investigating brain function in animals which can then provide useful information for modeling brain function in humans.

To characterize the underlying hippocampal connectivity, we will fit statistical models to the LFPs. One of the major challenges is that the parameter space of models can be potentially high dimensional. This is because the number of recording tetrodes (P) in multi-channel LFPs can range from 8-100, and the temporal order (d) of parametric models such as vector autoregressive models needs to be sufficiently large in order to accurately capture the dynamics in these complex hippocampal processes. The number of parameters in this setting is P^2d, which can be large and consequently leads to intensive computation. Another modeling challenge comes from the need that the fitted statistical models must be able to characterize complex hippocampal connectivity both across trials and experimental conditions. This is because heterogeneous temporal patterns in the hippocampus were observed in memory consolidation for sequence of events (see Figure 1.1). Therefore we want to characterize the heterogeneity in hippocampal connectivity both within-conditions (trials) and between-conditions (InSeq and OutSeq). Besides these statistical and computational challenges, the

lack of universally-agreed measures for characterizing connectivity is also a problem. An appropriate measure in this study should indicate both the functional connectivity and effective (directional) connectivity in the hippocampus.

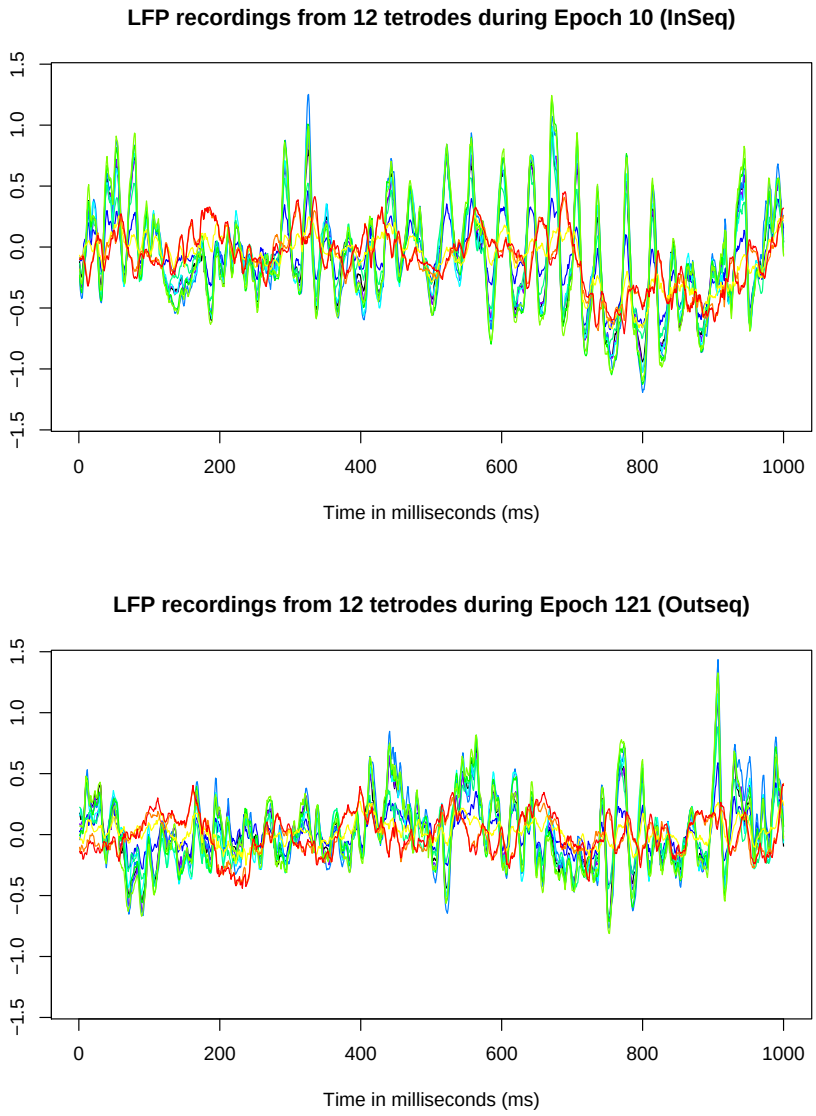

Figure 1.1: Local field potential (LFP) recordings of 12 tetrodes during one epoch (1000 milliseconds; $T = 1000$) from InSeq and OutSeq condition respectively. Each time series with color indicates the LFP recording of one tetrode. Different temporal patterns could be indication of heterogeneous hippocampal connectivity in these tetrodes across experimental conditions.

1.2 Current statistical approaches and limitations

1.2.1 Characterizing connectivity in a single trial

Connectivity in brain signals is actually the causal relation among simultaneously measured time series. One series is causal to the other one if better prediction of the second series can be achieved when incorporating the knowledge of the first one [53]. This concept was later developed and formalized in [21] with Granger-causality. We say brain signal from channel v "Granger-causes" signal from channel u if the past observations of channel v help improve predictions of channel u at future time points, compared with predictions based on the past of channel u alone. Granger-causality recognizes the importance of temporal ordering in the context of linear regression models of complex brain processes. A common approach to characterize Granger-causal relation in a multichannel LFP signal of a single trial is the vector autoregressive (VAR) model [46]. A P-dimensional brain signal $\mathbf{X}_t$ is said to follow a VAR model of order d, denoted VAR(d), if it has the representation

$$\mathbf{X}_t \;=\; \Phi_1\mathbf{X}_{t-1} + \ldots + \Phi_d\mathbf{X}_{t-d} + \varepsilon_t \quad t = d+1, ..., T \tag{1.2.1}$$

Φ_ℓ's $\in \mathfrak{R}^{P\times P}$ are the autoregressive coefficient matrices. $\varepsilon_t \overset{iid}{\sim} N_P(\overrightarrow{0}, \Sigma)$ is Gaussian noise. The interconnectivity between channels is determined by the autoregressive coefficient matrices $\{\Phi_\ell\}_{\ell=1}^d$ and spatial covariance matrix Σ. The VAR model provides a broad framework for capturing complex temporal and cross-sectional interrelationship among brain time series signals (in particular, directionality of frequency-specific connectivity). Consequently it can be applied to model the Granger-causal relation between channels [28].

An illustration of how VAR matrices capture the connectivity among brain channels can be found in Figure 1.2. Denote the single trial LFP traces of hippocampal region to be u-th and v-th channel. Then Φ_ℓ^{uv}, which is the (u, v) entry of VAR matrix Φ_ℓ, shows the impact

of input signal from v-th channel at past time point $t-\ell$ to brain activity at u-th channel at current time point t. Φ_ℓ^{uv} is not necessarily equal to Φ_ℓ^{vu}, because impact of one channel on the other channel could be different the other way around. Therefore the connectivity characterized by VAR matrices is directional. If $\Phi_\ell^{uv}=0$ and $\Phi_\ell^{vu}=0$ for all lags ℓ then, there is no causal relation between these two channels as determined by VAR model. A positive value indicates that the signal of v-th channel at time $t-\ell$, conditional on LFP values at other time points, has positive linear dependence with u-th channel at time t. That is, a marginal increase in activity in v-th channel leads to an increased future activity in u-th channel. Thus, the entries of $\{\Phi_\ell\}_{\ell=1}^d$ contain the information of brain effective connectivity between channels.

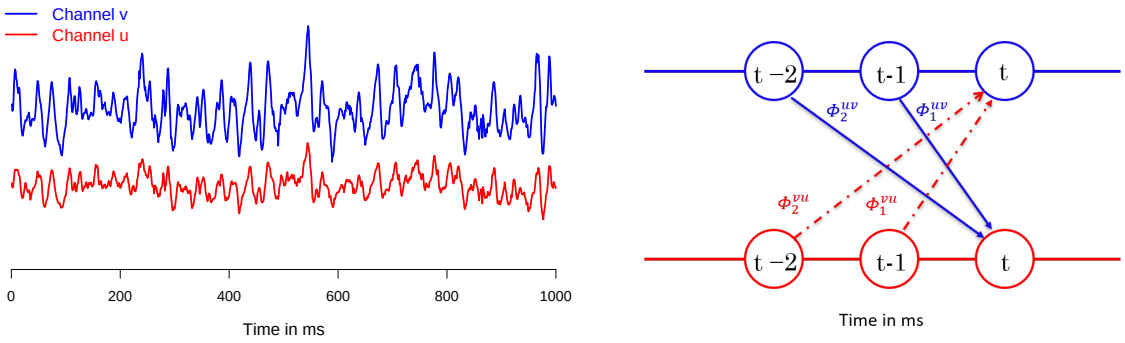

(a) LFP traces (b) Explicit connectivity in VAR

Figure 1.2: Illustration of VAR model. Φ_ℓ^{uv} $(\ell=1,2)$ captures the impact of the input from v-th channel at time $t-\ell$ to brain activity at u-th channel at the current time t.

As noted above, to investigate the effective connectivity between channels actually requires the knowledge of the VAR coefficient matrices. However, this is challenging as the parameter space of a VAR model for brain signals could be potentially high. For example, a fitted VAR(10) model to LFPs from 12 channels or tetrodes has $10\times 12^2=1440$ parameters in total to estimate, which subsequently require intensive computation. One may suggest fitting a model with low temporal lag d in order to reduce the number of parameters. The problem with this suggestion, unfortunately, is that a low temporal order might miss potentially

important features of the LFP data such as multiple peaks in the spectra. One classic estimation approach is via least squares which provides unbiased estimator for the elements of the VAR coefficient matrices but at the cost of high demand of computing. The least squares estimate (LSE) does not possess the specificity for coefficients with true value of zero. Hence, LSE estimation cannot identify the causal relation between channels as well as the functional connectivity structure in the hippocampus. Another common estimation approach is the LASSO (least absolute shrinkage and selection operator) method which is a particular representative of the penalized regression family [50, 16, 54, 23]. Compared with LSE, the LASSO approach requires shorter computation time [34]. Most importantly, LASSO has higher specificity of zero-coefficients. The main limitation of the LASSO (and most regularization methods) is that the estimators of the non-zero coefficients are biased. Thus, LASSO could lead to misleading results when investigating strength of brain effective connectivity. Due to these unavoidable drawbacks, classic estimating approaches are not ideal options to solve VAR modeling for high dimensional brain signals. Consequently a more scalable approach is in intense need to estimate connectivity in multi-channel brain signals.

1.2.2 Characterizing connectivity in multiple trials

Characterizing multi-trial LFPs is more complicated compared with single trial case. Figure 1.1 demonstrates an example of rat's LFPs recorded in two trials (here an epoch is 1 second time block) from InSeq and OutSeq respectively. Very different temporal pattern of LFPs can be observed from InSeq and OutSeq condition, which indicates potential variation of brain connectivity in hippocampal region across conditions/trials. Our question of interest, when characterizing multi-trial LFPs, is not only study the hippocampal connectivity at trial level but investigate its evolution at condition level. That is to say, we want to characterize the heterogeneity both within-conditions (trials) and between-conditions (InSeq and

OutSeq). To analyze multi-trial LFPs at condition level, two-stage approaches have generally been employed, in which a VAR model is fit on each individual trial and characterize trial-specific connectivity in the first stage, then condition-level connectivity and between-conditions variation are obtained in the second stage [10, 25]. Despite their common usage, there are several known drawbacks of two-stage approaches. First of all, the information of connectivity similarity within-conditions is missing. Connectivity in trials from the same condition should have common structure. However, this similarity is typically not taken into account during the parameter estimation procedure in the first stage, since trials from same experimental condition were modeled and estimated separately. Secondly, summarizing and making inference on the condition-level effective connectivity was accomplished via bootstrap analysis, where random variability at trail level was introduced but not accounted for by re-sampling residuals. To overcome these issues, a mixed-effects generalization of the usual VAR model was proposed in [20], which decomposes connectivity of multi-trial signals into condition-specific and trial-specific components. The problem of their approach is that there will be an explosion of number of parameters in the conditional maximum likelihood procedure, where complexity-penalized regression should have been introduced. In a Bayesian extension, those deficiency was addressed by charactering via Bayesian hierarchical vector autoregressive (BH-VAR) models, which allows for simultaneous inference on effective connectivity at both trial- and condition-level [9]. In addition, sparsity in VAR parameter space was induced at the condition level through "spike-and-spike" prior.

1.2.3 Measures of brain connectivity

There are different types of connectivity of interest in complex brain network study – structural connectivity, functional connectivity and effective connectivity. *Structural connectivity*, the set of structural connections between neuronal units at a given time, typically corresponds to white matter tracts between pairs of brain regions [44]. It is relatively stable at short

time scales (seconds to minutes), but can be dynamic in long time windows [48]. Graph theory is a popular method used in the analysis of structural connection pattern, which allows for the identification and classification of sub-networks of brain regions. The presence of an edge between two nodes in the graph indicates the presence of connection between the two corresponding channels. To measure structural connectivity, clustering coefficient and the characteristic path length in graph theory are frequently used, where the former one measures local structure and the latter one is global characteristic [49].

Functional connectivity, which captures patterns of deviations from statistical independence between channels, corresponds to magnitudes of brain temporal correlations in activity. It is time-dependent (hundreds of milliseconds) and usually measures statistical interdependence (e.g., correlation/covariance, spectral coherence) between channels without explicit relation to causal effects [48]. Estimates of functional connectivity don't depend on statistical models, but could differ across different methodologies for measuring brain activity [24]. A common dependency measure of functional connectivity is coherency, which can be interpreted as the cross-correlation between frequency oscillatory component in one channel and the frequency oscillatory component in another channel [41]. Coherence, another functional connectivity measure, is the squared value of coherency. When it is close to 1, both channels share a common frequency oscillatory activity. A large coherence value between two channels could be due to direct connectivity between these two channels or could be indirectly due to the intervening effect of other channel(s). Therefore we shall use partial coherence to measure the strength of functional connectivity between a pair of channels – with the effect of all intervening channels removed. Partial coherence is a measure of direct influence between two channels at frequency domain after the influence of all other channels has been controlled.

The third type of brain connectivity is *effective connectivity*, which refers to the causal influence of one neural unit over another [15]. It requires the specification of a causal model, for example VAR models. Therefore effective connectivity is not model-free. Unlike functional

connectivity, effective connectivity is a measure of directed information flow. That is to say, the connectivity from channel v to channel u is not the same as that from channel u to channel v. Particularly, we use partial directed coherence (PDC) to measure the effective connectivity for VAR models. Partial directed coherence was developed in [4] and refined in [5]. Consider a VAR(d) model given by Equation (1.2.1), partial directed coherence is the transform of sequence $\{\Phi_\ell\}_{\ell=1}^d$ at frequency ω. It measures the direct influence from channel v to channel u conditional on all the outflow from channel v. PDC gives an indication on the extent to which present frequency-specific oscillatory activity from a sender channel explains future oscillatory activity in a specific receiver channel relative to all channels in the network. In addition, PDC of a channel to itself indicates how much current oscillatory activity of a channel can be explained by its own past at certain frequency. Compared with measures of functional connectivity, the directionality of PDC is more specific and brings us more insights about the dynamic of information flow.

1.3 Proposed modeling and estimating approaches

1.3.1 Estimating and inference approach for a single trial

A scalable estimating procedure of VAR coefficients is the key to characterize connectivity in single trial LFPs, which requires both the specificity of zero/non-zero dependence and the sensitivity to the non-zero dependence strength. Inspired by the capability of each of the two classical estimating approaches (i.e., LSE and the LASSO), we propose to combine these in a two-step estimation procedure for the VAR coefficient matrices. We first apply LASSO to identify entries in VAR matrices whose estimates are not set 0, then we fit LSE with the constraint that "zero" entries estimates from step 1 are fixed to 0. Our method has inherited low bias for non-zero estimates and high specificity for zero-estimates from

LSE and the LASSO separately. As a result, the proposed two-step method has substantial higher specificity and significantly lower mean squared error (MSE) in the simulation study. Note that though LASSO aims to shrink many of the VAR coefficients to zero but this does not necessarily lead to a sparse connectivity structure. A pair of channels are functionally disconnected only if all of the its corresponding VAR coefficients at all lags are estimated to be zero. Thus, imposing sparsity on the VAR coefficient matrices helps to weed out the less important parameters in the VAR model but does not oversimplify the connectivity structure.

To make inference on effective connectivity of single trial, a natural idea is to derive the asymptotic property of the estimated VAR coefficients as well as the estimated connectivity. However, this is not trivial and in fact not solved yet given the regularization setting in estimating high dimensional VAR parameters. A substitute approach is that we can develop a bootstrap-based inference, which has been used in time series [42, 43, 29, 45, 31]. After obtaining the estimates of the VAR coefficients, we use these estimates and re-sampled residuals to generate new bootstrapped trials. The two-step method is re-applied to the generated time series, then new estimates of VAR coefficients and partial directed coherence are obtained. By repeating this procedure a sufficient large times, the empirical distribution of estimated connectivity is formed and consequently we can study the variation of connectivity.

1.3.2 Modeling and inference approach for multiple trials

As mentioned before, two-stage modeling approach has been adopted as a common method to characterize connectivity in multiple trials, which separates trail-specific connectivity in the first stage and condition-level connectivity in the second stage. To address the deficiencies of this method, we extend the Bayesian hierarchical vector autoregressive models by [9]

in this thesis and adapt some of its prior information to LFP data. We will characterize both trial- and condition-level hippocampal connectivity simultaneously in the hierarchical structure. By imposing condition-level priors on parameters in trial-specific models, we are able to incorporate within-conditions correlation with between-conditions variation. These information will help us better characterize trail- and condition-level connectivity by computing the posterior distribution. Moreover, inference on trial- and condition-level connectivity are made simultaneously with the posterior distribution, without introducing any additional uncertainty like two-stage approach.

Note the potential sparse structure in high dimensional parameter space of characterizing brain signals, sparsity in parameters could be induced via imposing variable selection priors (e.g., "spike-and-slab" mixture priors) on condition-level connectivity. Then Bayesian inference could be conducted on whether the parameters are truly sparse based on the knowledge from MCMC samplers. Moreover, this Bayesian framework allows us to directly make inference about the difference between hippocampal connectivity in different experimental conditions, of which the mean level and variation can be achieved from MCMC sampling.

1.4 Rat's non-spatial sequence memory study

To address the neuronal mechanisms underlying hippocampal function on sequence memory, our collaborators in the Fortin Laboratory at UCI recorded neural activity in hippocampal region CA1 of rats that performed a hippocampus-dependent sequence memory task. The task is clinically meaningful as this form of sequence memory shows strong behavioral parallels in rats and humans [1], and depends on the hippocampus for both species [13, 8], and is impaired in normal aging [2].

1.4.1 Experiment design

In the experiment (see Figure 1.3), rats were presented with repeated sequences of five odors in a single odor port. They were trained to identify whether each odor was presented "in sequence" (by holding their nose poke until the signal) or "out of sequence" (by withdrawing their nose poke before the signal) to receive a water reward. The LFP data included here was recorded from CA1 electrodes during a session in which a well-trained rat performed the task over 80% correctly across all training sessions before the experiment [3].

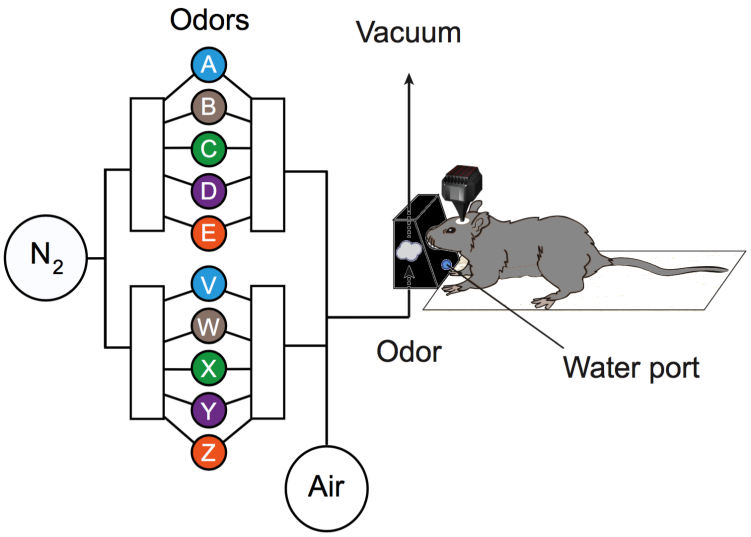

Figure 1.3: A non-spatial sequence memory experiment in rats. Rats were presented with repeated sequences of five odors (A,B,C,D and E) in a single odor port. Each odor presentation was initiated by a nose poke and rats were required to correctly identify the odor as either InSeq (ABCDE) by holding their nose poke until the signal or OutSeq (e.g.,ABDDE) by withdrawing their nose poke before the signal.

1.4.2 LFP data

Neural activity (including local field potentials) was recorded during each session. The full dataset includes LFPs from 23 tetrodes located in the hippocampus and $n = 247$ epochs. $n = 219$ epochs are "in sequence" and $n = 28$ epochs are "out of sequence". Each epoch

is recorded roughly 1 second with sampling frequency of 1000 Hz and thus has $T = 1000$ time points. Our analysis was specifically focused on LFPs from $P = 12$ tetrodes, a subset of electrodes that also recorded clear single-cell spiking activity and were confirmed to be located in the pyramidal layer of CA1 (see estimated tetrode locations in Figure 1.4). In addition, LFPs of Epoch 10 can be found in Figure 1.5. We observe that time series of LFPs from tetrode T13 to tetrode T23 have highly similar temporal pattern, while time series of the remaining tetrodes are highly similar. This is because tetrodes near each other are likely to behave more similarly than those that are far apart.

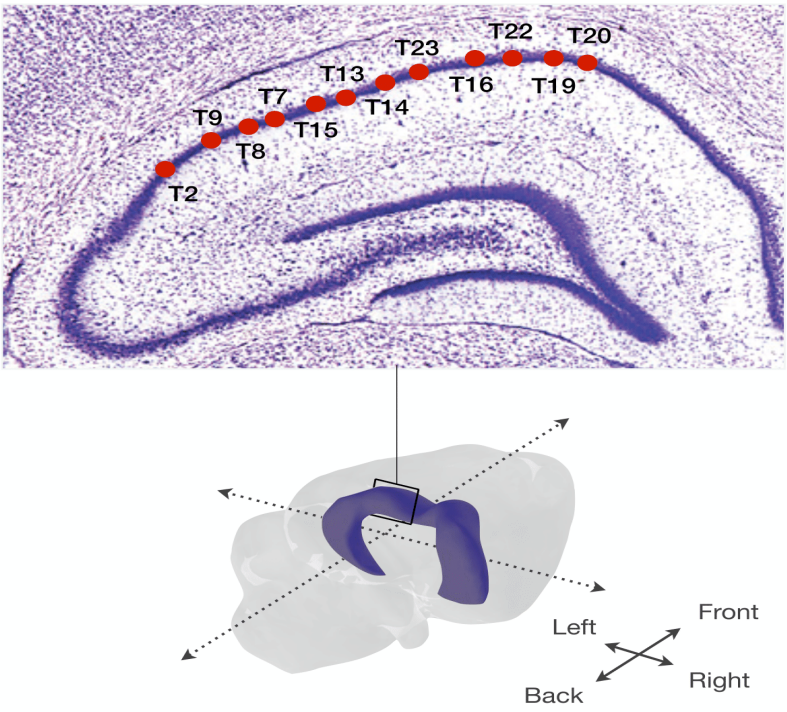

Figure 1.4: Estimated location within the hippocampus (dorsal CA1 region) of subset of 12 tetrodes included in the analyses.

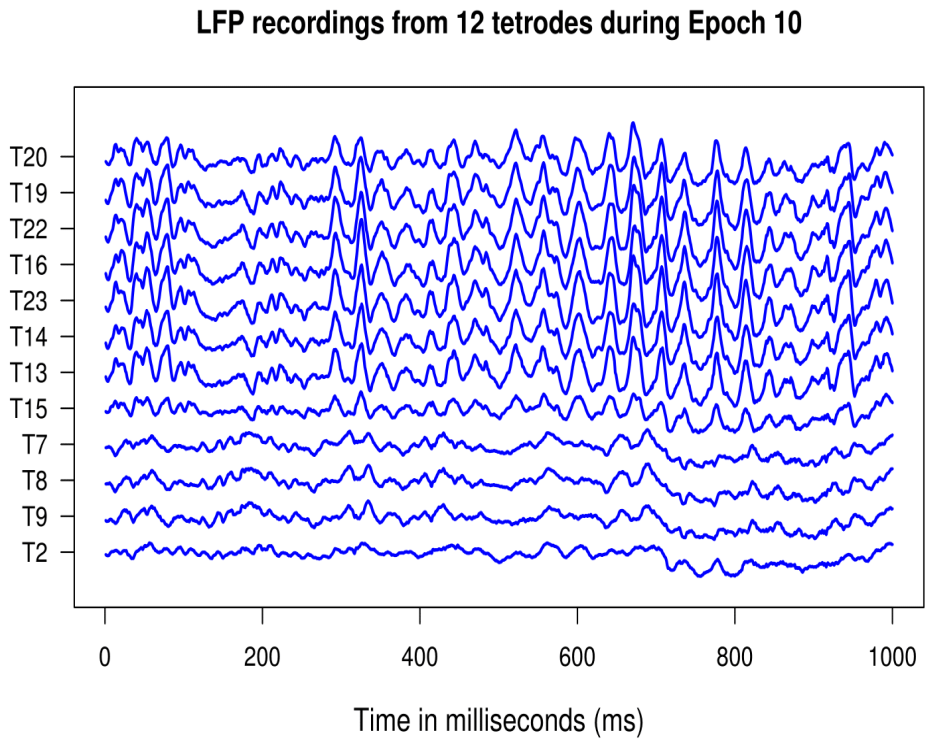

Figure 1.5: LFPs from 12 tetrodes studied in this paper during Epoch 10. These LFPs have temporal patterns that can be separated into two clusters. The first consists of T7, T8, T9 and T2 which are all on the posterior (back) portion of the dorsal CA1 region. The second consists of the remaining channels which are all on the anterior portion (front).

Figure 1.6 (left) displays the LFPs from tetrode T22 during the first 30 epochs; the boxplots of its auto-correlation function (ACF) across all 247 epochs; and the boxplots of the partial auto-correlation function (PACF) across all epochs. We observe that the boxplots of ACF fail to drop to zero even after very long lags and there is a cyclical behavior in the pattern. Both of these could be evidence of non-stationarity (or long-memory). These suggest pre-processing the data by taking a first order difference. The results of LFPs after differencing are shown on the right side of Figure 1.6. Compared to the previous plots, the ACF boxplots eventually decay to zero with smaller interquartile range, which means that the pre-processed data looks more stationary and the correlation drops to zero faster than the original LFPs. Therefore we will conduct our data analyses on the first order differenced LFPs.

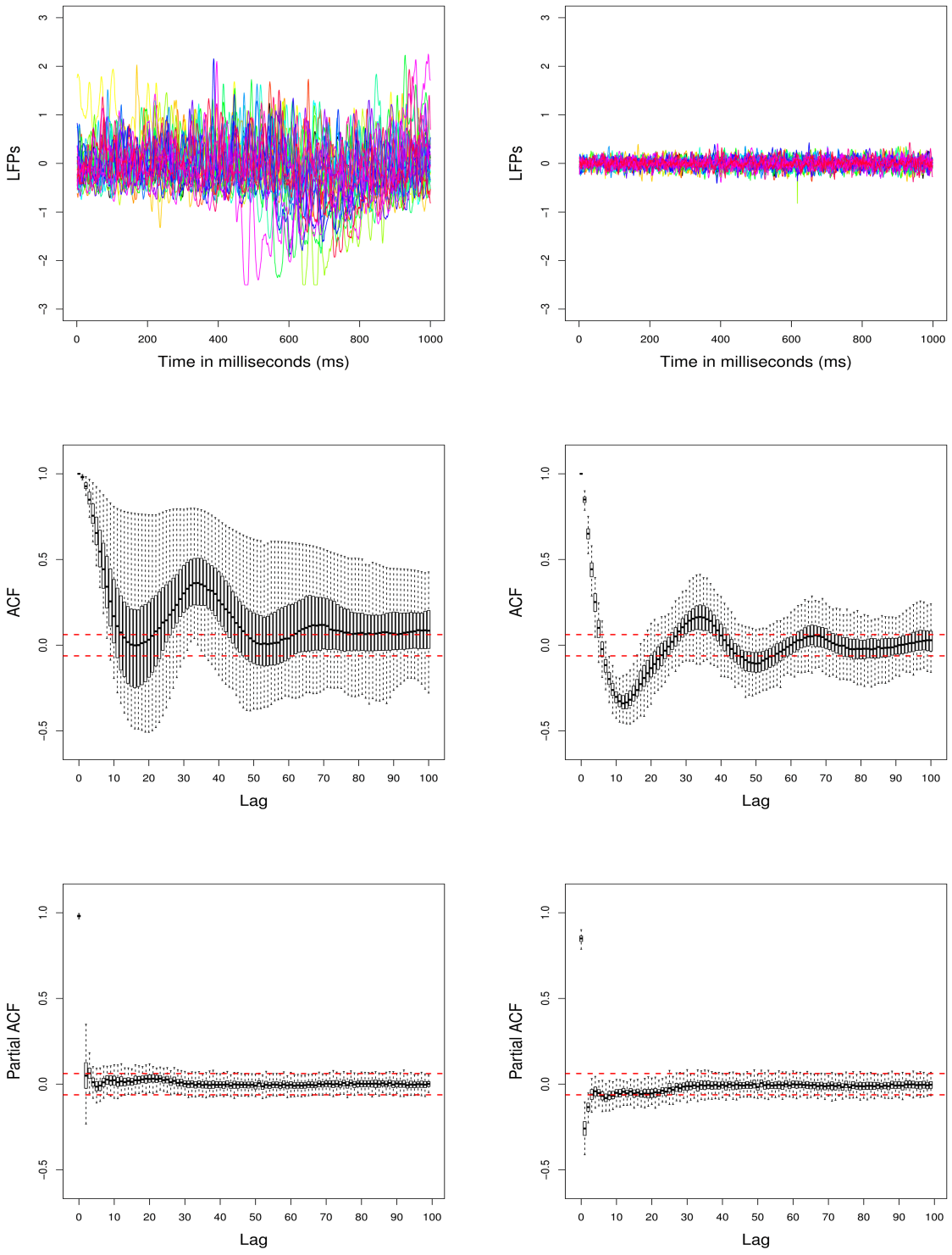

Figure 1.6: Top: The LFPs time series plots of the first 30 epochs at tetrode T22 before (left) and after (right) processing. Middle: The boxplots of auto-correlation function (ACF) from tertrode T22 before (left) and after (right) processing across all epochs. Bottom: The boxplots of partial auto-correlation function (PACF) from tetrode T22 before (left) and after (right) processing across all epochs.

The remainder of this dissertation is arranged as follows. In Chapter 2, I present the proposed methods for characterizing hippocampal connectivity in signal trial. Proposed methods for multi-trial study is in Chapter 3, followed by Conclusion in Chapter 4.

Chapter 2

Characterizing hippocampal connectivity in single-trial LFPs

2.1 Introduction

Connectivity between populations of neurons is crucial to fully characterize brain processes during cognition (e.g., memory and learning) and even during resting-state. Moreover, alterations in brain connectivity is widely believed to be implicated in a number of neurological and mental diseases such as obsessive compulsive disorder and Alzheimer's disease. However, the underlying mechanisms of brain connectivity remain elusive. First, there is no set of universally-agreed measures for characterizing connectivity. Second, there are major statistical and computational challenges for modeling and analyzing multichannel brain signals – especially when the number of parameters is large which often happens when the number of channels is large and/or the temporal lag for parametric models such as vector autoregressive (VAR) is high. Our contribution in this paper is a scalable approach to estimate connectivity in multichannel brain physiological signals modeled with high dimensional parameters.

The work is motivated by our current collaborations with the Fortin Laboratory (UC Irvine) whose research requires developing a systematic statistical framework to quantify functional and effective connectivity among multi-site neural activity signals recorded in rats performing complex memory tasks. The electrophysiological data recorded from rats include local field potentials (LFPs) and an example of a recording for one epoch (here an epoch is 1 second time block) is given in Figure 2.1. LFP signals have excellent temporal resolution (here 1000 observations per second). It is comparable to electroencephalograms (EEGs) in terms of temporal resolution and both capture electrical activity of the neurons. However, LFPs are recorded invasively since these are obtained from electrodes that are chronically implanted inside the brain. Because LFPs are obtained from implanted electrodes, they have lower contamination compared to scalp EEGs. They contain less non-neuronal physiological activity (e.g., muscular activity) and therefore possess a higher signal-to-physiological-noise ratio. One disadvantage of LFPs, however, is its limited utility in humans due to its invasive nature. However, these will continue to be a valuable tool for investigating brain function in animals which can then provide useful information for modeling brain function in humans. One of the challenges to fitting statistical models to LFPs is that the parameter space can be high dimensional. The number of recording tetrodes (P) in LFPs can range from 8-100; and the temporal order (d) of parametric models such as vector autoregressive (VAR) models needs to be sufficiently large in order to accurately capture the dynamics in these complex processes. In this setting the number of parameters in a VAR model is P^2d, which can be large.

In this thesis we will develop a computationally scalable method for fitting high dimensional complex models that addresses two important goals in brain science: (1.) To identify the connectivity structure between channels in a brain network and (2.) To quantify both the strength and directionality of connectivity between these channels. Our approach is to fit a VAR model with potentially high temporal lag in order to more accurately capture complex lead-lag temporal dynamics between the channels or leads. Estimates of the VAR model

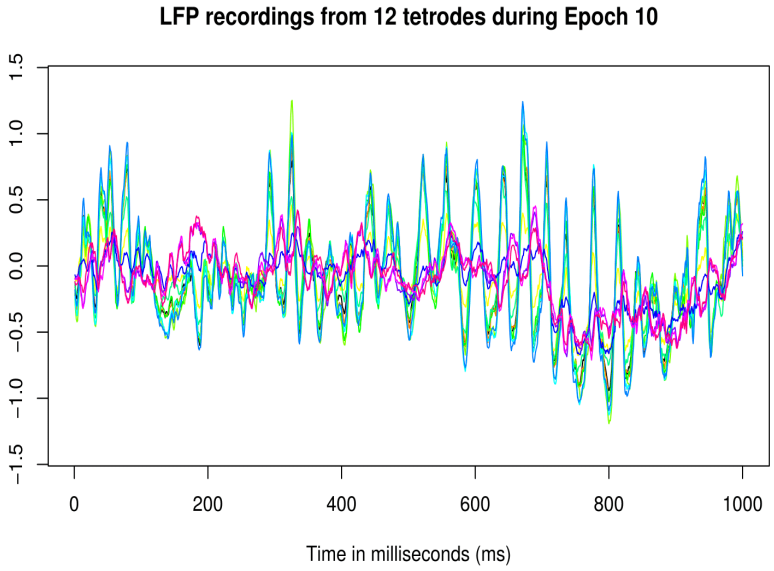

Figure 2.1: Local field potential (LFP) recordings from 12 tetrodes during one epoch (1000 milliseconds; $T = 1000$). Each time series with color indicates the LFP recording from one tetrode.

will be obtained by a combination of regularization to maintain high specificity and least squares estimation to reduce bias and mean-squared error. The method will be applied to LFPs obtained from a rat performing an odor sequence memory task, in which he is required to identify each odor as being presented in the correct or incorrect sequence position.

To characterize connectivity in a multichannel LFP signal we shall use the vector autoregressive (VAR) model [46]. A P-dimensional brain signal $\mathbf{X}_t$ is said to follow a VAR model of order d, denoted VAR(d), if it has the representation

$$\mathbf{X}_t \;=\; \Phi_1 \mathbf{X}_{t-1} + \ldots + \Phi_d \mathbf{X}_{t-d} + \varepsilon_t \quad t = d+1, ..., T \tag{2.1.1}$$

where Φ_ℓ's $\in \Re^{P\times P}$ are the autoregressive coefficient matrices and $\varepsilon_t \overset{iid}{\sim} N_P(\overrightarrow{0}, \Sigma)$. The interconnectivity between channels is determined by the autoregressive coefficient matrices $\{\Phi_\ell\}_{\ell=1}^{d}$ and spatial covariance matrix Σ. Thus, the VAR model provides a broad framework for capturing complex temporal and cross-sectional interrelationship among the time series

(in particular, directionality of frequency-specific connectivity). Consequently it can be applied to model the Granger-causal relation between channels [28].

To illustrate connectivity via the VAR matrix, consider Figure 2.1.1 and denote the LFP traces of brain region to be u-th and v-th channel. Then the entry Φ_ℓ^{uv} shows the impact of the input from v-th channel at time $t-\ell$ to brain activity at u-th channel at the current time t. If $\Phi_\ell^{uv}=0$ and $\Phi_\ell^{vu}=0$ for all lags ℓ then, there is no connectivity between these two channels as determined by VAR model. A positive value indicates that the signal of v-th channel at time $t-\ell$, conditional on LFP values at other times, has positive linear dependence with u-th channel at time t. That is, a marginal increase in activity in v-th channel leads to a increased future activity in u-th channel. Thus, the entries of $\{\Phi_\ell\}_{\ell=1}^d$ contain the information of brain connectivity between channels. In this paper, we shall use partial directed coherence (PDC) [4, 5] to characterize effective (directed) connectivity. This measure is more specific and provides more information, in particular frequency-specific directionality, than simply the coefficients of the VAR matrices. PDC is frequency-specific: it measures how an oscillatory activity (at a particular frequency band) at a present time in one channel may impact oscillatory activity of the same frequency band at another channel at a future time point.

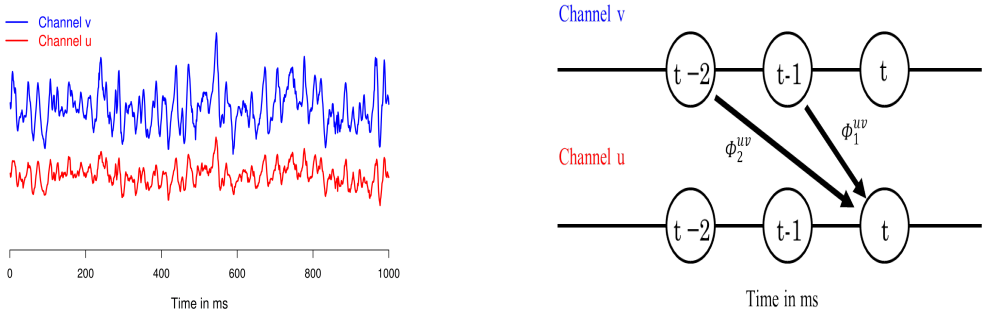

(a) LFP traces (b) Explicit lagged cross-dependence in VAR

Figure 2.2: LFP traces and VAR. Φ_ℓ^{uv} $(\ell=1,2)$ captures the impact of the input from v-th channel at time $t-\ell$ to brain activity at u-th channel at the current time t.

As noted above effective connectivity between channels will be characterized by the VAR coefficient matrices. This is challenging because the parameter space of a VAR model for brain signals is usually high. For example, if we fit a VAR(10) model to 12 leads or channels, there are $10 \times 12^2 = 1440$ parameters in total to estimate, which subsequently requires intensive computation. One could suggest fitting a model with low temporal lag in order to reduce the number of parameters. The problem with this suggestion, unfortunately, is that a low temporal order might miss potentially important features of the data such as multiple peaks in the spectra.

One classic estimation approach is via least squares which (as long as there are sufficient data points) provides unbiased estimator for the elements of the VAR coefficient matrices but at the cost of high demand of computing. The least squares estimate (LSE) does not possess the specificity for coefficients with true value of zero. Hence it cannot provide an adequate answer to the first question about identifying functionally connected regions in brain network. Another common estimation approach is the LASSO (least absolute shrinkage and selection operator) method which is a particular representative of the penalized regression family [50, 16, 54, 23]. Compared with LSE, the LASSO approach requires smaller computation time [34]. Most importantly, LASSO has higher specificity of zero-coefficients. The main limitation of the LASSO (and most regularization methods) is that the estimators of the non-zero coefficients are biased. Thus, it could lead to misleading results when investigating strength of brain effective connectivity. Inspired by the strengths of each of the two classical approaches (i.e., LSE and the LASSO), we propose to combine these in a two-step estimation procedure which we call the LASSLE method. We demonstrate that LASSLE has inherited low bias for non-zero estimates and high specificity for zero-estimates from LSE and the LASSO separately. As a result, the proposed two-step method has higher specificity and significantly lower mean squared error (MSE) in the simulation study. At this stage, the full theoretical justification is being developed but the numerical experiments are encouraging.

A natural question to ask is whether or not the LASSO method is appropriate for fitting VAR models to brain signals. The answer lies in whether or not brain signals such as LFPs and EEGs indeed exhibit sparse connectivity structure. Due to volume conduction for EEGs, it is not likely that the connectivity structure between channels is sparse. However, though LASSO aims to shrink many of the VAR coefficients to zero but this does not necessarily lead to a sparse connectivity structure. Keep in mind that a pair of channels are functionally disconnected only if *all* of the its corresponding VAR coefficients at *all* lags are estimated to be zero. Thus, imposing sparsity on the VAR coefficient matrices helps to weed out the less important parameters in the VAR model but does not oversimplify the connectivity structure.

The remainder of this chapter is arranged as follows. In Section 2.2, we present the proposed hybrid LASSLE (LASSO+LSE) method followed by finite sample simulation studies in Section 2.3 and analysis of LFP signals in Section 2.4 and the Conclusion in Section 2.5.

2.2 A proposed two-step LASSO+LSE procedure for fitting a VAR model

First, we note that the VAR(d) model can be alternatively written in a form

$$\underbrace{\begin{bmatrix} (\mathbf{X}_T)' \\ \vdots \\ (\mathbf{X}_{d+1})' \end{bmatrix}}_{Y} = \underbrace{\begin{bmatrix} (\mathbf{X}_{T-1})' & \cdots & (\mathbf{X}_{T-d})' \\ \vdots & \ddots & \vdots \\ (\mathbf{X}_d)' & \cdots & (\mathbf{X}_1)' \end{bmatrix}}_{\mathbb{X}} \underbrace{\begin{bmatrix} (\Phi_1)' \\ \vdots \\ (\Phi_d)' \end{bmatrix}}_{B} + \underbrace{\begin{bmatrix} (\varepsilon_T)' \\ \vdots \\ (\varepsilon_{d+1})' \end{bmatrix}}_{E}. \tag{2.2.1}$$

Next, denote $Y = [y_1, y_2, ..., y_P]$, $B = [b_1, b_2, ..., b_P]$, $E = [e_1, e_2, ..., e_P]$. Denote the k^{th} column vector of the matrices Y, B and E ($k = 1, 2, ..., P$) to be y_k, b_k, e_k. Then we have

$$\underbrace{y_k}_{m\times 1} = \mathbb{X}\underbrace{b_k}_{q\times 1} + \underbrace{e_k}_{m\times 1}, \quad e_k \overset{indep}{\sim} N_m(\overrightarrow{0}, \sigma_{kk} I_m) \tag{2.2.2}$$

where $m = T - d$, $q = P \times d$, and σ_{kk} is the k^{th} diagonal element of the covariance matrix Σ. Note that Equation (2.2.1) is finally decomposed into many sub-linear regression problems of estimating $\{b_k\}_{k=1}^{P}$ in a parallel manner and all the entries of connectivity matrices are included in $\{b_k\}_{k=1}^{P}$.

2.2.1 Least squares estimation (LSE)

To fit a linear regression model, the most common approach is via least squares estimation so that the least squares estimator $\widehat{b}_k$ satisfies

$$\widehat{b}_k = \underset{b_k \in \Re^q}{\operatorname{argmin}} \|y_k - \mathbb{X} b_k\|^2 \tag{2.2.3}$$

which gives the unbiased estimator $\widehat{b}_k = (\mathbb{X}'\mathbb{X})^{-1}\mathbb{X}' y_k$. Some papers [22] argue that in high dimensional case the number of parameters q can be larger than the number of observations m, thus this method has limitations due to the nonsingular matrix $\mathbb{X}'\mathbb{X}$. However, we do not worry about this when analyzing the LFP data since normally we have replicated measurements from multiple epochs. The biggest problem here is that LSE has poor specificity for coefficients with true value of zero. It always produces estimates that are very close to zero rather than exactly zero, which reflects non-connectivity between channels. Indeed when LFP channels are not effectively connected with each other, then an excess non-zero estimate could lead to incorrect characterizations of connectivity through partial directed coherence. Moreover, even a trivial amount of bias for one coefficient, when added across

thousands of coefficients, can produce large mean squared error (as demonstrated in the simulation study).

2.2.2 LASSO family estimation

In order to overcome the problem of non-specificity by the LSE method, recent attention has been focused on the family of penalized regression models as viable solutions to this problem. One of the well known methods of this family is LASSO regression (with L_1 penalty term). The estimates given by LASSO are the solution to the minimization of the criterion

$$\widetilde{b}_k = \underset{b_k \in \Re^q}{\operatorname{argmin}} \|y_k - \mathbb{X} b_k\|^2 + \lambda \|b_k\|_1 \tag{2.2.4}$$

The penalty term will force a lot of excess non-zero estimates to exact zero, which provides good estimate for the sparsity of the VAR coefficient matrices $\{\Phi_\ell\}_{\ell=1}^d$ and could consequently greatly simplify the calculation of connectivity measures (e.g., PDC) by focusing only on the more important coefficients. In the implementation of the algorithms for LASSO, we take advantage of the results demonstrated by [14] where estimation of generalized linear models with convex penalties can be handled by cyclical coordinate descent and computed along a regularization path. The price of LASSO is that the non-zero estimates are biased of true values which leads to incorrect estimates of the strength of connectivity between channels (PDC).

2.2.3 LASSLE: proposed two-step estimation method

Motivated by both the advantages and limitation of each of the previous approaches, we propose a two-step procedure to estimate VAR model parameters. Our method consists of these two steps:

Step 1. Apply LASSO to identify entries in $\{\Phi_\ell\}_{\ell=1}^d$ whose estimates are not set to 0.

$$\widehat{S}_k = \{j \in \{1, ..., q\} : \widehat{b}_k^j \neq 0\} \tag{2.2.5}$$

Step 2. Fit LSE with the constraint that "zero" entries estimates from Step 1 are fixed to 0

$$\widetilde{b}_{kLAS} = \underset{b_k : b_k^j = 0, j \in \widehat{S}_k^c}{\operatorname{argmin}} \|y_k - \mathbb{X} b_k\|_2^2 \tag{2.2.6}$$

Algorithm 1 LASSLE Algorithm

procedure TWO-STEP ESTIMATION
Step 1:
    Generate a sequence of (d, λ) and randomly divide data to K folds
    For a possible choice of (d, λ), leave one fold as test data at each time
    Train 2.2.2 with LASSO method on other folds and compute $\{\widehat{\Phi}_\ell\}_{\ell=1}^d$ for $\{\Phi_\ell\}_{\ell=1}^d$
    Based on $\{\widehat{\Phi}_\ell\}_{\ell=1}^d$, calculate prediction error on test set and finally take average
    Select (d, λ) with the lowest average prediction error
    Obtain estimate $\{\widehat{b}_k\}_{k=1}^P$ for $\{b_k\}_{k=1}^P$ in Equation (2.2.2) of lag d using LASSO method with λ
Step 2:
    if $\widehat{b}_k^j = 0$ **then**
        Set $b_k^j = 0$.
    if $\widehat{b}_k^j \neq 0$ **then**
        Keep b_k^j.
    Obtain estimate $\{\widetilde{b}_{kLAS}\}_{k=1}^P$ for $\{b_k\}_{k=1}^P$ in Equation (2.2.2) with LSE under above constriction
    Obtain estimate $\{\widetilde{\Phi}_{\ell LAS}\}_{\ell=1}^d$ for $\{\Phi_\ell\}_{\ell=1}^d$ by arranging $\{\widetilde{b}_{kLAS}\}_{k=1}^P$

To obtain the optimal tuning parameter λ, we employ a K-fold cross-validation test in Step 1. A sequence of candidates of λ will be pre-specified and the optimal value is selected such that the average of prediction error on test data is minimized.

2.2.4 Theoretical consideration

For linear regression, under Irrepresentable Condition[1], $\{\widehat{b}_k\}_{k=1}^P$ have sign consistency assured by LASSO estimator [55], which means for sufficient large sample size $T-d$

$$\Pr(\operatorname{sgn}(\widehat{b}_k) = \operatorname{sgn}(b_k)) \to 1 \tag{2.2.7}$$

where $\operatorname{sgn}(b_k)$ is the sign function with value of 1, 0 or -1 corresponding to $b_k > 0$, $b_k = 0$ or $b_k < 0$ respectively. Therefore, $\mathbf{P}(\widehat{S}_k \neq S_k) \to 0$, which implies high specificity of true zero VAR coefficients. Then our inaccurate non-zero estimate will be updated in Step 2. Since we put a constraint for LSE in Step 2, the computing is much simplified compared with merely LSE. Moreover, the bias and mean squared error of LASSLE estimator will be bounded [33]

$$||E(\widetilde{b}_{kLAS}) - b_k||_2^2 \leq 2\mathbf{P}(\widehat{S}_k \neq S_k)\{O(\frac{1}{m}) + ||b_k||_2^2 + \tau\sigma_{kk}\} \tag{2.2.8}$$

$$E||\widetilde{b}_{kLAS} - b_k||_2^2 \leq 2\frac{\sigma_{kk}}{m}tr(\Psi_{11}^{-1}) + \sqrt{\mathbf{P}(\widehat{S}_k \neq S_k)}\{O(\frac{1}{m}) + ||b_k||_2^2 + \tau\sigma_{kk}\} \tag{2.2.9}$$

Thus, our non-zero estimates are almost unbiased, which is significantly improved from LASSO. Final estimates given by LASSLE in simulation study have substantially lower general mean squared error. Thus our approach is able to both indicate the most important effective connectivity and give a more precise estimate of the strength of connectivity.

[1] Assume $b_k = (b_k^1, ..., b_k^J, b_k^{J+1}, ..., b_k^q)^T$, where $b_k^j \neq 0$ for $j = 1, ..., J$ and $b_k^j = 0$ for $j = J+1, ..., q$. Let $b_k^{(1)} = (b_k^1, ..., b_k^J)^T$ and $b_k^{(2)} = (b_k^{J+1}, ..., b_k^q)^T$. Denote Gram matrix $\Psi = \frac{1}{n}\mathbb{X}'\mathbb{X} = \begin{pmatrix} \Psi_{11} & \Psi_{12} \\ \Psi_{21} & \Psi_{22} \end{pmatrix}$, then Irrepresentable Condition is satisfied if there exists a positive constant vector η, such that $|\Psi_{21}(\Psi_{11})^{-1}\operatorname{sgn}(b_k^{(1)})| \leq 1 - \eta$.

2.2.5 Measure of dependence

In this section, we enumerate the different measures of dependence between components of a multivariate time series (or between different channels) using the VAR model. First, a P-channel time series, denoted $\{\mathbf{X}_t = (\mathbf{X}_t^1, ..., \mathbf{X}_t^P)', t = 1, 2, ...\}$, is weakly stationary if the following are satisfied:

(a.) $E(\mathbf{X}_t)$ is constant over all time t, and

(b.) the autocovariance function matrix

$$cov(X_t, X_{t+h}) = \Gamma(h) = \begin{pmatrix} \gamma_{11}(h) & \gamma_{12}(h) & \dots & \gamma_{1P}(h) \\ \gamma_{21}(h) & \gamma_{22}(h) & \dots & \gamma_{2P}(h) \\ \vdots & \vdots & \ddots & \vdots \\ \gamma_{P1}(h) & \gamma_{P2}(h) & \dots & \gamma_{PP}(h) \end{pmatrix}$$

depends only on the lag h, where $\gamma_{uv}(h) = cov(X_t^u, X_{t+h}^v)$ for all pairs of channels $u, v = 1, ..., P$.

Moreover, if the sequence of auto- and cross-covariance between any pair of channels u and v is absolutely summable, i.e., $\sum_{h=-\infty}^{\infty} |\gamma_{uv}(h)| < \infty$, then we define the spectral density matrix of $\{\mathbf{X}_t\}$ to be

$$f(\omega) = \sum_{h=-\infty}^{\infty} \Gamma(h) e^{-2\pi i \omega h}, \quad -1/2 \leq \omega \leq 1/2. \tag{2.2.10}$$

The spectral matrix has dimension $P \times P$ whose diagonal elements $f_{uu}(\omega)$ are the auto-spectra of the channels at frequency ω and the off-diagonal elements $f_{uv}(\omega)$ are the cross-spectra of channels u and v at frequency ω.

The first dependency measure that we will consider is coherency. Coherency between the u-th and v-th channels at frequency ω, is defined as

$$\rho_{uv}(\omega) = \frac{f_{uv}(\omega)}{\sqrt{f_{uu}(\omega)}\sqrt{f_{vv}(\omega)}}. \tag{2.2.11}$$

One can interpret coherency as the cross-correlation between the ω-oscillatory component in channel u and the ω-oscillatory component in channel v [41].

The second dependency measure is coherence. Coherence between the u-th and v-th channels at frequency ω, is defined as

$$\rho^2_{uv}(\omega) = \frac{|f_{uv}(\omega)|^2}{f_{uu}(\omega)f_{vv}(\omega)}. \tag{2.2.12}$$

When $\rho^2_{uv}(\omega)$ is close to 1 then both channels u and v share a common ω-oscillatory activity. Moreover, when the cross-correlation between the u and v channels is 0 at all time lags, then the coherency (and coherence) between these channels at *all* frequencies is 0. A large coherence value between channels u and v could be due to direct connectivity between these two channels or could be indirectly due to the intervening effect of other channel(s). To measure the strength of connectivity between a pair of channels – with the effect of all intervening channels removed – we shall use partial coherence.

The third dependency measure is partial coherence. Define the matrix $g(\omega) = f^{-1}(\omega)$ and denote the diagonal elements as $g_{pp}(\omega)$. Let $h(\omega)$ be a diagonal matrix whose elements are $g_{pp}^{-1/2}(\omega)$. Define the matrix $C(\omega)$ to be

$$C(\omega) = -g(\omega)h(\omega)g(\omega) \tag{2.2.13}$$

Then, the partial coherence between the u-th and v-th channels is the modulus squared of the (u, v)-th element of $C(\omega)$ [12, 11]

$$\zeta_{uv}^2(\omega) = |C_{uv}(\omega)|^2 \tag{2.2.14}$$

We now present the fourth dependency measure which is partial directed coherence developed in [4] and refined in [5]. Consider a VAR(d) model given by Equation (1.2.1), define

$$A(\omega) = I - \sum_{\ell=1}^{d} \Phi_\ell \exp(-i2\pi\omega\ell/\Omega) \tag{2.2.15}$$

be the transform of sequence $\{\Phi_\ell\}_{\ell=1}^d$ at frequency ω, where Ω is the sampling frequency. The partial directed coherence from channel v to channel u at frequency ω is defined as

$$\pi_{uv}^2(\omega) = \frac{|A_{uv}(\omega)|^2}{\sum_{m=1}^{P} |A_{mv}(\omega)|^2} \tag{2.2.16}$$

which measures the direct influence from channel v to channel u conditional on all the outflow from channel v. PDC gives an indication on the extent to which present frequency-specific oscillatory activity from a sender channel explains future oscillatory activity in a specific receiver channel relative to all channels in the network.

2.2.6 Model selection

To determine the best order $\widehat{d}$ of VAR, we first use least squares estimation to obtain $\{\widehat{\Phi}_\ell\}_{\ell=1}^{d_j}$ for each candidate order in the set $\{d_j\}_{j=1}^J$. We search among a class of reasonable temporal lag orders. From our analysis of LFPs where there are usually less than 4 peaks in the spectrum, it would be reasonable to use an upper bound of 12 as the temporal lag order.

Then we calculate the sum of squared errors

$$SSE(d_j) = \sum_{t=d_j+1}^{T} (\mathbf{X}_t - \sum_{\ell=1}^{d_j} \widehat{\Phi}_\ell \mathbf{X}_{t-\ell})(\mathbf{X}_t - \sum_{\ell=1}^{d_j} \widehat{\Phi}_\ell \mathbf{X}_{t-\ell})' \tag{2.2.17}$$

Consequently the conditional MLE of the error covariance matrix Σ for a candidate order d_j is

$$\widehat{\Sigma}(d_j) = SSE(d_j)/(T - d_j) \tag{2.2.18}$$

which is analogous to univariate regression case. To choose the optimal lag, we compute three information criteria - the Akaike Information criterion (AIC), Bayesian Information criterion (BIC) and Hannan-Quinn information criterion (HQC), respectively, for each candidate order d_j.

$$AIC(d_j) = \log|\widehat{\Sigma}(d_j)| + 2/T(P^2 d_j) \tag{2.2.19}$$

$$BIC(d_j) = \log|\widehat{\Sigma}(d_j)| + \log T/T(P^2 d_j) \tag{2.2.20}$$

$$HQC(d_j) = \log|\widehat{\Sigma}(d_j)| + 2\log\log T/T(P^2 d_j) \tag{2.2.21}$$

The optimal order for each criterion, denoted $\widehat{d}$ is the minimizer of the cost functions and thus gives the optimal balance between fit (as measured by SSE) and model complexity (as expressed by the penalty terms). It has been noted that $\widehat{d}^{BIC} \leq \widehat{d}^{HQC} \leq \widehat{d}^{AIC}$ when $T \geq 16$ [27]. In the analysis of LFPs, the difference between $\widehat{d}^{BIC}$ and $\widehat{d}^{AIC}$ is at most 1, therefore we choose $\widehat{d}^{AIC}$ to capture more temporal correlation by fitting a VAR of slightly higher lag

order.

2.2.7 Bootstrap-based inference

To conduct inference on the VAR parameters, a general idea is to derive the asymptotic property of the estimated VAR coefficient matrices. However, this is not trivial and is still under investigation given the high dimensionality of the VAR parameter space. An alternative is to develop a bootstrap-based inference, which has been used in time series [42, 43, 29, 45, 31]. After obtaining the estimates of the VAR(d) coefficient matrices, $\{\widetilde{\Phi}_\ell\}_{\ell=1}^d$, we use these estimates and corresponding residuals to generate new bootstrapped trials. Denote

$$R_t = \mathbf{X}_t - \widetilde{\Phi}_1 \mathbf{X}_{t-1} - ... - \widetilde{\Phi}_d \mathbf{X}_{t-d}, \quad t = d+1, ..., T. \tag{2.2.22}$$

by residual at time t. Then, to generate a bootstrapped trial $\{\mathbf{X}_t^{(b)}\}_{t=1}^T$, we shall use the following bootstrap algorithm. Define the bootstrapped residuals to be $\{R_t^{(b)}\}_{t=d+1}^T$, which are selected with replacement from $\{R_t\}_{t=d+1}^T$. Let $\mathbf{X}_t^{(b)} = \mathbf{X}_t$ when $t = 1, ..., d$, then $\mathbf{X}_t^{(b)} = \sum_{\ell=1}^d \widetilde{\Phi}_\ell \mathbf{X}_{t-\ell}^{(b)} + R_t^{(b)}$ are bootstrapped data at time t when $t = d+1, ..., T$.

Algorithm 2 Bootstrap Algorithm

1: For $b = 1, ..., B$
2: *Step 1*:
3: Let $\mathbf{X}_t^{(b)} = \mathbf{X}_t$ for $t = 1, 2, ..., d$
4: *Step 2*:
5: Randomly sample bootstrapped residuals $\{R_t^{(b)}\}_{t=d+1}^T$ from $\{R_t\}_{t=d+1}^T$ with replacement
6: *Step 3*:
7: Let $\mathbf{X}_t^{(b)} = \sum_{\ell=1}^d \widetilde{\Phi}_\ell \mathbf{X}_{t-\ell}^{(b)} + R_t^{(b)}$ be bootstrapped data at time t when $t = d+1, ..., T$

Given the b-th bootstrap time series $\{\mathbf{X}_t^{(b)}\}_{t=1}^T$, we compute the VAR coefficient estimates which we denote by $\{\widetilde{\Phi}_\ell^{(b)}\}_{\ell=1}^d$ using the LASSLE method and then compute partial directed

coherence estimate. We repeat this procedure a sufficient large number of times, then we can find the empirical distribution and obtain the 95% bootstrap confidence interval of both VAR parameters and PDCs.

2.3 Simulation study

2.3.1 Simulation design

To compare the performance of the proposed LASSLE approach with the classical methods (i.e., LSE only and LASSO only), we conducted a simulation study of VAR(d) model for two different brain network types. The first is "Cluster", which is a type of network that has high level local and global connectivity efficiency. In Figure 2.3, channels (red nodes) are located in four brain regions, while the edge between two red nodes indicates connectivity at channel level. Auto-connectivity inside each region makes channels from the same region connect like a cluster, and cross-connectivity between brain regions determines whether these clusters are connected with each other. For example, Cluster 2 is independent from other regions, but Cluster 1 and Cluster 4 are connected due to the cross-connectivity at region level.

In the second type "Scale-free", shown in Figure 2.4, there is no significant auto-connectivity or cross-connectivity at the region level, but all the brain channels are connected within the network. Most of the channels have several connections with other channels, with the exception that a few channels are heavily connected. The idea is that these channels play a central role in the organization of entire brain network, as they are mostly responsible for the connectivity efficiency.

For both network types, we use Equation (1.2.1) to generate time series data sets. The VAR

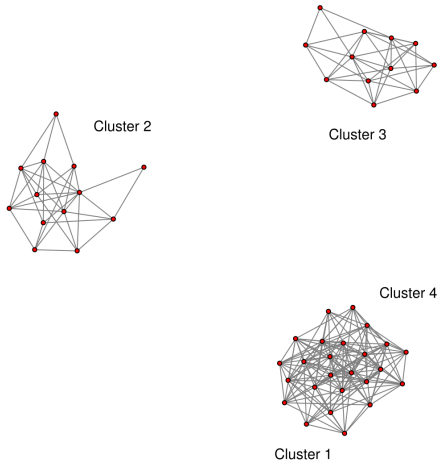

Figure 2.3: 50 brain channels of "Cluster" type

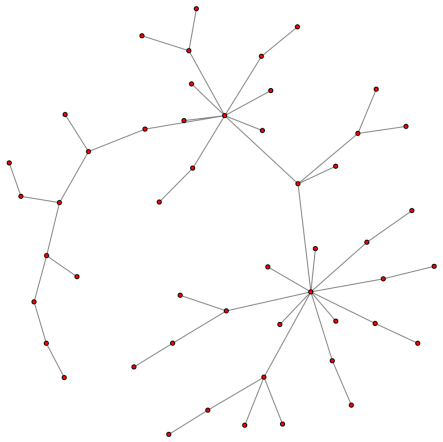

Figure 2.4: 50 brain channels of "Scale-free" type

matrix Φ_1 of setting $\{P = 50,\, d = 1\}$ is visualized in Figure 2.5(a) and Figure 2.6(a). Each small square represents the non-zero entry of Φ_1 and different colors indicate different values according to the color bar. The blank part of coefficient matrix are the zero entries. In addition, ε_t follows a Gaussian distribution and the covariance matrix is not necessary to be

diagonal. We run $N = 1,000$ simulations for each VAR setting respectively and the time series data of each channel contains $T = 10,000$ time points. Then we apply LSE, LASSO and our LASSLE method to estimate coefficient matrices, and compare their results with two important criteria. The first one evaluates how successful the estimate identifies the specific entries with true value of zero, as shown by the visualization of absolute difference between true coefficient matrix and estimated one. The second criteria is their mean squared error, defined as

$$MSE = \frac{\sum_{n,\ell,i,j}(\Phi_\ell^{ij} - \widehat{\Phi}_\ell^{ij})^2}{N} \tag{2.3.1}$$

where $\{\Phi_\ell^{ij}\}_{\ell=1}^d$, $\{\widehat{\Phi}_\ell^{ij}\}_{\ell=1}^d$ represent entries of $\{\Phi_\ell\}_{l=1}^d$ and $\{\widehat{\Phi}_\ell\}_{\ell=1}^d$ respectively. Lower MSE indicates better centering at true connectivity matrix.

2.3.2 Simulation results

Due to the display limit of high dimensional matrix, we only demonstrate visualized results of VAR setting $\{P = 50,\, d = 1\}$.

Results from the "Cluster" setting

In this setting, 50 channels represent measurements in four brain regions and only region 1 and region 4 have cross-connectivity. In the coefficient matrix, all non-zero entries are first randomly assigned either 0.1 or -0.1, then 0.5 is added to all diagonal entries (shown in Figure 2.5(a)). Figure 2.5(b),(c),(d) yield the absolute difference between true connectivity matrix and estimated one by LSE, LASSO and LASSLE method. The color of small squares ranging from white to red indicates the value of absolute difference of each entry. The blank part of the matrix implies that the estimate has given correct zero-estimate for those true zero

entries so that there is no need to distinguish the difference with color. Table 1 demonstrates the MSE results of all three methods under different VAR parameter setting $\{P, d\}$.

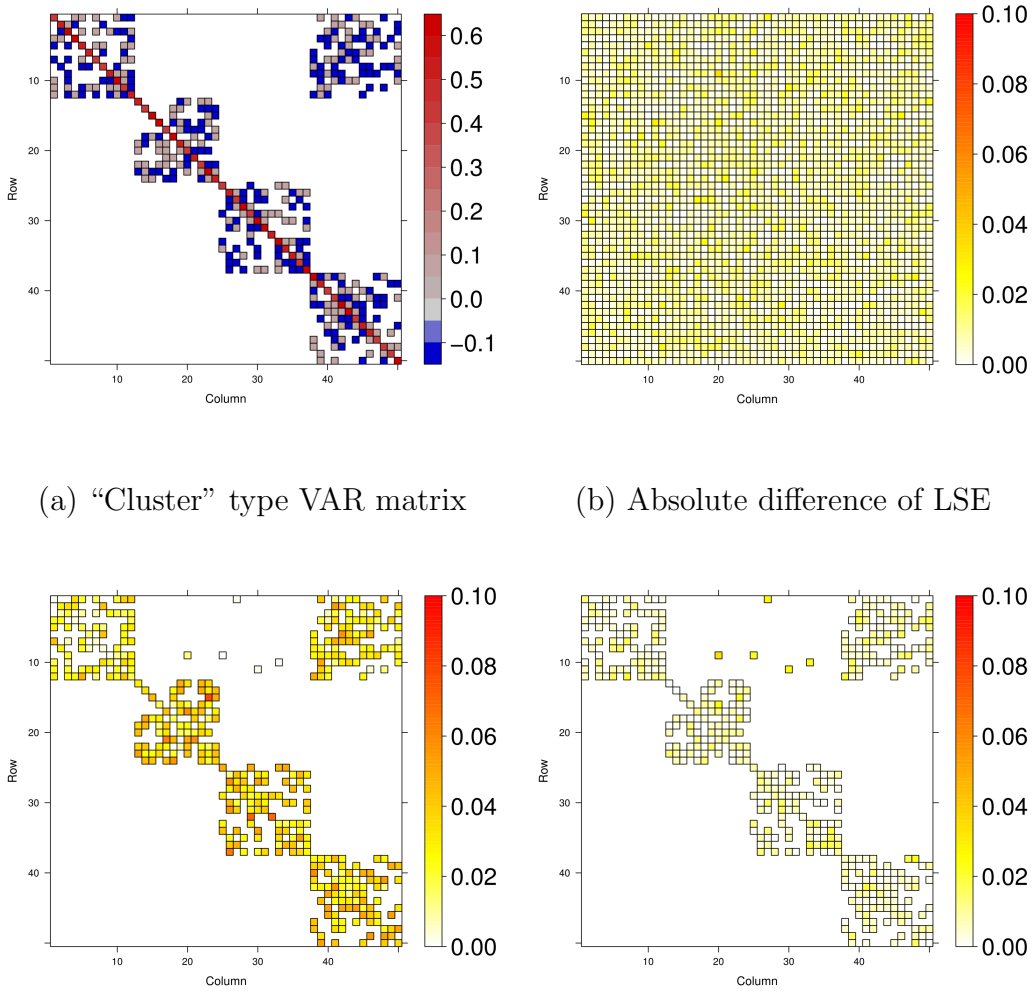

(a) "Cluster" type VAR matrix (b) Absolute difference of LSE

(c) Absolute difference of LASSO (d) Absolute difference of LASSLE

Figure 2.5: Comparison of specificity of true zero on "Cluster" type data with Gaussian noise. Figure 2.5(a) demonstrates the true VAR(1) coefficient matrix with $P = 50$. Figure 2.5(b),(c),(d) yield the absolute difference between true matrix and estimated matrix by LSE, LASSO and LASSLE method respectively.

VAR Parameter Setting			MSE $\times 10^{-3}$		
Number	P	d	LSE	LASSO	LASSLE
100	10	1	8	93	4 *
500	10	5	58	326	36 *
1,000	10	10	134	412	82 *
2,500	50	1	176	464	24 *
5,000	50	2	457	739	93 *
10,000	100	1	697	1016	65 *

Table 2.1: Comparison of MSE between three methods on "Cluster" type data

Results from the "Scale-free" setting

To generate "Scale-free" type data, we assign 0.5 to all diagonal entries of connectivity matrix, and 0.1 or -0.1 randomly to other non-diagonal entries with small probability (seen in Figure 2.6(a)). Figure 2.6(b),(c),(d) give the visualized estimate results given by LSE, LASSO and LASSLE method separately. MSE comparison can be found in Table 2.

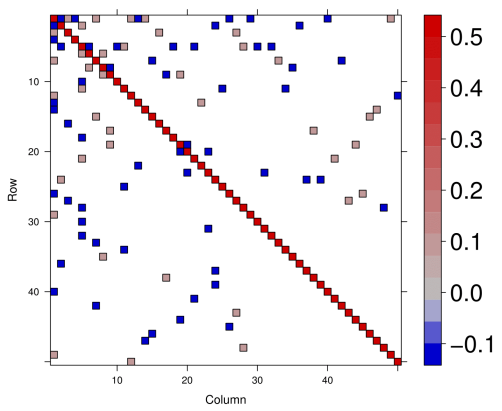

(a) "Scale-free" type VAR matrix

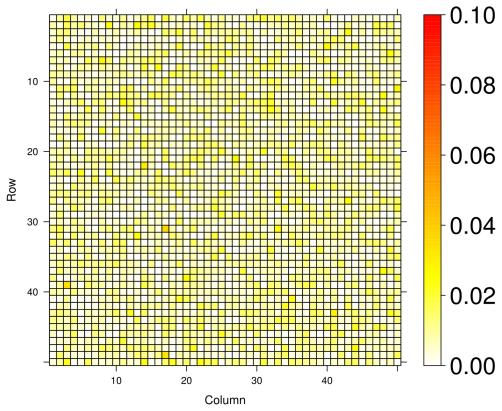

(b) Absolute difference of LSE

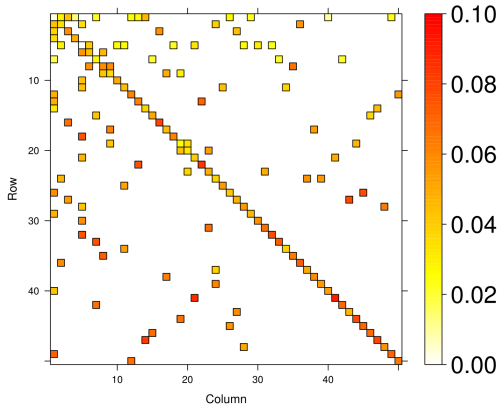

(c) Absolute difference of LASSO

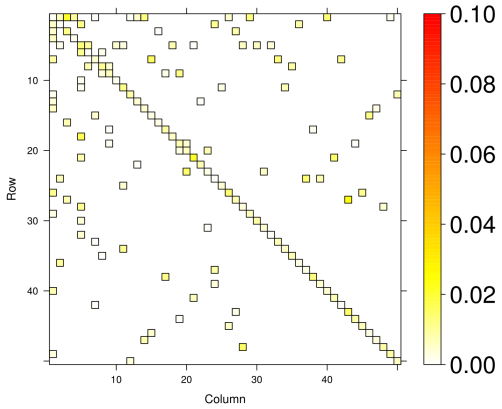

(d) Absolute difference of LASSLE

Figure 2.6: Comparison of specificity of true zero on "Scale-free" type data with Gaussian noise. Figure 2.6(a) demonstrates the true VAR(1) coefficient matrix with $P = 50$. Figure 2.6(b),(c),(d) yield the absolute difference between true matrix and estimated matrix by LSE, LASSO and LASSLE method respectively.

VAR Parameter Setting			MSE $\times 10^{-3}$		
Number	P	d	LSE	LASSO	LASSLE
100	10	1	7	86	2 *
500	10	5	53	158	16 *
1,000	10	10	130	472	72 *
2,500	50	1	191	432	9 *
5,000	50	2	480	877	37 *
10,000	100	1	762	921	19 *

Table 2.2: Comparison of MSE between three methods on "Scale-free" type data

Discussion

From visualized results, we can find that LSE is unable to give specificity for true zero coefficients, since its estimates do not contain blank squares. However, its estimate has general lower bias across all the entries, which is implied by the light color of absolute difference. LASSO is able to identify most true zero entries, but darker color of rectangles indicate that this method has high bias for the estimate. Our method, constrained with LASSO in Step 1, has inherited the specificity of true zero values from LASSO, consequently can capture true zero values as well as LASSO. Thus in the sense of specificity of true zero, the comparison result is: LASSLE = LASSO >> LSE.

For another important criteria MSE, the proposed LASSLE approach has substantial advantage over LSE and LASSO. In 50-channel "Cluster" setting, the MSE given by LSE and LASSO are approximately 5 times and 10 times the MSE provided by our method. Also, in 50-channel "Scale-free" settlement, LSE and LASSO provide at least 10 times and 20 times higher MSE compared with LASSLE. With the increase of dimensions, the advantage is also increasing geometrically. Therefore, LASSLE performs better with respect to the MSE

criterion compared to both LSE and LASSO.

2.3.3 Bootstrap-based inference

For each VAR setting and its simulation, we follow the bootstrap algorithm in Section 2.7 to generate 1,000 bootstrapped trials and re-estimate the VAR parameters with LASSLE method. We (1.) investigated whether the 95% bootstrap confidence interval given by the empirical distribution of each VAR parameter captured the true value and (2.) compared the center of the bootstrap distribution to the true value of the quantities of interest (VAR parameters and true PDC values). To answer (1.), we plot the empirical distribution of each VAR parameter and compare its 95% empirical confidence interval with the true value. To compare (2.), we obtain the median of bootstrapped estimates for each entry, then use these medians to form a matrix and compare its absolute difference with the true connectivity matrix.

Figure 2.7 and Figure 2.8 demonstrate examples of empirical distribution derived from 1,000 bootstrap estimates. The red dashed line indicates the true value of these example coefficients. The blue curve is the smoothed estimated density curve of each empirical distribution. For some coefficients, e.g., $\Phi_1^{20}, \Phi_{15}^{25}$ in Figure 2.7 and $\Phi_{15}^{40}, \Phi_{30}^{25}$ in Figure 2.8, we are not able to provide a density curve as the empirical distribution is a point-mass density at $x = 0$, in other words, all 1,000 bootstrapped LASSLE estimates of these zero coefficients are exactly zero. We can conclude that 95% confidence interval or set of the empirical distribution can capture the true parameter value in the simulation study.

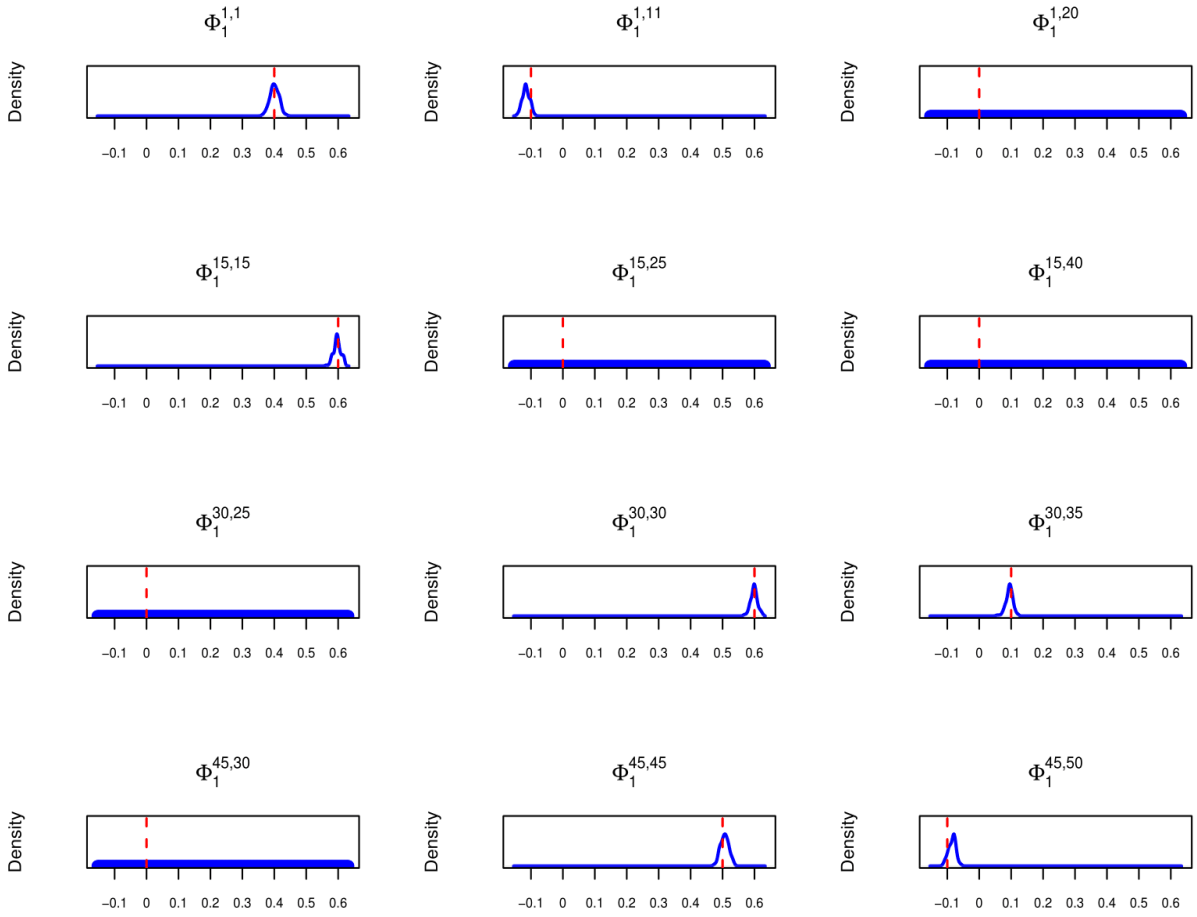

Figure 2.7: Sample empirical distribution of "Cluster" type bootstrapped estimates. Red dashed line indicates the true value of these example coefficients. Blue curve is the smoothed estimated density curve of each empirical distribution. All 1,000 bootstrap estimates of $\Phi_1^{1,20}, \Phi_1^{15,25}, \Phi_1^{15,40}, \Phi_1^{30,25}$ and $\Phi_1^{45,30}$ are zero, so we are not able to plot the point-mass density for these coefficients.

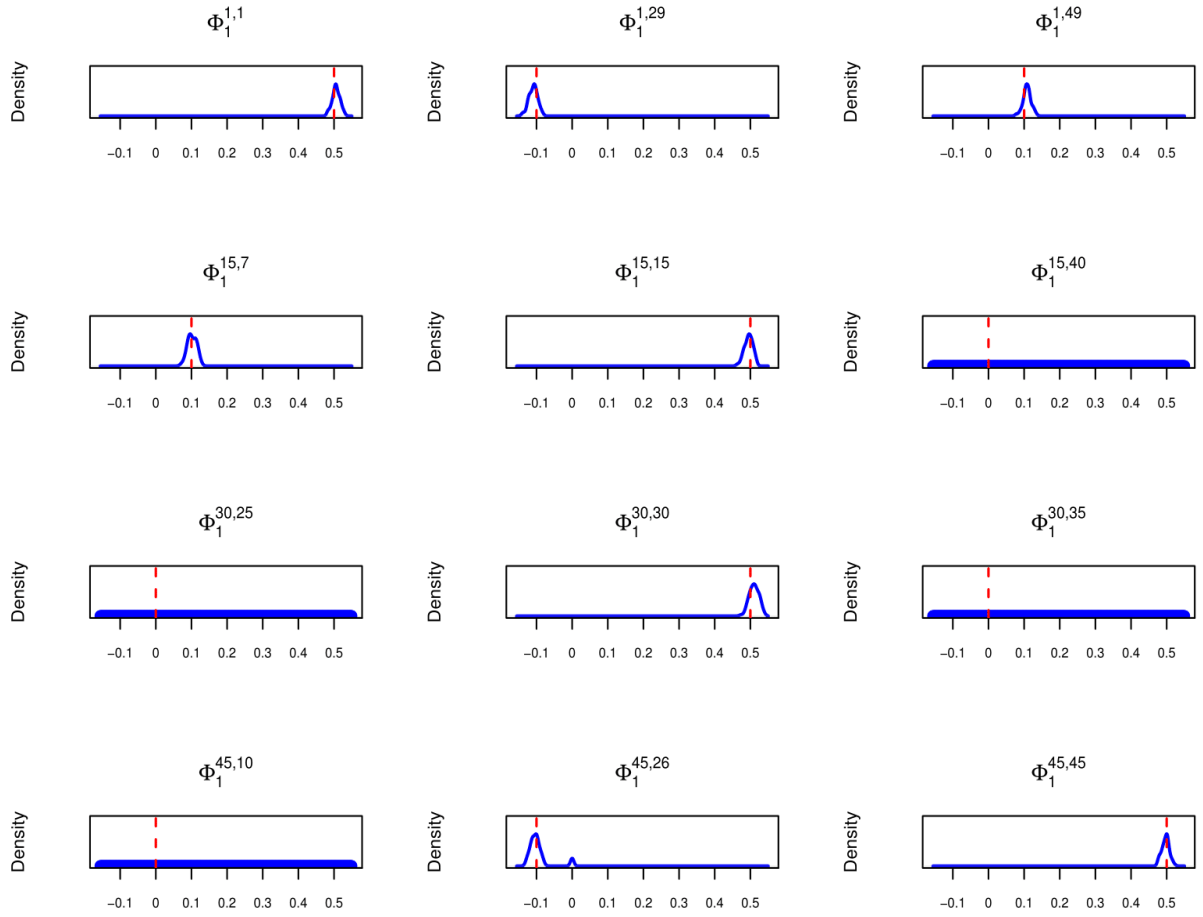

Figure 2.8: Sample empirical distribution of "Scale-free" type bootstrapped estimates. Red dashed line indicates the true value of these example coefficients. Blue curve is the smoothed estimated density curve of each empirical distribution. All 1,000 bootstrap estimates of $\Phi_1^{15,40}, \Phi_1^{30,25}, \Phi_1^{30,35}$ and $\Phi_1^{45,10}$ are zero, so we are not able to plot the point-mass density for these coefficients.

Figure 2.9(a),(b) demonstrate the median of 1,000 bootstrapped LASSLE estimates of "Cluster" and "Scale-free" type data under previous setting $\{P = 50, d = 1\}$ respectively. Figure 2.9(c),(d) yield their absolute difference with the true connectivity matrix. Given the color of most nonzero median estimates of LASSLE is very light, we can conclude that the empirical distributions generated by bootstrap are well centered around the true coefficient values.

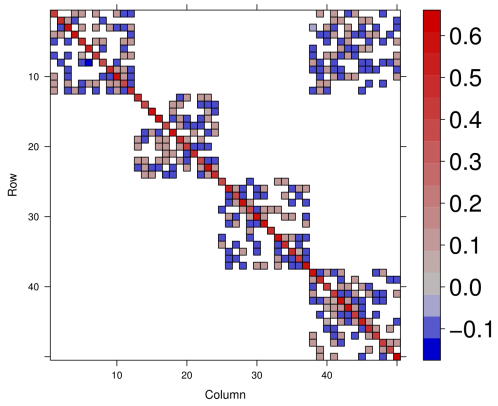

(a) Bootstrap median of "Cluster" type

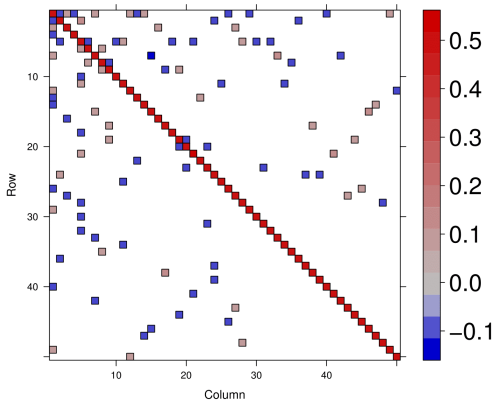

(b) Bootstrap median of "Scale-free" type

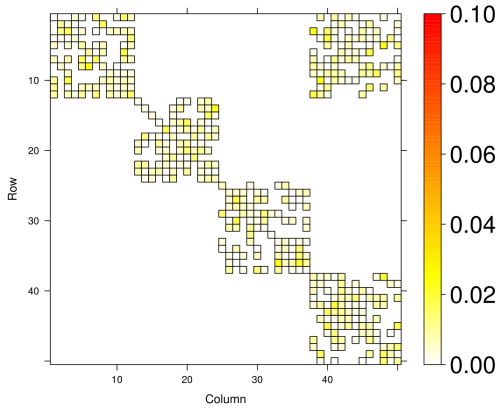

(c) Absolute difference of "Cluster" type

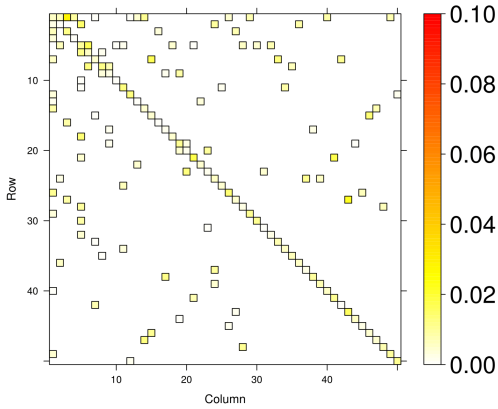

(d) Absolute difference of "Scale-free" type

Figure 2.9: Bootstrap median of 1,000 bootstrapped LASSLE estimates. Figure 2.9(a),(b) give the median of 1,000 bootstrapped LASSLE estimates for "Cluster" type and "Scale-free" type data. Figure 2.9(c),(d) demonstrate the absolute difference between the median estimated matrix and true coefficient matrix.

2.3.4 Robustness of LASSLE method

Previous simulation study are conducted under the assumption that ε_t, the noise of VAR(d) at time t, follows a multivariate Gaussian distribution. In addition to Gaussian noise, we

are interested to investigate whether the LASSLE method has better specificity, lower bias, lower variance (and thus lower MSE) than the LSE and LASSO methods for other noise distributions, e.g., student's t-noise (with low degree of freedom) and shifted χ^2 noise. To explore this, we generated time series datasets using Equation (1.2.1) under different VAR setting $\{P, d\}$ with P independent t-noise and P independent χ^2 noise respectively. Then we apply all three methods to estimate the VAR coefficient matrices under each setting and compare their performance in terms of both the specificity of true zero and the general mean squared error.

Results from student's t-noise

We use P independent $\sqrt{0.06} * t(5)$, of which mean equals to 0 and variance equals to 0.1, to generate the student's t-noise at time t. Figure 2.10 and 2.11 demonstrate the performance comparison of three methods on "Cluster" type and "Scale-free" type data regarding their specificity of true zero under setting $\{P = 50,\, d = 1\}$. The visualization results imply that LASSLE can capture the true zero coefficient substantially better than LSE. In addition, LASSLE has much lower absolute difference on non-zero coefficients compared to LASSO.

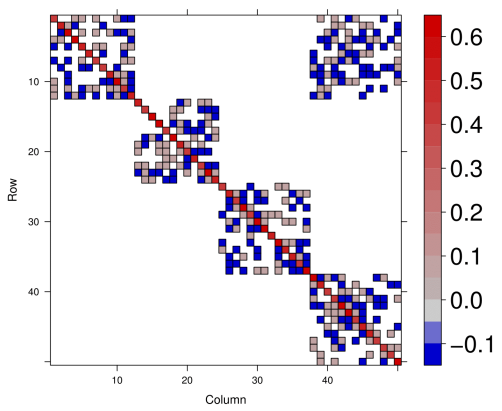

(a) "Cluster" type VAR matrix

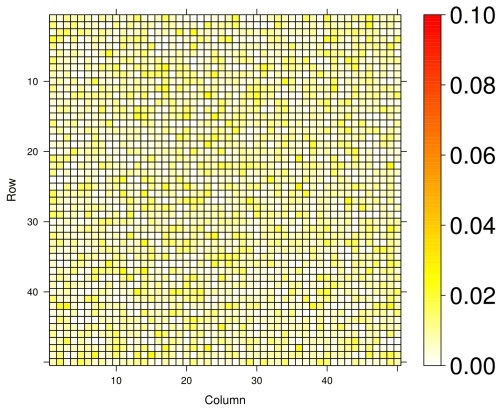

(b) Absolute difference of LSE

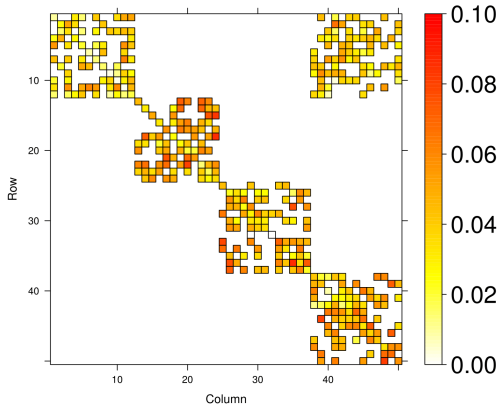

(c) Absolute difference of LASSO

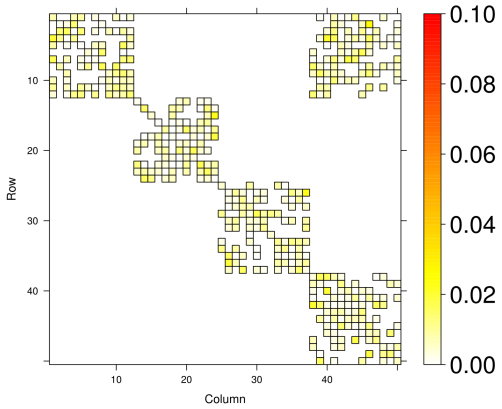

(d) Absolute difference of LASSLE

Figure 2.10: Comparison of specificity of true zero on "Cluster" type data with student's t-noise. Figure 2.10(a) demonstrates the true VAR(1) coefficient matrix with $P = 50$. Figure 2.10(b),(c),(d) give the absolute difference between true matrix and estimated matrix by LSE, LASSO and LASSLE method respectively.

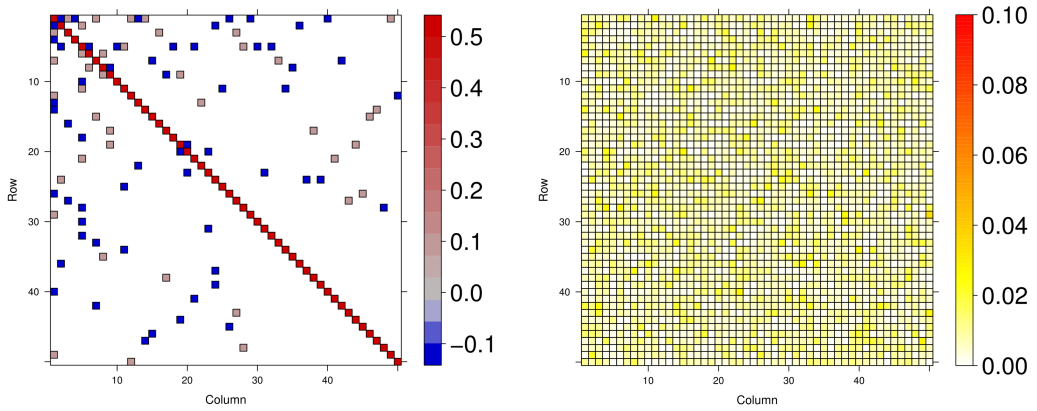

(a) "Scale-free" type VAR matrix (b) Absolute difference of LSE

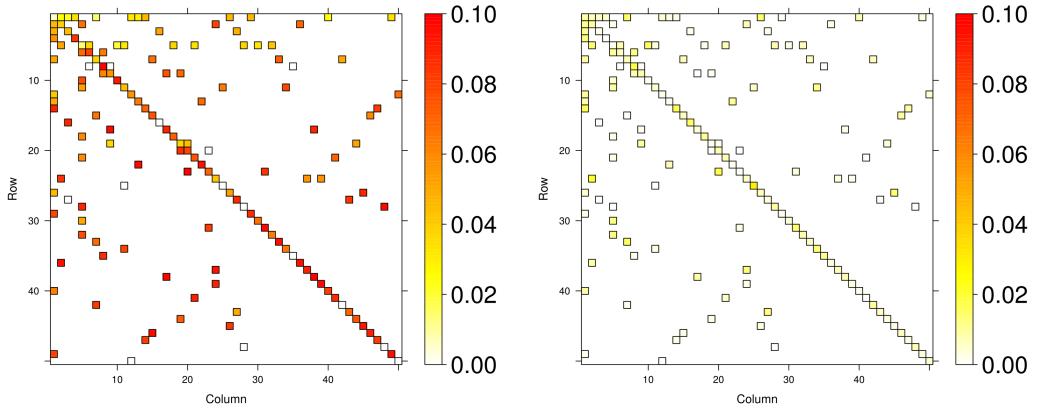

(c) Absolute difference of LASSO (d) Absolute difference of LASSLE

Figure 2.11: Comparison of specificity of true zero on "Scale-free" type data with student's t-noise. Figure 2.11(a) demonstrates the true VAR(1) coefficient matrix with $P = 50$. Figure 2.11(b),(c),(d) give the absolute difference between true matrix and estimated matrix by LSE, LASSO and LASSLE method respectively.

Table 2.3 and 2.4 list the MSE results of all three methods on both "Cluster" type and "Scale-free" type data with student's t-noise under different VAR parameter setting [2]. We can see that LASSLE method still has overwhelming advantage over LSE and LASSO when the number of parameter is large enough ($\geq 2,500$). On the other hand, LSE has slightly

[2] "*" indicates the method which gives the lowest MSE.

lower MSE than LASSLE under low-dimensional parameter setting.

VAR Parameter Setting			MSE $\times 10^{-3}$		
Number	P	d	LSE	LASSO	LASSLE
100	10	1	7 *	184	28
500	10	5	57 *	603	73
1,000	10	10	147 *	741	216
2,500	50	1	175	836	37 *
5,000	50	2	455	1242	98 *
10,000	100	1	686	1726	88 *

Table 2.3: Comparison of MSE for "Cluster" type data with student's t-noise

VAR Parameter Setting			MSE $\times 10^{-3}$		
Number	P	d	LSE	LASSO	LASSLE
100	10	1	6 *	134	11
500	10	5	44	278	12 *
1,000	10	10	124 *	728	217
2,500	50	1	181	778	50 *
5,000	50	2	450	1056	24 *
10,000	100	1	747	1641	160 *

Table 2.4: Comparison of MSE for "Scale-free" type data with student's t-noise

Results from shifted zero-mean χ^2 noise

To generate P-dimensional shifted χ^2 noise at time t, we employ P independent $\sqrt{0.0125} * \chi^2_4 - \sqrt{0.2}$, with mean of 0 and variance of 0.1. Figure 2.12 and 2.13 demonstrate the comparison results of three methods on "Cluster" type and "Scale-free" type data in terms of their specificity of true zero under setting $\{P = 50,\, d = 1\}$. Based on the visualization

results, we can see that LASSLE estimate has very good specificity of true zero coefficients regardless of χ^2 noise.

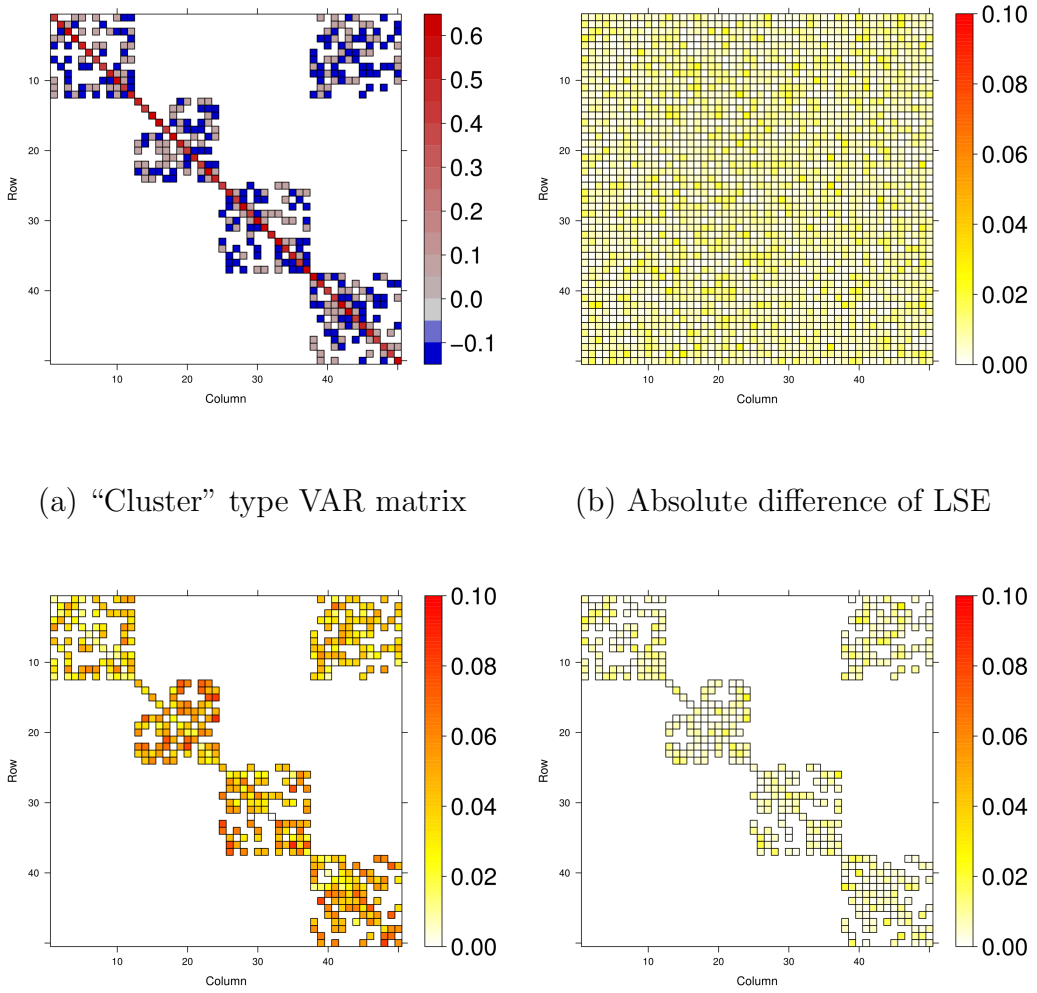

(a) "Cluster" type VAR matrix (b) Absolute difference of LSE

(c) Absolute difference of LASSO (d) Absolute difference of LASSLE

Figure 2.12: Comparison of specificity of true zero on "Cluster" type data with shifted zero-mean χ^2 noise. Figure 2.12(a) demonstrates the true VAR(1) coefficient matrix with $P = 50$. Figure 2.12(b),(c),(d) give the absolute difference between true matrix and estimated matrix by LSE, LASSO and LASSLE method respectively.

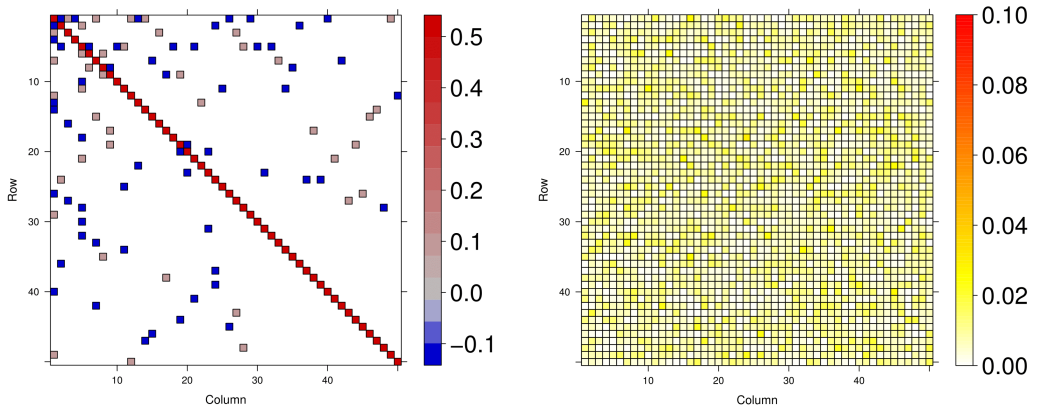

(a) "Scale-free" type VAR matrix (b) Absolute difference of LSE

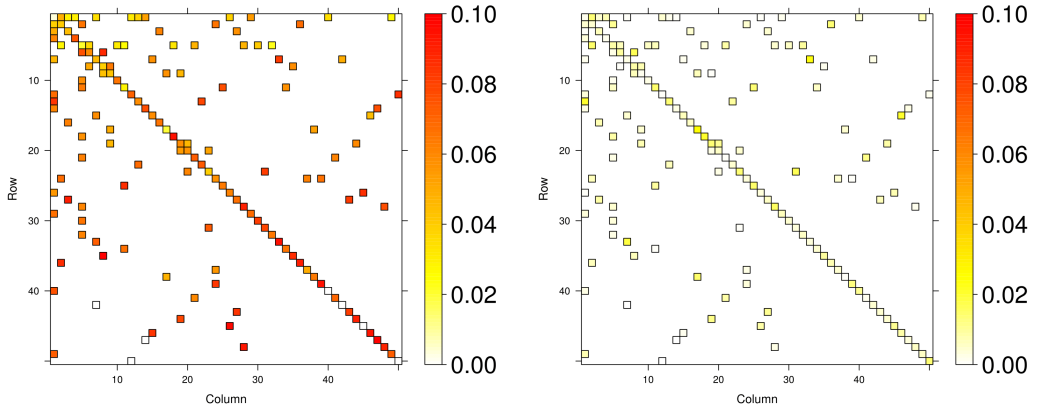

(c) Absolute difference of LASSO (d) Absolute difference of LASSLE

Figure 2.13: Comparison of specificity of true zero on "Scale-free" type data with shifted zero-mean χ^2 noise. Figure 2.13(a) demonstrates the true VAR(1) coefficient matrix with $P = 50$. Figure 2.13(b),(c),(d) give the absolute difference between true matrix and estimated matrix by LSE, LASSO and LASSLE method respectively.

Table 2.5 and 2.6 list the MSE results of all three methods on both "Cluster" type and "Scale-free" type data with shifted χ^2 noise under different VAR parameter setting. It implies that LASSLE method has significantly lower MSE under most high dimension parameter setting than LSE and LASSO.

VAR Parameter Setting			MSE $\times 10^{-3}$		
Number	P	d	LSE	LASSO	LASSLE
100	10	1	7 *	159	14
500	10	5	56	465	41 *
1,000	10	10	139	561	136 *
2,500	50	1	182	666	31 *
5,000	50	2	453	1039	75 *
10,000	100	1	696	1572	87 *

Table 2.5: Comparison of MSE for "Cluster" type data with shifted zero-mean χ^2 noise

VAR Parameter Setting			MSE $\times 10^{-3}$		
Number	P	d	LSE	LASSO	LASSLE
100	10	1	8	143	3 *
500	10	5	55	224	16 *
1,000	10	10	129 *	654	153
2,500	50	1	194	663	22 *
5,000	50	2	451	967	23 *
10,000	100	1	747	1291	40 *

Table 2.6: Comparison of MSE for "Scale-free" type data with shifted zero-mean χ^2 noise

2.4 Application to effective connectivity in multichannel LFPs

In this section, we will fit a VAR model to LFP data recorded from multiple electrodes as rats perform a non-spatial sequence memory task [3] and apply the LASSLE method to estimate the VAR parameters and consequently partial directed coherence. Our objective

is to examine and quantify potential connectivity (i,.e., effective) among electrodes located in hippocampal region CA1. We specifically focused our analyses on LFPs from $P = 12$ tetrodes, a subset of electrodes that also recorded clear single-cell spiking activity and were confirmed to be located in the pyramidal layer of CA1 (see estimated tetrode locations in Figure 1.4).

2.4.1 Preliminary analysis of a single epoch

We first demonstrate fitting the VAR model to to a single epoch (Epoch 10 in this example). To select the best lag order $\widehat{d}$, we fit a VAR(d_j) model with candidate order $d_j \in \{1, 2, ..., 12\}$ and use LSE to estimate the coefficient matrices. Then we apply Equation (2.2.17), (2.2.18), and (2.2.19) to compute AIC for each candidate order d_j. For epoch 10, the best order (or the minimizer of AIC) was $\widehat{d} = 3$. Consequently there were 3 coefficient matrices (each of dimension 12 x 12) to estimate.

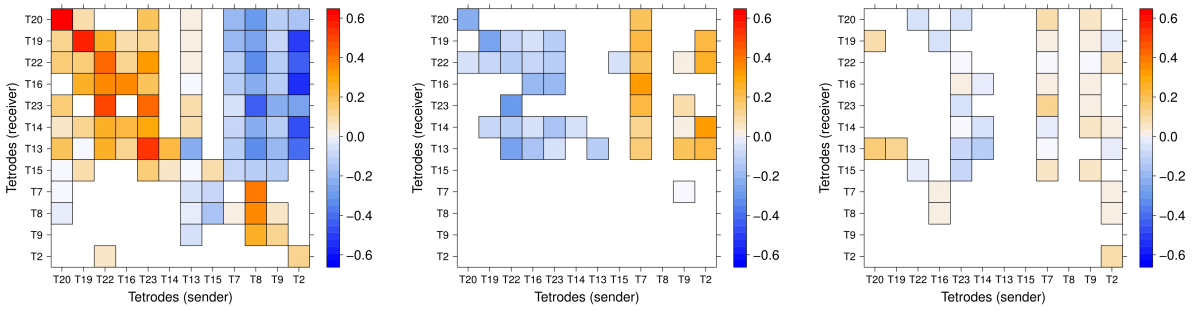

(a) Estimated Φ_1 (b) Estimated Φ_2 (c) Estimated Φ_3

Figure 2.14: Estimated coefficient matrices Φ_1, Φ_2, Φ_3 in Epoch 10 using the LASSLE method.

Figure 2.14 shows the LASSLE estimates of Φ_1, Φ_2 and Φ_3 for Epoch 10. Blanks are assigned to entries whose value is zero, so non-dependence between tetrodes is easy to tell. For entries whose value is not zero, we assign them with colors of red for positive value and blue for

negative value, and the strength of dependence is implied by the color-key. As we can see, most diagonal entries of Φ_1 are either red or orange, which implies that signals have strong positive auto-dependence. In addition, upper off-diagonal entries in column 9 to 12 of Φ_1 are mostly blue, which could be evidence that signal of tetrode T7, T8, T9 and T2 at time $t-1$ has significant negative dependence with signals from other tetrodes location at time t. Compared to Φ_1, more than half entries in Φ_2 are blank, suggesting there is no auto- and cross-dependence between those tetrodes at time $t-2$ and at time t. Column 1 to 8 in Φ_2 are light blue, which implies weak negative dependence between signals from tetrode T20, T19,..., T15 at time $t-2$ and signals from these tetrodes location at time t. Also, we believe there is positive dependence between signals from tetrode T7, T9, T2 at time $t-2$ and signals from tetrode T20, T19, ..., T13 at time t as the color of column 9, 11 and 12 in Φ_2 is orange. However, most entries of Φ_3 are blank and limited non-zero estimates are close to zero, which implies that the dependence between LFPs at time $t-3$ and time t is very weak.

Next we applied Equation (2.2.15) and (2.2.16) to the LASSLE estimates to calculate partial directed coherence. PDC was computed at the following frequency bands in the study: δ band (0-4 Hertz), θ band (4-8 Hertz), α band (8-12 Hertz), β band (12-32 Hertz) and γ band (32-50 Hertz), which are standard in brain signals analysis. To estimate PDC at specific frequency band, we calculate the average of estimates of PDC over all singleton frequencies in that band. Figure 2.15 demonstrates the estimated PDC results of these frequency bands in Epoch 10. Since there is only slight change on the estimated PDC across different frequency bands, we use the results of the γ band (shown in Table 2.7) as representative to explain the PDC. For tetrodes T16, T14, T13, T15, T7 and T9, over 75% of their information can be explained by their own past while most of their information flowing to other tetrodes are very close to 0. More specifically, tetrode T14 has 2.4% information that flows to tetrode T13, and 6.1% information of tetrode T16 flows to tetrode T14. This implies that they tend to have communication with specific tetrodes instead of the entirety. Unlike these tetrodes,

tetrodes T20, T19, T22, T23, T8 and T2 have significant amount of information flowing to other tetrodes. For example, the proportion of current tetrode T8 that is explained by its own past is only about 30.0%. This could be evidence that these tetrodes play an important role of passing information to other tetrodes while the rat was engaged in a non-spatial memory task. Estimated PDCs from tetrodes T20, T19, T22, T16, T23, T14, T13, T15 (sender) to tetrodes T7, T8, T9, T2 (receiver) are almost none (the blank on the bottom left of PDC), which suggest that previous oscillatory activity at the γ band of first 8 tetrodes can hardly explain future oscillatory activity at the γ band of last 4 tetrodes as they are far apart in spatial distance.

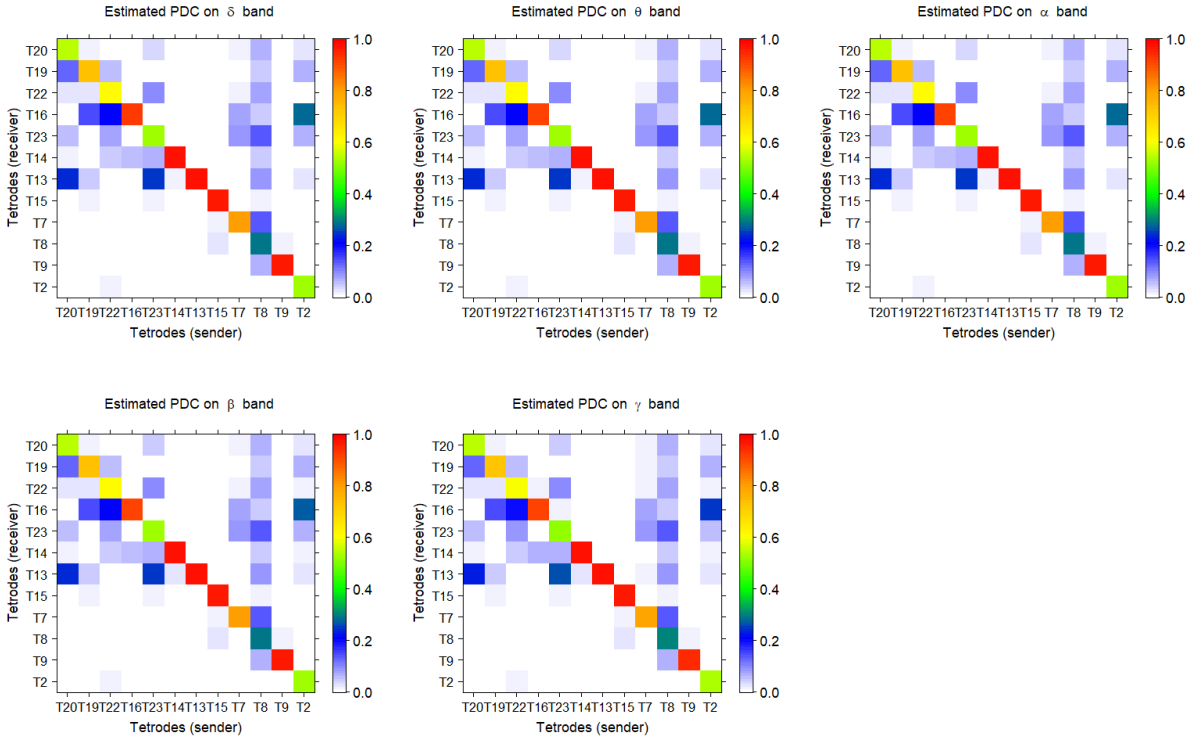

Figure 2.15: Estimated PDC by LASSLE of Epoch 10

Tetrode (reciever)	Tetrode (sender)											
	T20	T19	T22	T16	T23	T14	T13	T15	T7	T8	T9	T2
T20	0.548	0.019	0.005	0.000	0.041	0.000	0.002	0.000	0.018	0.060	0.004	0.021
T19	0.126	0.734	0.054	0.005	0.003	0.000	0.001	0.000	0.011	0.048	0.002	0.062
T22	0.026	0.026	0.593	0.010	0.091	0.000	0.001	0.003	0.017	0.078	0.006	0.019
T16	0.000	0.147	0.200	0.909	0.010	0.000	0.000	0.000	0.073	0.041	0.009	0.252
T23	0.056	0.000	0.085	0.000	0.513	0.000	0.007	0.000	0.082	0.139	0.007	0.058
T14	0.010	0.007	0.043	0.061	0.068	0.971	0.006	0.000	0.001	0.042	0.004	0.019
T13	0.232	0.048	0.008	0.003	0.258	0.024	0.979	0.000	0.009	0.081	0.004	0.029
T15	0.000	0.019	0.000	0.000	0.016	0.005	0.000	0.962	0.002	0.014	0.004	0.000
T7	0.000	0.000	0.000	0.006	0.000	0.000	0.001	0.010	0.786	0.133	0.002	0.002
T8	0.001	0.000	0.000	0.006	0.000	0.000	0.001	0.025	0.001	0.300	0.012	0.002
T9	0.000	0.000	0.000	0.000	0.000	0.000	0.002	0.000	0.000	0.063	0.946	0.000
T2	0.000	0.000	0.012	0.000	0.000	0.000	0.000	0.000	0.000	0.000	0.000	0.536

Table 2.7: Estimated PDC value at the γ band in Epoch 10. The estimated PDC from tetrode T16 to tetrode T22 is 0.010. The estimated PDC from tetrode T22 to T16 is 0.200.

2.4.2 Change of brain connectivity across epochs

We repeat the same procedure for all epochs and select the best VAR order separately. Figure 2.16 demonstrates the AIC curves of the first 15 epochs, from which we can see some epochs reach the lowest AIC at $\widehat{d} = 3$ and some of them are $\widehat{d} = 4$. Table 2.8 shows the distribution of $\widehat{d}$ across all 247 epochs. We fit VAR($\widehat{d}$) to each epoch and estimate the corresponding coefficient matrices by LASSLE method. Figure 2.17 shows the boxplots of ACF and PACF of residuals fitted from tetrode T22 across all 247 epochs, which is strong evidence that the residuals from tetrode T22 are white noise. The same phenomenon is observed for residuals fitted from other tetrodes.

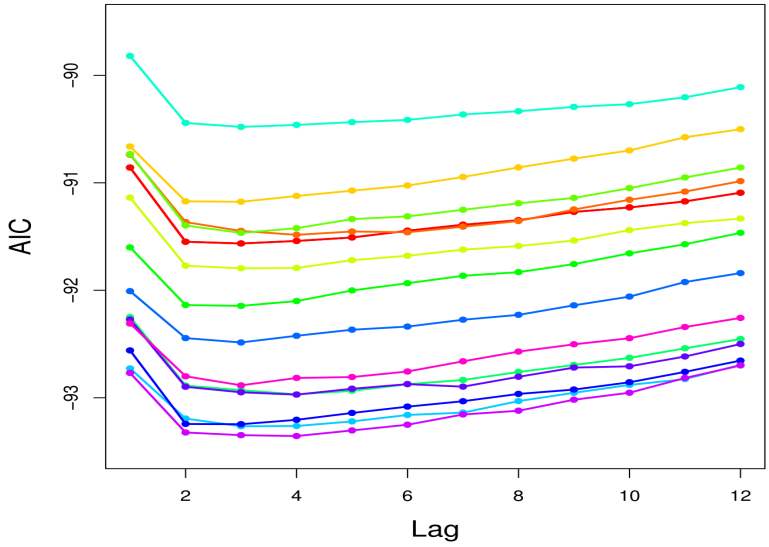

Figure 2.16: AIC of fitted VAR on first 15 epochs, lag order range: 1,2,...,12.

Selected lag order	2	3	4	5
Number of epochs	64	158	23	2
Proportion (%)	25.9	64.0	9.3	0.8

Table 2.8: Distribution of selected VAR lag order

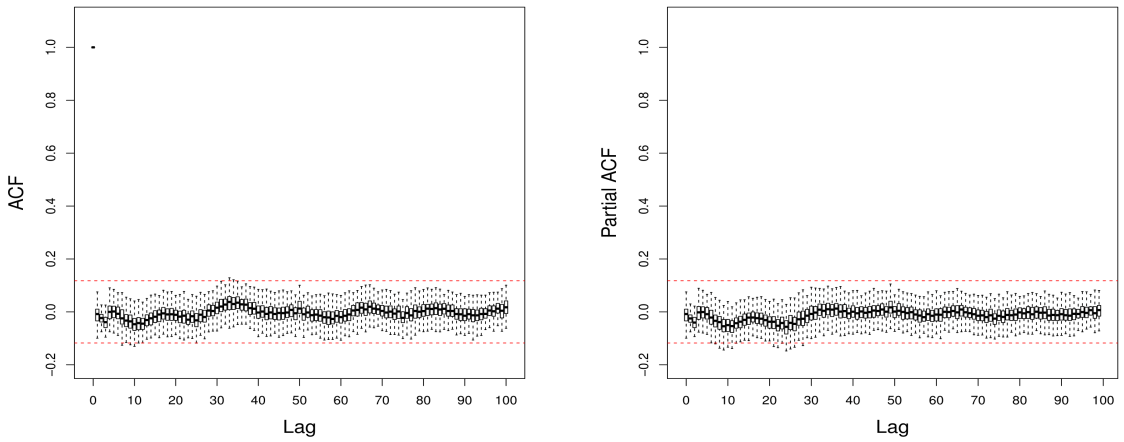

Figure 2.17: The boxplots of auto-correlation function (ACF) of residuals fitted from tetrode T22 across all epochs (left). The boxplots of partial auto-correlation function (PACF) of residuals fitted from tetrode T22 across all epochs (right).

After computing all the PDCs, we obtain the 95% confidence interval of PDC by summarizing from the empirical distribution if we assume all epochs carry the same connectivity information. However, this assumption may not be true and we are more interested in the variation of PDCs across all epochs, which can help us understand the dynamics of rat's brain connectivity in this memory experiment. To visualize the evolution, we develop Figure 2.18 and Figure 2.19, where PDC matrix (12×12) is converted to a column vector of $12 \times 12 = 144$ elements at each epoch and x-axis indicates the index of epochs. We can clearly see that estimated PDCs at the γ band are quite stable on some tetrode pairs, e.g., tetrode T13 to tetrode T13 (always red color), while PDC estimates of other tetrode pairs are varying with epochs.

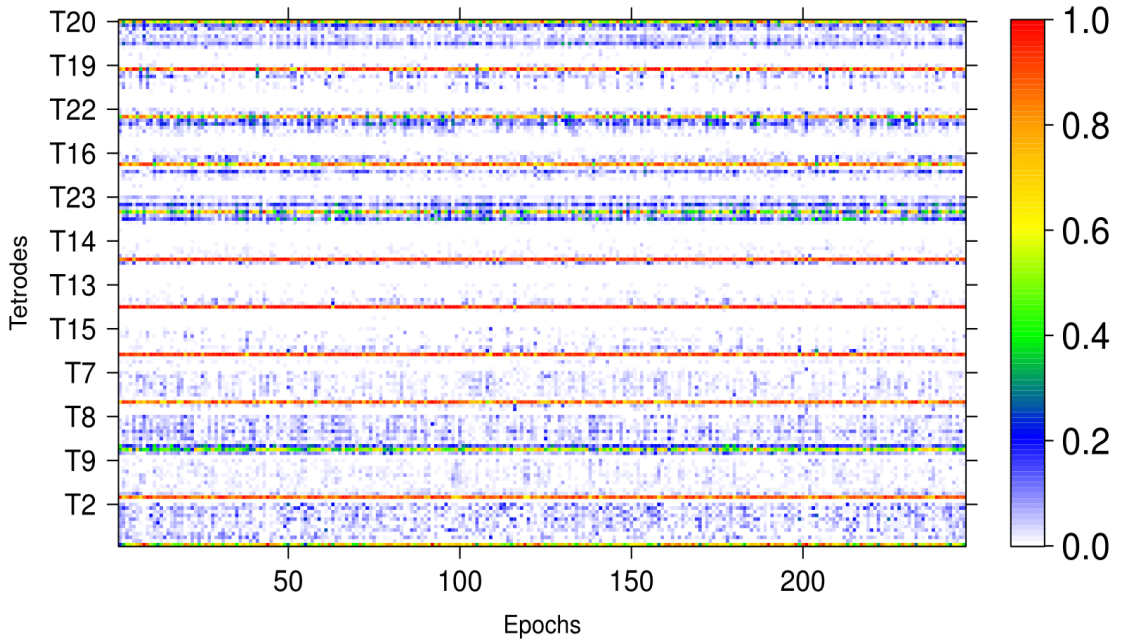

Figure 2.18: PDC on γ band across all epochs. X-axis is the index of epochs. At each epoch, PDC matrix (12×12) is converted to a column vector of $12 \times 12 = 144$ elements, where every 12 elements are the PDC values of one tetrode to all 12 tetrodes.

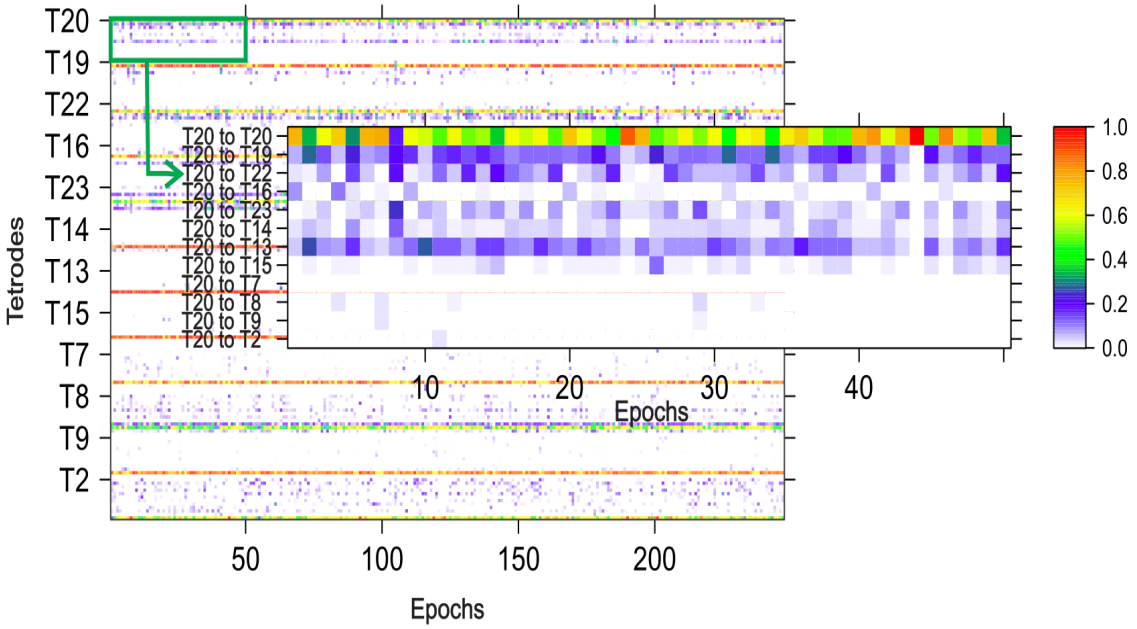

Figure 2.19: Illustration of Figure 2.18. Every 12 rows in Figure 2.18 indicate the PDCs from one tetrode to all 12 trodes across 247 epochs. For example, the first 12 rows demonstrate the PDCs from T20 to T20, T19, ..., T2 at all epochs.

To compare the variation of estimated PDCs at the γ band between InSeq epochs and OutSeq epochs, the Kolmogorov-Smirnov (KS) test is used [30]. The null hypothesis of KS test is that the empirical distribution of PDCs from InSeq epochs and that of OutSeq epochs are identical. Here we use permutation to obtain the empirical distribution of KS test statistics. Since it is necessary to preserve the inherent correlation across different epochs, the entire 247 epochs were partitioned into 50 groups where 5 consecutive epochs are within the same group (for the last group, we replicate Epoch 246 and Epoch 247 to make 5 epochs). This idea is inspired by the block bootstrap procedure for time series. Then, we randomly selected 5 groups (containing 25 epochs) from 50 groups as experimental OutSeq epochs, using the rest as experimental InSeq epochs, and compute the KS-statistic for this new Inseq and OutSeq grouping. This procedure is repeated 10,000 times to obtain the empirical distribution of KS-statistics. Finally, the proportion of permuted KS-statistics with larger values than the real KS-statistic is used as the p-value.

Figure 2.20 and Figure 2.21 demonstrate the empirical distributions of estimated PDCs for all tetrodes given by Inseq epochs (blue curve) and Outseq epochs (red curve). Based on the p-values of KS test, there is strong evidence showing that the variation of auto-PDC of tetrode T19, T22, T23 and T13 are different between Inseq epochs and Outseq epochs (Figure 2.20). For these tetrodes, the proportion of their current oscillatory activity that can be explained by their own past activity is influenced by whether odors are presented in the correct or incorrect sequence position (Inseq or Outseq, respectively). However, for the remaining tetrodes the variation in their estimated auto-PDC is quite stable across Inseq epochs and Outseq epochs. As shown in Figure 2.21, p-values also indicate that the variation of estimated PDC from tetrode T19, T22 and T23 (sender) to some other tetrodes (receiver) are significantly different between Inseq epochs and Outseq epochs, which suggests that the information flowing from these tetrode locations to others is also influenced by the Inseq/Outseq status of the presented odor.

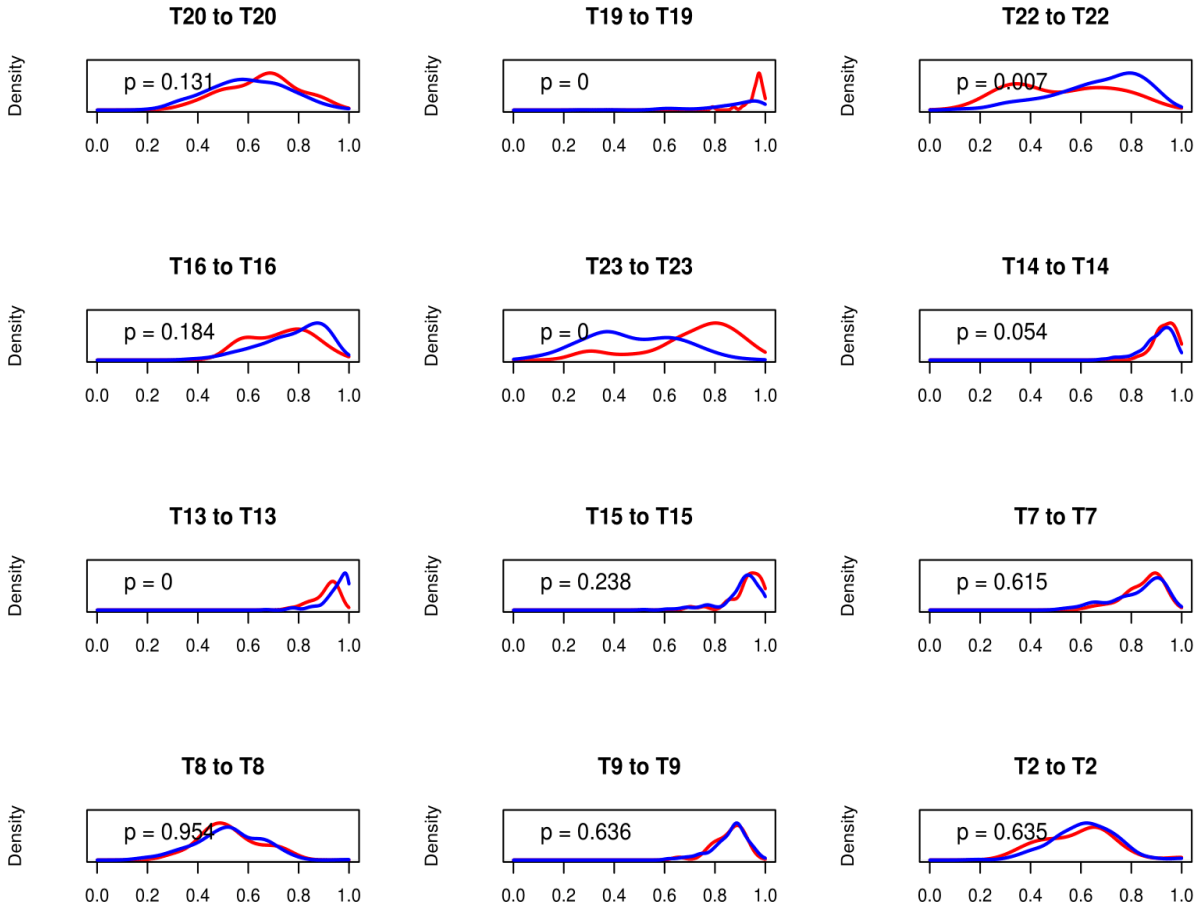

Figure 2.20: Density curves of auto-PDCs across all 247 epochs. Blue one is the density curve of InSeq epochs only. Red one is the density curve of OutSeq epochs only. Kolmogorov-Smirnov test is used, where the null hypothesis is that two empirical distributions are the same. P-value is obtained from permutation and we reject the null hypothesis when $p <= 0.05$.

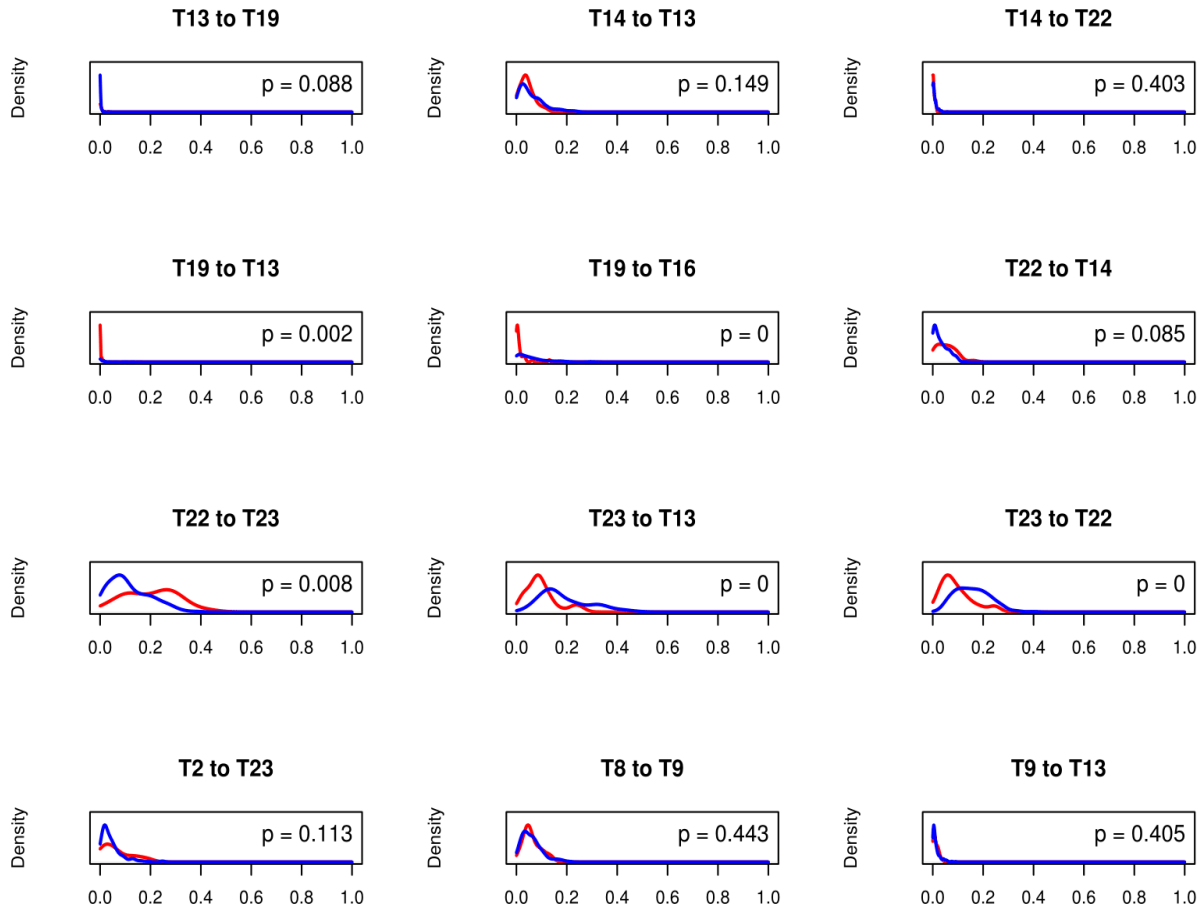

Figure 2.21: Density curves of some cross-PDCs across all 247 epochs. Blue one is the density curve of InSeq epochs only. Red one is the density curve of OutSeq epochs only. Kolmogorov-Smirnov test is used, where the null hypothesis is that two empirical distributions are the same. P-value is obtained from permutation and we reject the null hypothesis when $p <= 0.05$.

2.4.3 Comparison of three methods on PDC across all epochs

We also apply traditional methods (LSE only and LASSO only) to estimate VAR coefficients and then compute the PDC for each epoch separately. Figure 2.22 and Figure 2.23 demonstrate the density curve of auto-PDCs and some cross-PDCs estimated by three methods across all epochs. The red curve is given by LASSLE method, the blue one is via LSE, and

the green one is achieved by LASSO. As we can see, the red curve is close to the blue one for most PDCs. This is because each estimated PDC is mostly influenced by some dominant non-zero VAR coefficients, of which the estimates are close to each other by LASSLE and LSE separately. Noted that LASSO method has shrinked many VAR coefficients to zero and its non-zero estimates are very different from those by LSE. Cosequently the green curve is dissimilar to the blue one for most PDCs.

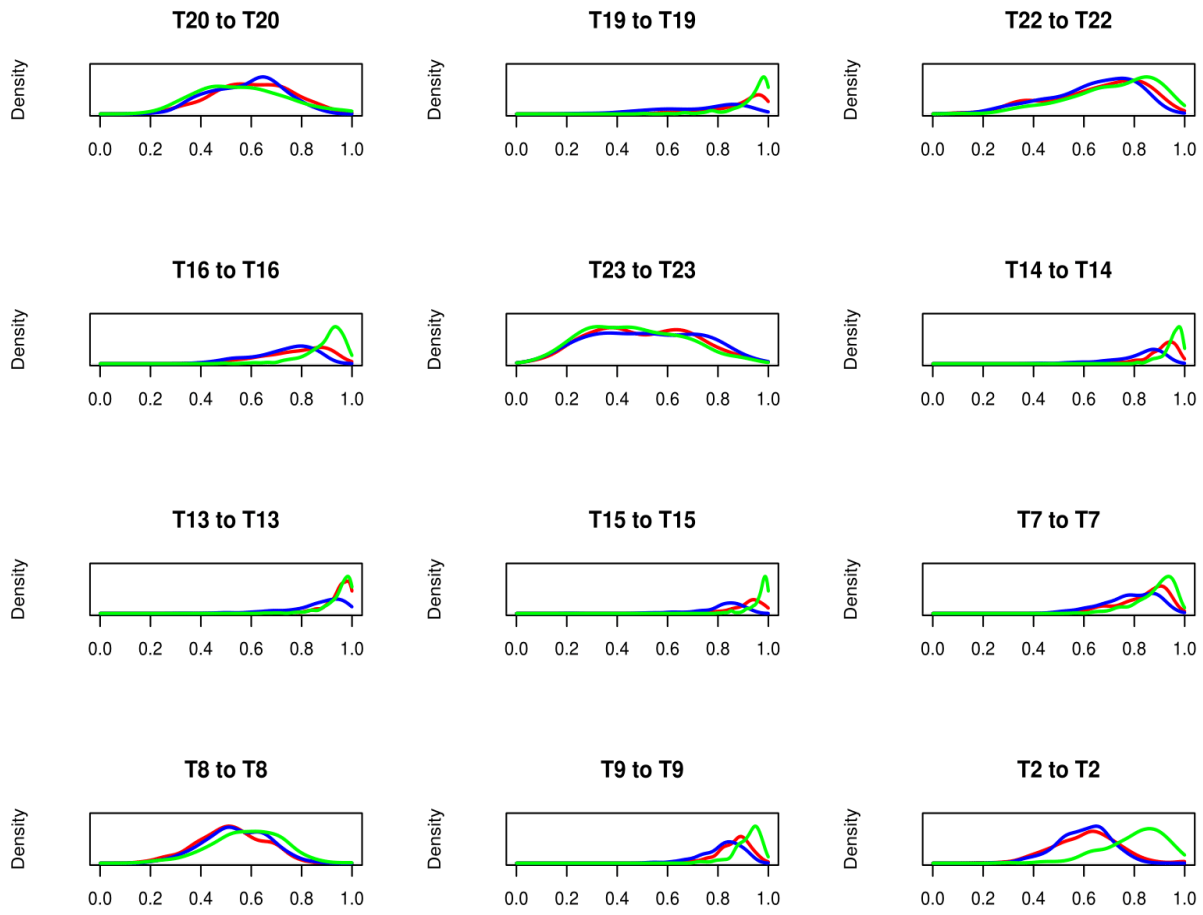

Figure 2.22: Density curves of auto-PDCs across all 247 epochs given by three methods. The red curve is LASSLE, the blue one is LSE, and the green one is LASSO.

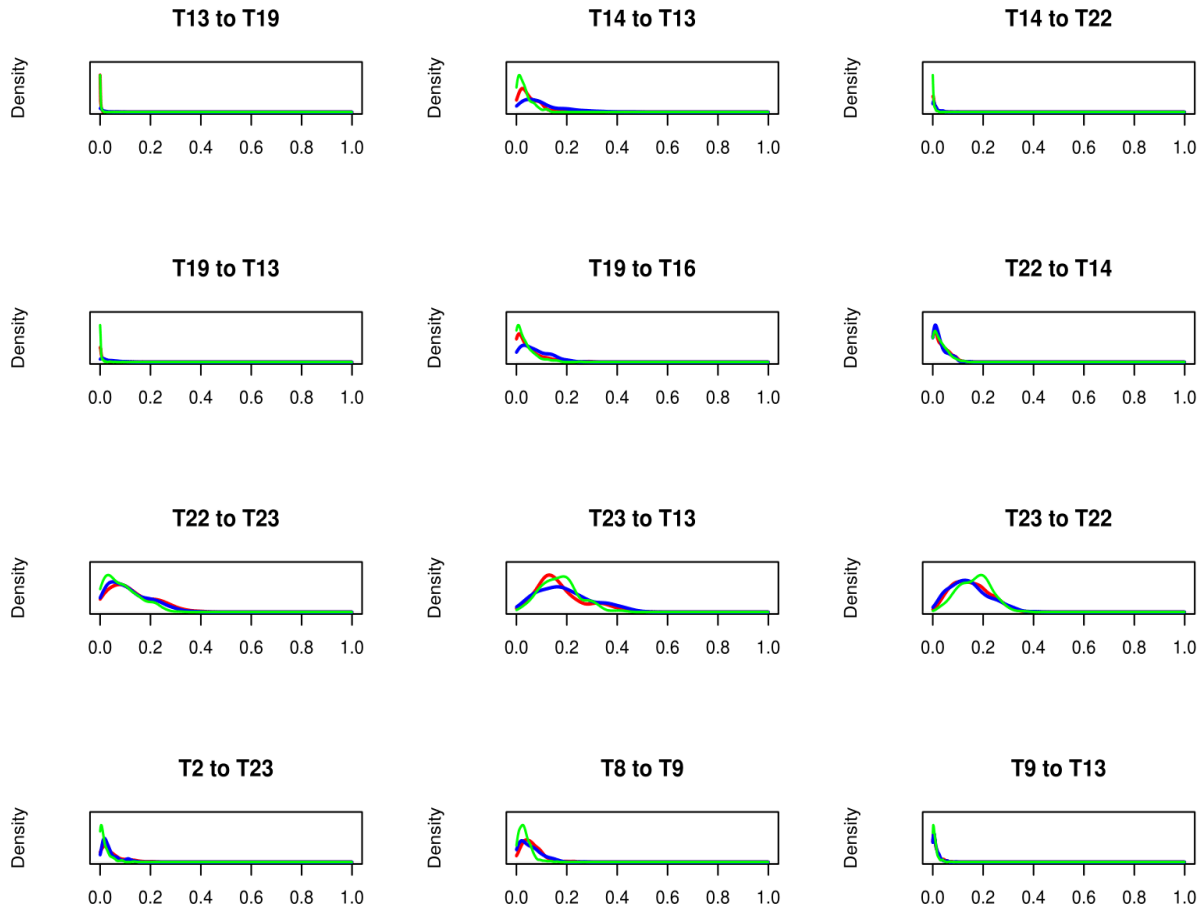

Figure 2.23: Density curves of some cross-PDCs across all 247 epochs given by three methods. The red curve is LASSLE, the blue one is LSE, and the green one is LASSO.

2.5 Conclusion

In this chapter, we proposed a hybrid LASSLE (LASSO+LSE) method to estimate the coefficients of vector auto-regressive models characterizing the effective and directional connectivity for multichannel brain physiological signals. This method uses regularization to control for sparsity on the first stage and then use least squares to improve bias and mean-squared error of the estimator on the second stage. Compared to the separate LASSO and LSE, the advantage of our method is that it is able to both indicate the most important

effective connectivity and give a more accurate estimate of the connectivity strength. Note that sparse VAR coefficient estimates can still capture complex dependency structures in a multivariate time series. In addition, we employ partial directed coherence to measure the directional connectivity between the channels. PDC is a directed frequency-specific measure that explains the extent to which the present oscillatory activity in a sender channel influences the future oscillatory activity in a specific receiver channel relative to all possible receivers in the network. The proposed modeling approach provided key insights into potential functional relationships among simultaneously recorded sites during performance of a complex memory task. Specifically, this novel method was successful in revealing patterns of effective connectivity across tetrode locations, by quantifying how present oscillatory activity in each tetrode is influenced by past oscillatory activity in other tetrodes. This approach was also successful in capturing how this effective connectivity varied across trial epochs and trial types (InSeq or OutSeq).

Chapter 3

Characterizing hippocampal connectivity in multi-trial LFPs

3.1 Introduction

To analyze multi-trial LFPs at condition level, we have proposed a two-stage modeling approach in Chapter 2 where vector auto-regressive (VAR) models are employed to characterize each individual trial separately and estimate trial-specific connectivities in the first stage, then estimate the between-conditions variation of the estimated connectivities in the second stage. However, this approach has some drawbacks. First of all, the parameter estimation procedure does not take into account the similarity of connectivity structure within same condition, since trials from same experimental condition are modeled and estimated separately. Secondly, summarizing and making inference on the condition-level effective connectivity is accomplished via bootstrap analysis, where random variability at trial level is introduced but not accounted for by re-sampling residuals. In this chapter, we address those deficiency by employing a Bayesian hierarchical vector autoregressive (BH-VAR) framework [9]. By

imposing condition-level priors on the parameters in trial-specific models, the proposed modeling approach allows to incorporate within-conditions correlation with between-conditions variation. The prior information will help better characterize trial- and condition-level connectivity through the posterior distribution. Moreover, inference on trial- and condition-level connectivity can be made simultaneously in our single modeling framework, without the loss of information implied by a two-stage estimation approach. We further take into account the potential sparse structure in high dimensional parameter space of brain signals by inducing sparsity in parameters via "spike-and-slab" mixture priors.

To describe condition-specific effective connectivities, we shall still use partial directed coherence, which is a connectivity measurement in frequency domain. Compared to the connectivity simply characterized by coefficients of VAR matrices, PDC provides a perspective to understand the connectivity at conditional level as to how an oscillatory activity (at a particular frequency band) at a present time in one channel may impact oscillatory activity of the same frequency band at another channel at a future time point. The remainder of this chapter is arranged as follows. In Section 3.2, I present the details of proposed hierarchical Bayesian models followed by simulation studies in Section 3.3. Analysis of LFP signals is in Section 3.4 and Conclusion is in Section 3.5.

3.2 A Bayesian hierarchical VAR model for differential connectivity

3.2.1 Single stage modeling

A P-dimensional LFP signal from trial s under condition g is said to follow a Bayesian hierarchical VAR model of order d, denoted as BH-VAR(d), if it can be expressed as

$$(\mathbf{X}_t^{(s)}|\eta_s = g, \Phi_{\ell,g}^{(s)}, \Sigma) = \sum_{\ell=1}^{d} \Phi_{\ell,g}^{(s)} \mathbf{X}_{t-\ell}^{(s)} + \varepsilon_t^{(s)} \quad t = d+1, .., T \tag{3.2.1}$$

where η_s is a condition indicator, $s = 1, ..., n$, and $g = 1, ..., G$. The matrices $\Phi_{\ell,g}^{(s)}$'s $\in \mathfrak{R}^{P\times P}$ are the autoregressive coefficient matrices of trial s from condition g, which capture lagged cross-dependence among signals from different channels in trial s. We assume $\varepsilon_t^{(s)} \overset{iid}{\sim} N(\underline{0}, \Sigma)$ for the noise of trial s, where $\Sigma = \text{diag}\{\sigma_1, ..., \sigma_P\}$ is the VAR covariance matrix with hyper priors $\sigma_j \sim IG(h_1, h_2)$ $(j = 1, ..., P)$ placed on σ_j's. Priors $p(\Phi_{\ell,g}^{(s)}|\Phi_{\ell,g})$ $(\ell = 1, ..., d)$ are imposed to account for the between-trials variation on VAR matrices under condition g, where $\{\Phi_{\ell,g}\}_{\ell=1}^{d}$ indicate the condition-specific coefficient matrices. An illustration of condition-specific connectivity via the BH-VAR model can be found in Figure 3.1. Denote the LFP recording of neurons to be u-th and v-th tetrode. Then the entry $\Phi_{\ell,g}^{uv}$ $(g = 1, 2)$ shows the impact of the input from v-th tetrode at time $t - \ell$ to brain activity at u-th tetrode at the current time t under condition g. If $\Phi_{\ell,g}^{uv} = 0$ and $\Phi_{\ell,g}^{vu} = 0$ for all lags ℓ then, there is no connectivity between these two tetrodes as determined by the BH-VAR model under condition g. Thus, the entries of $\{\Phi_{\ell,g}\}_{\ell=1}^{d}$ contain all the information about brain connectivity between channels under condition g.

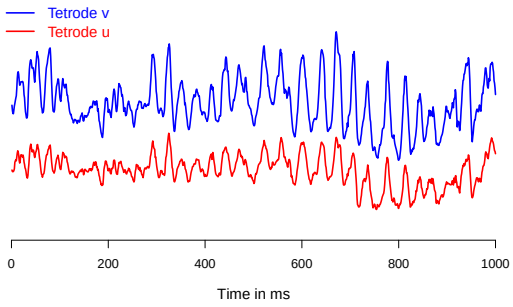

(a) LFP traces of Epoch 10 ($g = 1$)

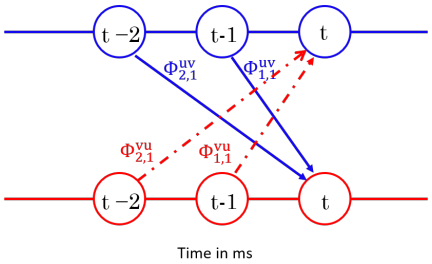

(b) Lagged dependence in $\Phi_{\ell,1}$'s

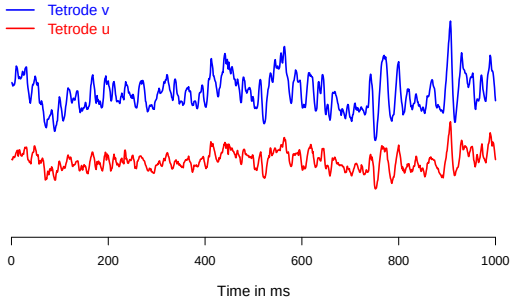

(c) LFP traces of Epoch 121 ($g = 2$)

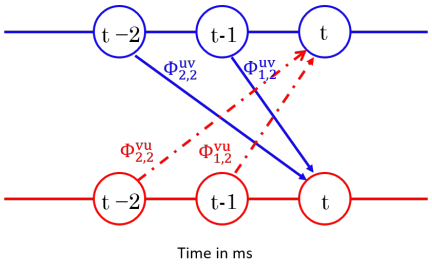

(d) Lagged dependence in $\Phi_{\ell,2}$'s

Figure 3.1: LFP traces and VAR. $\Phi^{uv}_{\ell,g}$ ($\ell = 1, 2$) captures the impact of the input from v-th channel at time $t - \ell$ to brain activity at u-th channel at the current time t from condition g.

Note that model (3.2.1) can be written in a standard multivariate linear regression form

$$\underbrace{\begin{bmatrix} (\mathbf{X}_T^{(s)})' \\ \vdots \\ (\mathbf{X}_{d+1}^{(s)})' \end{bmatrix}}_{Y^{(s)}:(T-d)\times P} = \underbrace{\begin{bmatrix} (\mathbf{X}_{T-1}^{(s)})' & \cdots & (\mathbf{X}_{T-d}^{(s)})' \\ \vdots & \ddots & \vdots \\ (\mathbf{X}_{d}^{(s)})' & \cdots & (\mathbf{X}_{1}^{(s)})' \end{bmatrix}}_{\mathbb{X}^{(s)}:(T-d)\times Pd} \underbrace{\begin{bmatrix} (\Phi_{1,g}^{(s)})' \\ \vdots \\ (\Phi_{d,g}^{(s)})' \end{bmatrix}}_{B_g^{(s)}:Pd\times P} + \underbrace{\begin{bmatrix} (\varepsilon_T^{(s)})' \\ \vdots \\ (\varepsilon_{d+1}^{(s)})' \end{bmatrix}}_{E^{(s)}:(T-d)\times P}. \tag{3.2.2}$$

Use the *vec* notation

$$\mathbf{y}^{(s)} = vec(Y^{(s)})$$
$$\beta_g^{(s)} = vec(B_g^{(s)})$$

$$e^{(s)} = vec(E^{(s)})$$

where $vec(Y^{(s)})$ stacks the columns of $Y^{(s)}$ on tops of one another. Then we must have

$$\underbrace{\mathbf{y}^{(s)}}_{(T-d)P\times 1} = (\underbrace{I}_{P\times P} \otimes \underbrace{\mathbb{X}^{(s)}}_{(T-d)\times Pd}) \underbrace{\beta_g^{(s)}}_{P^2d\times 1} + \underbrace{e^{(s)}}_{(T-d)P\times 1} \tag{3.2.3}$$

where $e^{(s)} \sim N(\underline{0}, \Sigma \otimes I)$. Eventually we can write model (3.2.1) as

$$(\mathbf{y}^{(s)}|\eta_s = g, \beta_g^{(s)}, \Sigma) \sim N((I \otimes \mathbb{X}^{(s)})\beta_g^{(s)}, \Sigma \otimes I) \tag{3.2.4}$$

with $\beta_g^{(s)}$ capturing the trial-level connectivities.

Here we adopt the model in [9] and [19], and propose to model the condition-level connectivities φ_g (vectorized VAR matrices at condition g). Multivariate normal priors are put on $\beta_g^{(s)}$:

$$(\beta_g^{(s)}|\varphi_g, \Xi_g) \sim N(\varphi_g, \Xi_g) \tag{3.2.5}$$

The trial-level connectivities under condition g are modeled as random derivations from the baseline process of condition g, where $\Xi_g = \text{diag}\{\xi_{g,1}, ..., \xi_{g,dP^2}\}$ is a diagonal covariance matrix to account for the variation.

In particular, we enforce sparsity in the condition-level connectivity structure by imposing "spike-and-slab" mixture priors [36, 17, 18] on elements of φ_g. By weeding out less important parameters, we also aim at improving the accuracy of estimated effective connectivity. Denote elements of φ_g by $\{\varphi_{g,k}\}_{k=1,...,dP^2}$, we introduce binary indicators $\{\gamma_{g,k}\}_{k=1,...,dP^2}$, which satisfy $\gamma_{g,k} = 1$ if $\varphi_{g,k}$ is non-zero and $\gamma_{g,k} = 0$ otherwise. Then our "spike-and-slab" priors

are defined as following

$$(\varphi_{g,k}|\gamma_{g,k}) \sim \gamma_{g,k} N(0, \tau_0^2) + (1 - \gamma_{g,k})\delta_0(\varphi_{g,k}) \tag{3.2.6}$$

where $\delta_0(\varphi_{g,k})$ is a point mass density at $\varphi_{g,k} = 0$, and τ_0^2 is constant. Taking into account the potential difference in variation of zero and non-zero elements of trial-level parameters $\beta_g^{(s)}$ in Equation (3.2.5), we also put priors on the diagonal elements of Ξ_g to differentiate the variances conditional on zero and non-zero elements of φ_g. If $\gamma_{g,k} = 1$, we set $\xi_{g,k} = c_g^1 \sim IG(a_g^1, b_g^1)$; if $\gamma_{g,k} = 0$, $\xi_{g,k} = c_g^0 \sim IG(a_g^0, b_g^0)$, where $(a_g^1, b_g^1, a_g^0, b_g^0)$ are constants. Furthermore, we impose Bernoulli priors on the variable selection indicator $\gamma_{g,k}$

$$(\gamma_{g,k}|p_g) \sim Bern(p_g), \quad k = 1, ..., dP^2 \tag{3.2.7}$$

p_g is the probability of non-zero VAR parameters at condition-level and follows $p_g \sim Beta(\alpha_g^1, \alpha_g^2)$. The value of (α_g^1, α_g^2) is informed via prior information on the proportion of non-zero dependence of LFPs. The graphical structure of our proposed BH-VAR model can be found in Figure 3.2. Nodes in circles denote parameters, while nodes in squares denote observables based on LFPs.

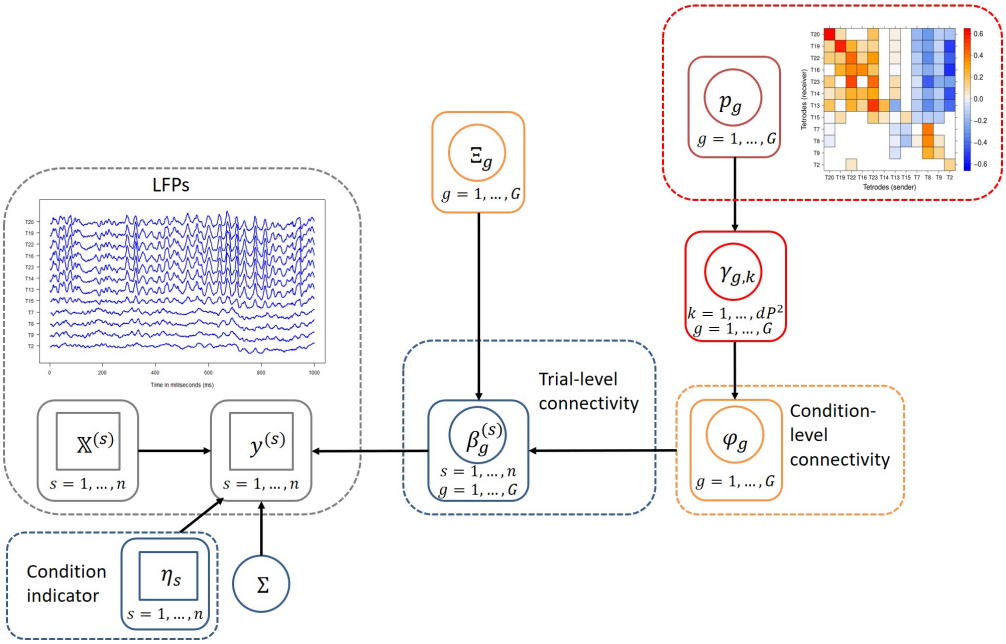

Figure 3.2: Graphical structure of the proposed probabilistic model in BH-VAR. Nodes in circles denote parameters, and nodes in squares denote observables based on LFPs.

Algorithm 3 MCMC Algorithm

1: Update $\beta_g^{(s)}$: Gibbs step from a normal distribution $\beta_g^{(s)} \sim N(\mu_\beta^{(s)}, v_\beta^{(s)})$

2: Jointly update (φ_g, γ_g) using a joint Metropolis-Hastings step

3: Update c_g^1 from $c_g^1 \sim IG(\chi_g^1, \psi_g^1)$, this is a Gibbs step

4: Update c_g^0 from $c_g^0 \sim IG(\chi_g^0, \psi_g^0)$, this is a Gibbs step

5: Update p_g from $p_g \sim Beta(n_{\gamma_g} + \alpha_g^1, P^2 d - n_{\gamma_g} + \alpha_g^2)$

6: Update σ_j's from $\sigma_j \sim IG(d_1, d_2)$, $j = 1, 2, ..., P$

3.2.2 Fast two-stage computation in a quasi-Bayesian approach

Since the computation of the above fully Bayesian approach is very intensive, one contribution of this manuscript is an alternative two-stage computation approach which still allows straightforward uncertainty quantification of between-trial conditions via a Bayesian hierarchical model and MCMC posterior sampling, but provides a fast approximate procedure

for the estimation of trial-specific VAR parameters. In the first stage, we use Lease square estimation (LSE) to obtain estimated trail-specific VAR parameters $\widehat{\beta_g^{(s)}}$, which satisfy

$$\widehat{\beta_g^{(s)}} = \underset{\beta_g^{(s)} \in \Re^{P^2 d}}{\operatorname{argmin}} \|\mathbf{y}^{(s)} - (I \otimes \mathbb{X}^{(s)})\beta_g^{(s)}\|^2 \tag{3.2.8}$$

In the second stage, we consider the parameters estimated in the first stage, and apply Step 2-6 of the above algorithm at each MCMC iteration to draw posterior samplers of condition-level VAR parameters φ_g and their corresponding binary indicators γ_g.

Algorithm 4 Modified MCMC Algorithm

1: **procedure** LSE
2: Estimate $\beta_g^{(s)}$ with LSE method
3: **procedure** MCMC
4: Jointly update (φ_g, γ_g) using a joint Metropolis-Hastings step
5: Update c_g^1 from $c_g^1 \sim IG(\chi_g^1, \psi_g^1)$, this is a Gibbs step
6: Update c_g^0 from $c_g^0 \sim IG(\chi_g^0, \psi_g^0)$, this is a Gibbs step
7: Update p_g from $p_g \sim Beta(n_{\gamma_g} + \alpha_g^1, P^2 d - n_{\gamma_g} + \alpha_g^2)$
8: Update σ_j's from $\sigma_j \sim IG(d_1, d_2)$, $j = 1, 2, ..., P$

This computation and approximation avoids sampling $\beta_g^{(s)}$ from high dimensional multivariate normal distribution (for example, dimension is $P \times d^2 \times n$ in this case) and computing their high dimensional covariance matrix. As a result, it can save the computation of sampling $P \times d^2 \times n$ parameters at each iteration. The cons of this approach is that the uncertainty of trial-specific parameters in Step 1 is not properly assessed. However, we will show that the estimation results of condition-level parameters are almost not affected in a simulation study in Section 3.3.

3.2.3 Inference on condition-level non-zero VAR parameters

In the Bayesian VAR model (3.2.1), we conclude there exists no connectivity from channel v to channel u at condition g at lag ℓ if $\Phi^{uv}_{\ell,g} = 0$, which is equivalent to $\gamma_{g,k} = 0$, where $\gamma_{g,k}$ is the corresponding binary indicator in "spike-and-slab" priors (3.2.6). Basically this requires dP^2 null hypotheses $H_0^k : \gamma_{g,k} = 0$ to be tested, which leads to a multiple hypotheses testing problem. To conduct inference on this, we adopt a Bayesian decision theoretic perspective, and compute marginal posterior probabilities (MPP) of $p(\gamma_{g,k} = 1|\mathbf{y}^{(s)}, s = 1, ..., n)$. The MPP's are estimated as the proportions of MCMC samples such that $\gamma_{g,k} = 1$ across all iterations after burn-in. A threshold on the MPP's leads to an optimal decision rule under a loss function which is a weighted compounded linear function of false positives and false negatives. We further choose the threshold κ_g to control the Bayesian false discovery rate (BFDR) at a certain level 0.05, that is

$$\text{BFDR}(\kappa_g) = \frac{\sum_{k=1}^{dP^2}(1 - \text{MPP}_k^{(g)})I_{(\text{MPP}_k^{(g)} > \kappa_g)}}{\sum_{k=1}^{dP^2} I_{(\text{MPP}_k^{(g)} > \kappa_g)}} \tag{3.2.9}$$

κ_g^* and κ_g^{**} $(\kappa_g^* < \kappa_g < \kappa_g^{**})$ are selected to ensure interval $\big(\text{BFDR}(\kappa_g^{**}), \text{BFDR}(\kappa_g^*)\big)$ contains $\text{BFDR}(\kappa_g) = 0.05$. $H_0^k : \gamma_{g,k} = 0$ is rejected if $\text{MPP}_k^{(g)} \geq \kappa_g$. In other words, we can conclude lag-specific directional connectivity between certain channels at condition level if their corresponding MPP is within the threshold κ_g.

3.2.4 Measures of effective connectivity

In this section, we will review several frequency domain connectivity measures typically employed in brain imaging when using the VAR model. We start by recalling that a P-channel brain signal, denoted $\{\mathbf{X}_t = (\mathbf{X}_t^1, ..., \mathbf{X}_t^P)', t = 1, 2, ...\}$, is said weakly stationary if

(a.) $E(\mathbf{X}_t)$ is constant over all time t, and

(b.) the auto-covariance function matrix

$$cov(X_t, X_{t+h}) = \Gamma(h) = \begin{pmatrix} \gamma_{11}(h) & \gamma_{12}(h) & \dots & \gamma_{1P}(h) \\ \gamma_{21}(h) & \gamma_{22}(h) & \dots & \gamma_{2P}(h) \\ \vdots & \vdots & \ddots & \vdots \\ \gamma_{P1}(h) & \gamma_{P2}(h) & \dots & \gamma_{PP}(h) \end{pmatrix}$$

depends only on the lag h, where $\gamma_{uv}(h) = cov(X_t^u, X_{t+h}^v)$ for all pairs of channels $u, v = 1, ..., P$.

If the sequence of auto- and cross-covariance between any pair of channels u and v is absolutely summable, i.e., $\sum_{h=-\infty}^{\infty} |\gamma_{uv}(h)| < \infty$, the spectral density matrix of $\{\mathbf{X}_t\}$ is defined as

$$f(\omega) = \sum_{h=-\infty}^{\infty} \Gamma(h) e^{-2\pi i \omega h}, \quad -1/2 \leq \omega \leq 1/2. \tag{3.2.10}$$

which is a $P \times P$ matrix with diagonal elements $f_{uu}(\omega)$ are the auto-spectra of the channels at frequency ω and the off-diagonal elements $f_{uv}(\omega)$ are the cross-spectra of channels u and v at frequency ω.

Then coherence between the u-th and v-th channels at frequency ω, is defined as

$$\rho_{uv}^2(\omega) = \frac{|f_{uv}(\omega)|^2}{f_{uu}(\omega) f_{vv}(\omega)}. \tag{3.2.11}$$

which can be interpreted as how much of ω-oscillatory component in common shared by channel u and channel v. A large coherence value between channels u and v could be due to direct connectivity between these two channels or could be indirectly due to the intervening effect of other channel(s). To measure the strength of connectivity between a pair of channels controlling for the effect of all other channels, we shall use partial coherence.

Define $g(\omega) = f^{-1}(\omega)$ and $g_{pp}(\omega)$ are the diagonal elements of $g(\omega)$. Let $h(\omega)$ be a diagonal matrix whose elements are $g_{pp}^{-1/2}(\omega)$, and $C(\omega) = -g(\omega)h(\omega)g(\omega)$. Then, the partial coherence between the u-th and v-th channels is the modulus squared of the (u, v)-th element of $C(\omega)$ ([12], [11])

$$\zeta_{uv}^2(\omega) = |C_{uv}(\omega)|^2 \tag{3.2.12}$$

Here we consider partial directed coherence instead [4, 5]. For a BH-VAR(d) model given by Equation (3.2.1), define

$$A_g(\omega) = I - \sum_{\ell=1}^{d} \Phi_{\ell,g} \exp(-i2\pi\omega\ell/\Omega) \tag{3.2.13}$$

to be the transform of sequence $\{\Phi_{\ell,g}\}_{\ell=1}^{d}$ at frequency ω, where Ω is the sampling frequency. The partial directed coherence from channel v to channel u at frequency ω under condition g is defined as

$$\pi_{uv}^2(\omega) = \frac{|A_g^{uv}(\omega)|^2}{\sum_{m=1}^{P} |A_g^{mv}(\omega)|^2} \tag{3.2.14}$$

which measures the direct influence from channel v to channel u conditional on all the outflow from channel v. PDC gives an indication on the extent to which present frequency-specific oscillatory activity from a sender channel explains future oscillatory activity in a specific receiver channel relative to all channels in the network.

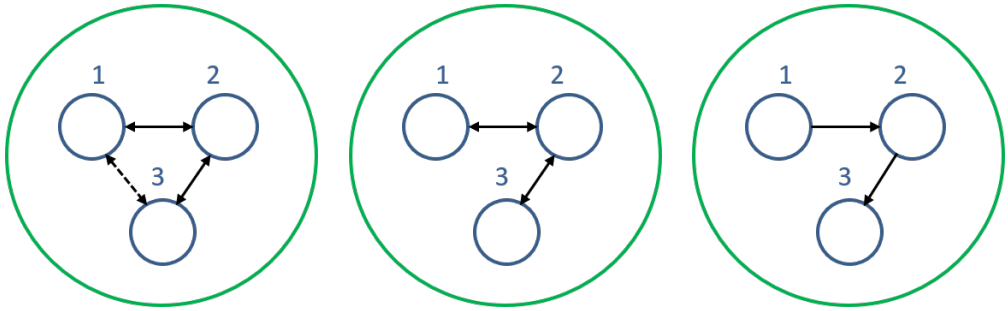

(a) Coherence (b) Partial coherence (c) PDC

Figure 3.3: Example of connectivity characterized by three different measures. Originally information flows from channel 1 to channel 2 and from channel 2 to channel 3 in (c). Indirect connectivity between channel 1 and channel 3 is measured by coherence in (a), while no directionality is specified by partial coherence in (b).

Figure 3.3 demonstrate an example of three brain channels connected in a network and the three different measures. Channel 1 is connected to channel 2 with outflow from 1 to 2; channel 2 is connected to channel 3 with outflow from 2 to 3; channel 1 and 3 are not directly connected. Their connectivity measured by coherence, partial coherence and partial directed coherence are shown in Table 3.1. Coherence between channel 1 and 3 at frequency ω is not zero even though they are not directly connected. Partial coherence between channel 1 and 3 at frequency ω removes the intervention of channel 2, thus $\zeta^2_{31}(\omega) = \zeta^2_{13}(\omega) = 0$. Partial directed coherence between channels only measures direct connectivity and is direction sensitive, consequently $\pi^2_{12}(\omega) = 0$ and $\pi^2_{21}(\omega) \neq 0$.

Channels	Connectivity measures		
	Coherence	Partial coherence	Partial directed coherence
1 and 2	$\rho^2_{12}(\omega) = \rho^2_{21}(\omega) \neq 0$	$\zeta^2_{12}(\omega) = \zeta^2_{21}(\omega) \neq 0$	$\pi^2_{12}(\omega) = 0$
			$\pi^2_{21}(\omega) \neq 0$
2 and 3	$\rho^2_{23}(\omega) = \rho^2_{32}(\omega) \neq 0$	$\zeta^2_{23}(\omega) = \zeta^2_{32}(\omega) \neq 0$	$\pi^2_{23}(\omega) = 0$
			$\pi^2_{32}(\omega) \neq 0$
3 and 1	$\rho^2_{31}(\omega) = \rho^2_{13}(\omega) \neq 0$	$\zeta^2_{31}(\omega) = \zeta^2_{13}(\omega) = 0$	$\pi^2_{31}(\omega) = 0$
			$\pi^2_{13}(\omega) = 0$

Table 3.1: Comparison of three connectivity measures in Figure 3.3.

3.2.5 Model selection

In the previous two-stage approach, VAR models with optimal lag order selected by AIC were fitted for each epoch separately. Therefore the selected lag orders were not the same across epochs. For this Bayesian approach, we fit model (3.2.1) with lag order $d \in \{1, 2, 3\}$ to all epochs separately, then use the posterior mean of MCMC samples after burn-in to calculate BIC for each model. The optimal lag order $\widehat{d}$ is chosen to return the lowest BIC.

3.3 Simulation study

A simulation study was conducted to investigate: (1) whether BH-VAR method can recover the connectivity information of multi-trial brain signals from different experimental conditions; and (2) whether the two-stage computation approach is able to recover the same connectivity inference as the full Bayesian method. In terms of assessing connectivity recovery, the first criterion is sensitivity - how well the estimated results identify the zero and non-zero structure of VAR matrices, which can be evaluated by the MPP results. The second criterion is specificity - how close the method can estimate the partial directed coherence compared to the truth, which is the comparison between the posterior mean PDCs and true PDCs.

3.3.1 Simulation setting

In order to assess the operation characteristic of the proposed procedure, we generated $n = 50$ trials of $P = 12$ channels from $G = 2$ conditions (25 trials for each) using VAR(1) models. The location of zero and non-zero entries of the two condition-level VAR matrices was determined by a $Bern(0.4)$ prior. Furthermore, we generated values of non-zero entries

from $Unif(-0.2, 0.3)$, and random numbers from $Unif(0.3, 0.5)$ were added to the diagonal entries. Figure 3.4 demonstrates the true VAR matrices from two conditions, where the blank cells indicate true zeros. Then random matrices with eigenvalues between $(-0.2, 0.2)$ were added to the condition-level matrices to construct 50 trail-specific VAR matrices. The prior choice was informed by previous exploratory analyses of LFP datasets according to the two-stage procedure in Chapter 2. Finally, we added a random noise from $N(0, 1)$ to each trial and 50 trials were simulated with $T = 1000$ from those VAR(1) matrices. Selected trails from two conditions can be found in Figure 3.5 and Figure 3.6, where different temporal patterns are observed between-conditions.

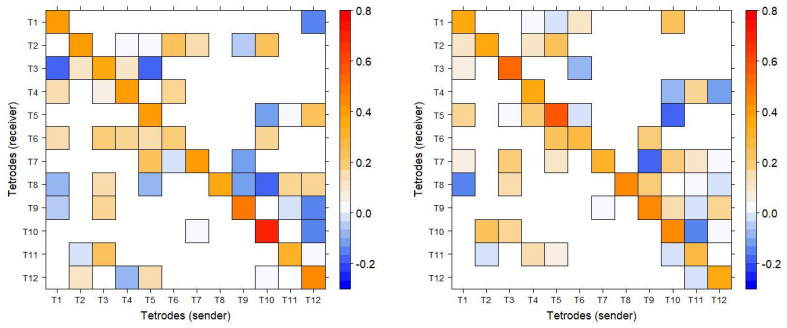

(a) True condition 1 (b) True condition 2

Figure 3.4: Condition-level VAR matrices.

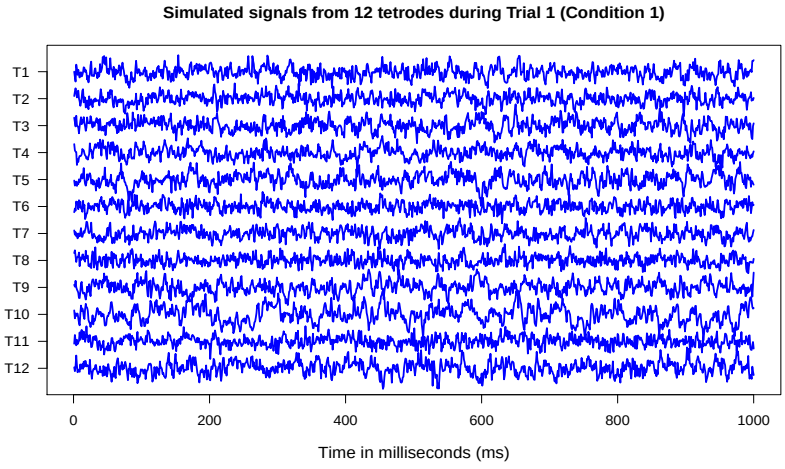

Figure 3.5: Simulated signals from condition 1.

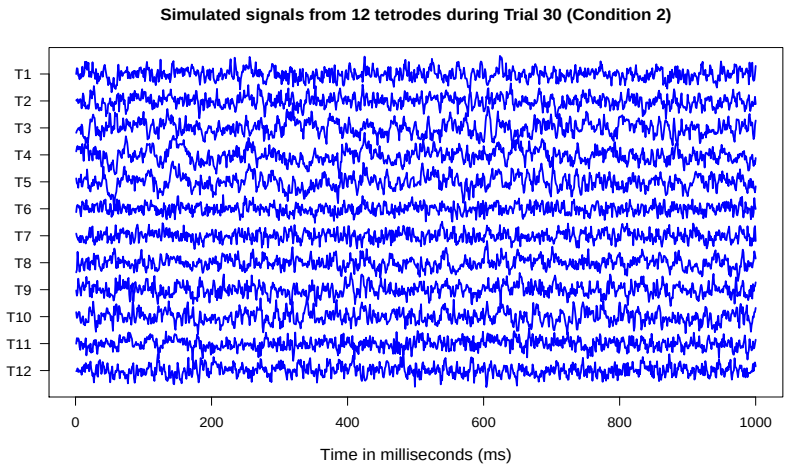

Figure 3.6: Simulated signals from condition 2.

The simulated trials were then estimated by full Bayesian method and two-stage approach separately: 10,000 MCMC iterations were run for both approaches with 5,000 burn-in. Consequently the posterior distributions of condition-level VAR parameters were formed by the 5,000 MCMC samples.

3.3.2 Inference on sparsity connectivity structures

To investigate whether our methods recover the sparse connectivity structure of the simulated data, we examined the inference on the latent indicators $\gamma_{g,k}$ (Figure 3.7). The subindex k indicates the VAR parameter arranged by column. For example, $\gamma_{1,20}$ corresponds to the $(8, 2)$ entry of $\Phi_{1,1}$. The threshold was then determined by Equation (3.2.9), and MPP exceeding the threshold implies that $\gamma_{g,k}$ should be non-zero (positive) while MPP within the threshold implies $\gamma_{g,k}$ is zero (negative). The black dots indicate true positives, red dots indicate false negatives, and blue dots indicate false positives. Based on the results, the full single-stage Bayesian approach successfully recovered most of the true non-zero connectivity, with few false negatives, whose true values were actually very close to 0. It makes sense even though there were a few false positives in the results, because of the randomness that we

added to the trail-specific VAR parameters and the white noise in the simulation setting. Compared to the inference of full Bayesian method, the two-stage approach tends to return lower MPP's values. This trend is possibly due to the loss of information and lack of borrowing of strength in the two-step estimation process versus the full Bayesian method. However, the BFDR thresholding identified a similar sparse connectivity structure than the one recovered by the fully single-stage Bayesian approach.

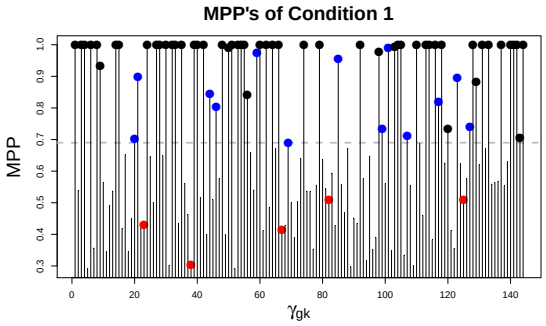

(a) MPP of condition 1 by full Bayesian

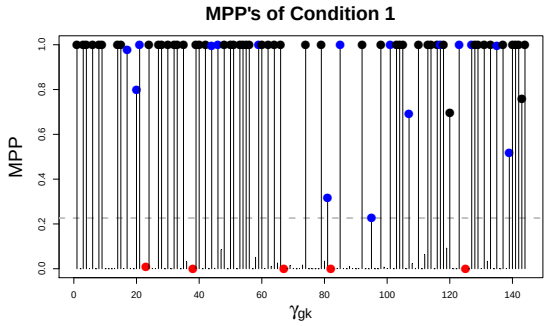

(b) MPP of condition 1 by fast two-stage

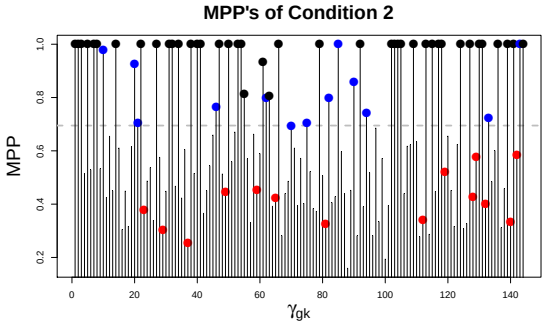

(c) MPP of condition 2 by full Bayesian

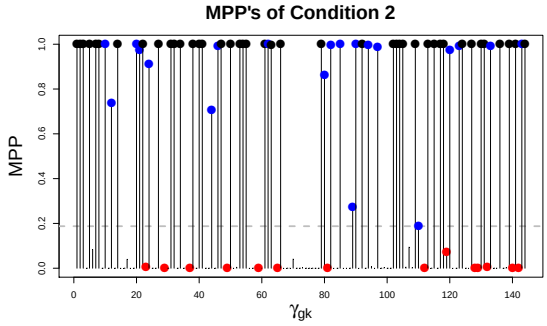

(d) MPP of condition 2 by fast two-stage

Figure 3.7: MPP's by full Bayesian method and two-stage approach. MPP exceeding the threshold implies $\gamma_{g,k}$ should be non-zero (positive) while MPP within the threshold implies $\gamma_{g,k}$ is zero (negative). The black dots indicate true positives, red dots indicate false negatives, and blue dots indicate false positives.

As for the specificity of condition-level connectivities, Figure 3.8 shows the comparison between the truth and posterior mean estimate of $\Phi_{1,1}$ and $\Phi_{1,2}$ given by different methods, where non-zero posterior mean estimate was forced to zero if the corresponding MPP was

smaller than the threshold. The results imply that the estimate obtained by the full single stage Bayesian method is very close to the truth, and the two-stage approach provided similar estimation.

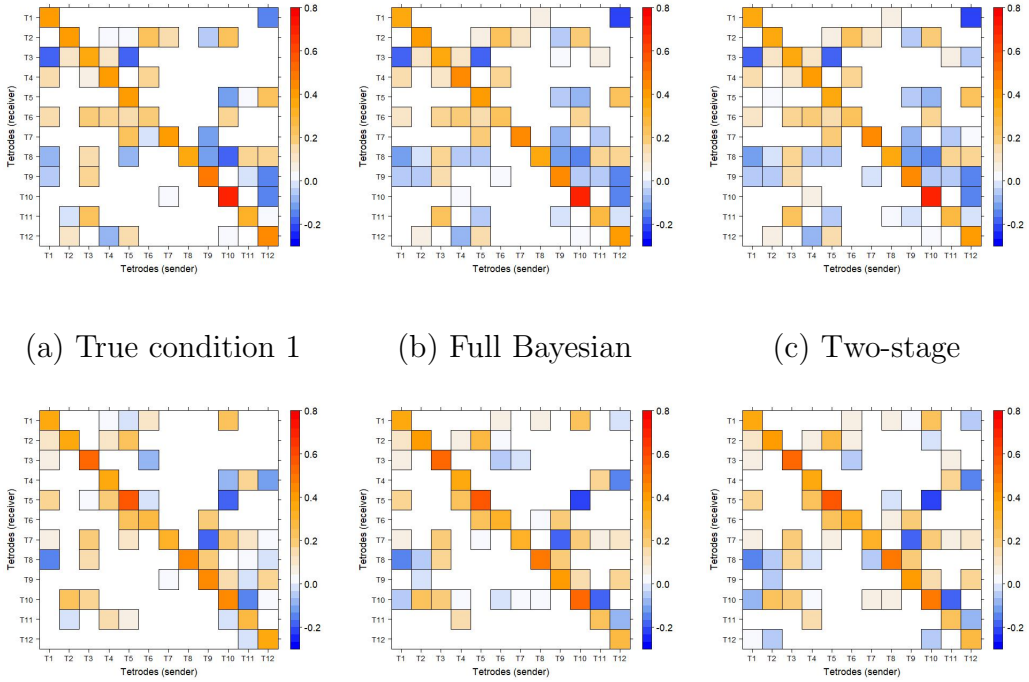

(a) True condition 1 (b) Full Bayesian (c) Two-stage

(d) True condition 2 (e) Full Bayesian (f) Two-stage

Figure 3.8: Posterior mean of estimated condition-level VAR matrices.

In addition to comparing estimated connectivity via VAR coefficients, comparisons on estimated PDCs were conducted to evaluate the specificity of proposed methods to the connectivity strength at frequency domain. Figure 3.9 and Figure 3.10 show the true PDCs and estimated posterior means by two approaches at different condition levels. We can see that both methods recovered the original PDCs.

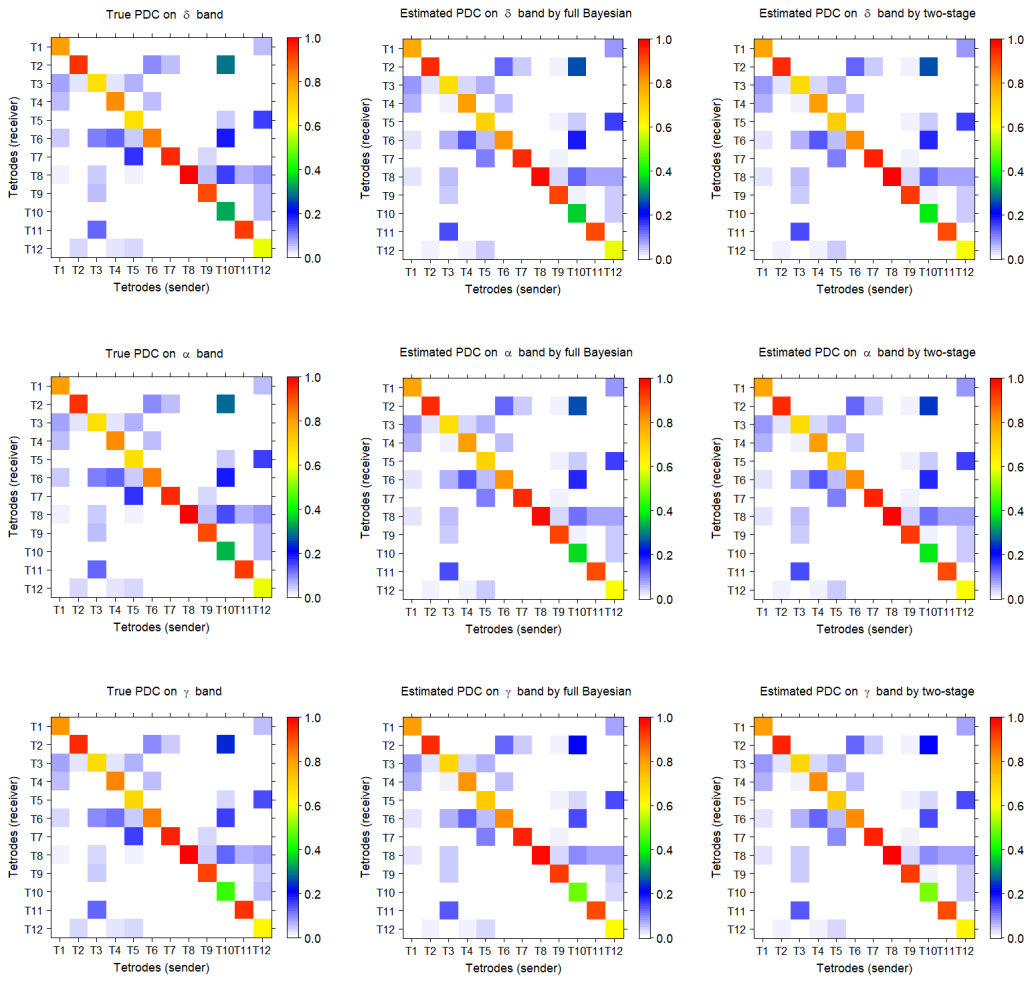

Figure 3.9: Posterior mean of estimated condition-level PDCs at condition 1.

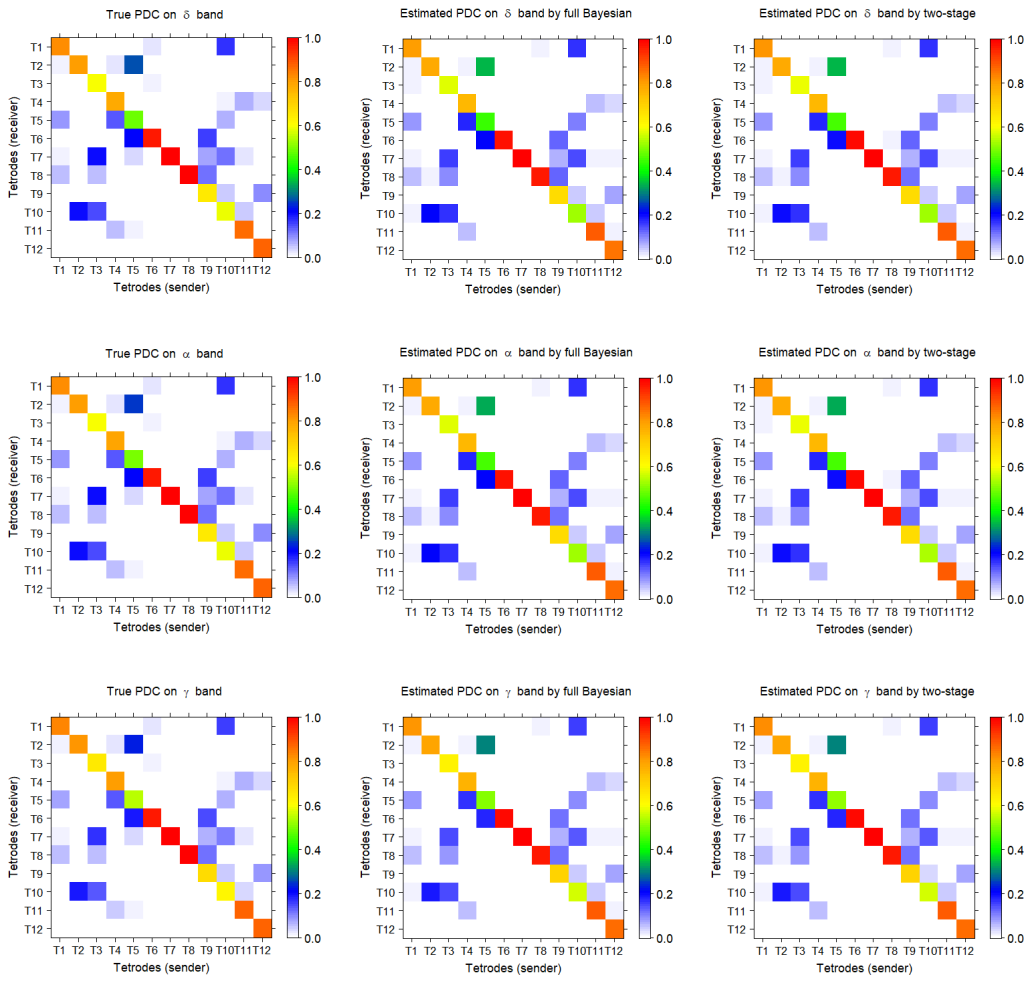

Figure 3.10: Posterior mean of estimated condition-level PDCs at condition 2.

3.4 Application to effective connectivity in multi-trial LFPs

In this section, we fit a BH-VAR model to LFP data recorded from multiple trials under two experimental conditions in a non-spatial sequence memory task [3]. We aim at estimating the VAR parameters at condition level and the partial directed coherence at several frequency bands of interest. Our objective is to examine and quantify potential connectivity (i,.e.,

effective) among electrodes located in hippocampal region CA1. This region is clinically meaningful as this form of sequence memory shows strong behavioral parallels in rats and humans [1], and depends on the hippocampus for both species [13, 8], and is impaired in normal aging [2].

3.4.1 Data analysis

LFPs of Epoch 10 and Epoch 121 can be found in Figure 3.12. We observe that the electrodes can be categorized into 2 main groups based on their LFP waveforms: a lateral CA1 group (T2, T9, T8, and T7) and a medial CA1 group (T14, T23, T16, T22, T19 and T20). Note that, for clarity, the electrodes near the transition point (T15 and T13) are not included in either group. Tetrodes within the same group have highly similar temporal pattern, because tetrodes near each other are likely to behave more similarly than those that are far apart. Note that this division along the mediolateral axis of CA1 is consistent with previous reports of anatomical and functional gradients along the proximodistal extent of CA1 [26, 39].

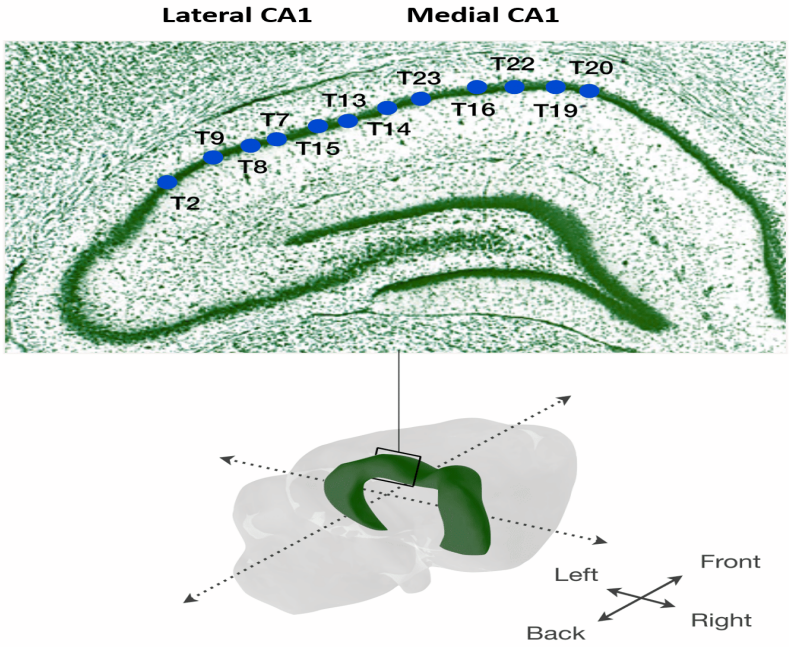

Figure 3.11: Estimated location within the hippocampus (dorsal CA1 region) of the subset of 12 electrodes (tetrodes) included in the analyses.

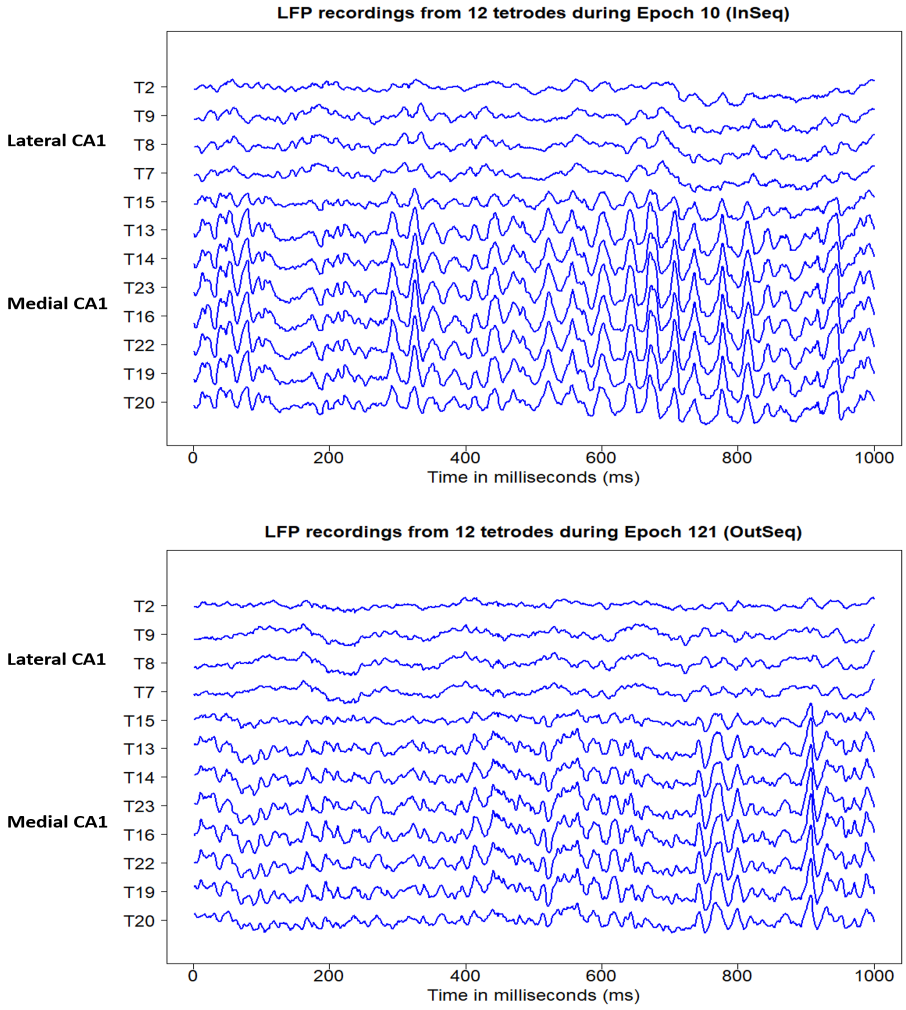

Figure 3.12: LFPs from 12 tetrodes studied in this paper during Epoch 10 and Epoch 121. These LFPs have temporal patterns that can be separated into two main groups: a lateral CA1 group (T2, T9, T8, and T7) and a medial CA1 group (T14, T23, T16, T22, T19 and T20). For clarity, the electrodes near the transition point (T15 and T13) are not included in either group. Note the difference in LFP waveforms between the two trial conditions (e.g., lower beta power on OutSeq trial than InSeq trial).

Preliminary analysis demonstrated that both auto-correlation function (ACF) and partial auto-correlation function (PACF) of original LFPs across all 247 epochs failed to decay to zero even after very long lags, which suggested evidence of non-stationarity (or long-memory). Therefore, it's necessary to pre-process the data by taking a first order difference. Compared to the raw LFPs, the ACF of pre-processed data eventually decayed to zero, looking more

stationary. Consequently a BH-VAR(2) model was fitted to the pre-processed LFP data in this study, with $n_1 = 219$ epochs in condition 1 and $n_2 = 28$ epochs in condition 2. In order to overcome the intensive computation issue, the two-stage approach was employed, where on the first stage LSE was used to estimate the coefficients of VAR(2) for each epoch, then MCMC was applied to these trial-specific estimates on the second stage to obtain the posterior samples of condition-level VAR(2) coefficients and PDCs. The posterior mean of condition-specific VAR(2) coefficients are demonstrated in Figure 3.13.

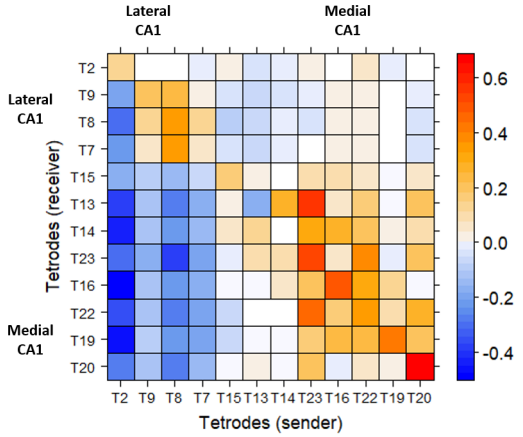

(a) Estimated Φ_1 of "InSeq" condition

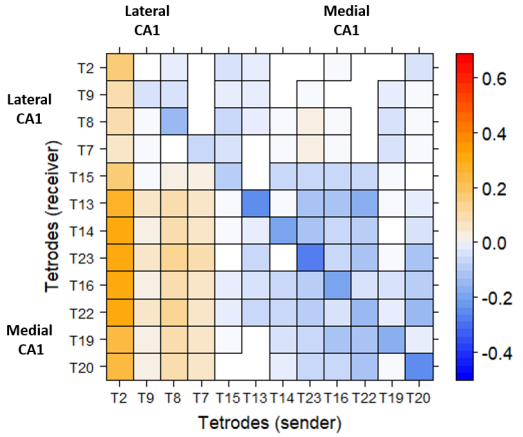

(b) Estimated Φ_2 of "InSeq" condition

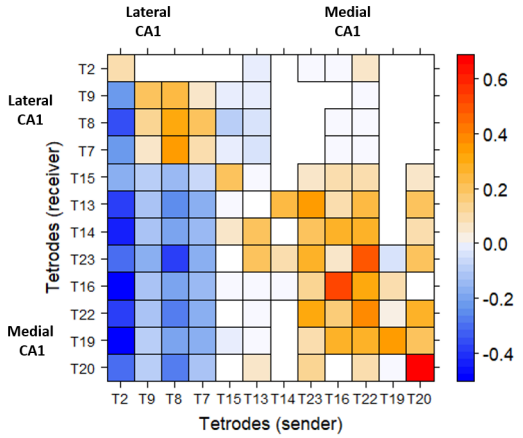

(c) Estimated Φ_1 of "OutSeq" condition

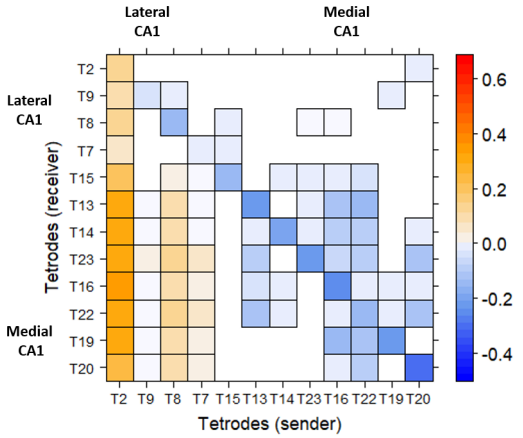

(d) Estimated Φ_2 of "OutSeq" condition

Figure 3.13: (a)-(d) demonstrate the posterior mean of estimated VAR matrices of "InSeq" and "OutSeq" condition. The blank cells indicate estimated zero coefficient.

Estimated Φ_1 and Φ_2 in "InSeq" and "OutSeq" condition look similar in terms of VAR connectivity strength. In the estimated Φ_1, the recorded LFPs generally have positive dependence with the signal from themselves at 1 lag before (diagonal entries). Moreover, the signals from T2, T9, T8 and T7, which belong to the lateral group, have negative lead-effect on the current signals from medial tetrodes (T14, T23, T16, T22, T19 and T20). Different lead-lag pattern are observed in estimated Φ_2. LFPs generally have negative lead-effect on the signal from the same tetrode at 2 lags behind, while the lateral group have positive leading effect on the medial group in the future. In addition, VAR coefficients under "OutSeq" condition tend to have more zero values compared to "InSeq" condition.

Since we are more interested in the LFP connectivity in frequency domain, the condition-level PDCs were computed at each MCMC iteration at the following frequency bands: δ band (0-4 Hertz), θ band (4-8 Hertz), α band (8-12 Hertz) and β band (12-32 Hertz). Consequently we obtain the posterior distribution of PDCs. Figure 3.14 and 3.15 demonstrate the posterior mean of PDC under "InSeq" and "OutSeq" condition respectively. As we can see, the variability of PDCs across different frequency bands is very small, so we use the results of the β band as representative to explain the PDC.

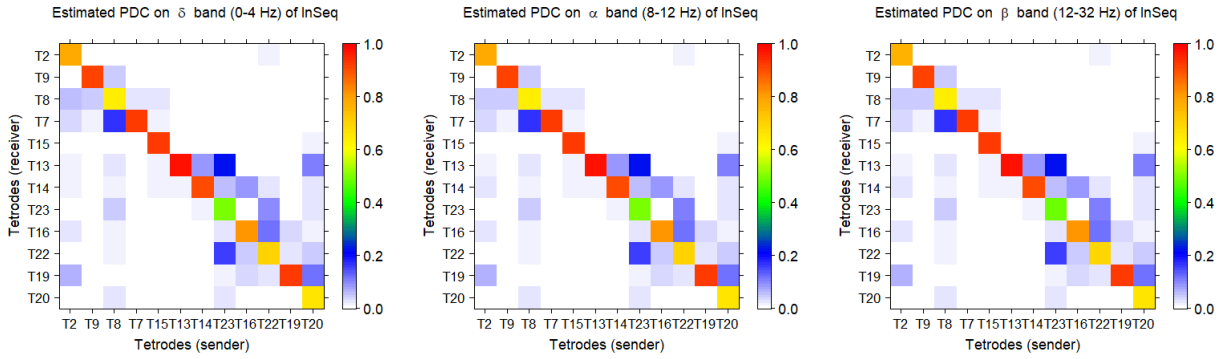

Figure 3.14: Estimated PDC of "InSeq" condition by posterior mean. The variation across different frequency bands is very small.

In "InSeq" condition, tetrodes in the lateral group are functionally connected to each other,

and so are tetrodes in the medial group. Over 80% information of tetrodes T9, T7, T15, T13, T14, T16 and T19 can be explained by their own past while their information flowing to other tetrodes is very close to 0. Tetrodes T2, T8, T23, T22 and T20 have significant amount of information flowing to other tetrodes. Particularly, the proportion of current tetrode T23 that is explained by its own past is only about 47.0%, but information flowing to T22 and T13 is 16.7% and 22.6% respectively. These suggest that T23 was positioned in a region of CA1 (either in terms of the mediolateral axis or depth relative to the cell layer) in which the LFP signature has considerable overlap with the rest of medial CA1. Estimated PDCs from the medial tetrodes (e.g., T14, T23,...,T20) to the lateral tetrodes (T2, T9, T8, T7) are almost zero (the blank on the upper right of PDC matrix), whereas several non-zero values are observed in the lateral-to-medial direction (bottom-left quadrant). This suggests that, at least at the time lags examined (1-3 ms), information flows primarily in a lateral-to-medial direction in CA1 during InSeq trials.

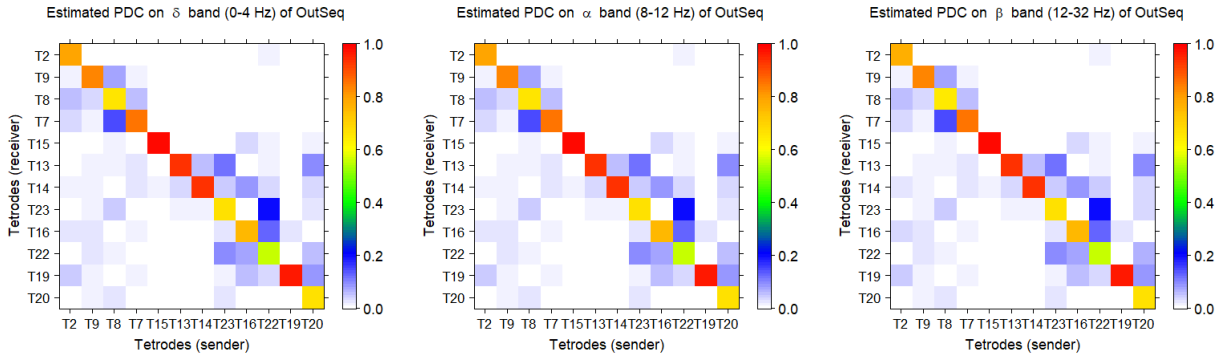

Figure 3.15: Estimated PDC of "OutSeq" condition by posterior mean. The variation across different frequency bands is very small.

As for "OutSeq" condition, over 80% information of tetrodes T9, T7, T15, T13, T14 and T19 can be explained by their own past with little information flowing to other tetrodes. Tetrodes T2, T8, T23, T16, T22 and T20 tend to pass information to other tetrodes as they have large amount of information flowing out. For example, only 54.5% of current tetrode T22 can be explained by its own past, while information flowing to T16 and T23 is 12.9%

and 19.9% respectively. Notice that T2, T8, T23, T22 and T20 also have high information outflow in the "InSeq" condition, indicating that the LFP features they capture are not condition-specific. Similar to what we found in "InSeq" trials, medial-to-lateral estimated PDCs are almost zero (upper right quadrant) whereas lateral-to-medial estimated PDCs include several non-zero values (lower left quadrant). This suggests that information also primarily flows from lateral CA1 to medial CA1 during "OutSeq" trial presentations, though this effect is a bit stronger than on "InSeq" trials.

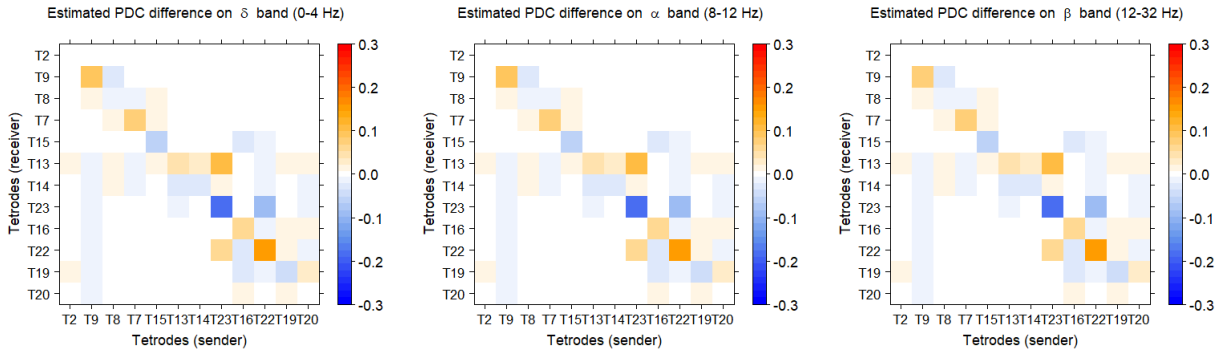

Figure 3.16: Estimated mean PDC difference between "InSeq" and "OutSeq" condition ("InSeq" - "OutSeq"). Significant increase on the auto-PDC of T9, T7 and T22 as well as decrease on the auto-PDC of T15, T23 and T19 are observed. The lower left quadrant indicates that leading effect of the lateral tetrodes on the medial tetrodes is a bit stronger on "OutSeq" trials than "InSeq" trials.

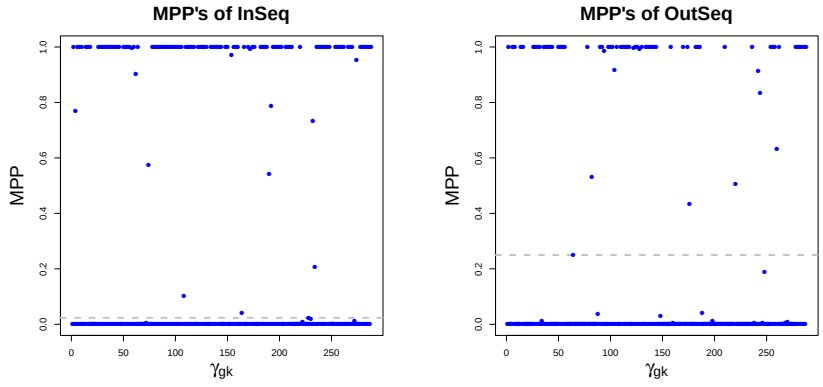

Figure 3.17: MPP's of $\gamma_{g,k}$ at "InSeq" and "OutSeq" condition. The gray dash line indicates threshold corresponding to BFDR=0.05.

3.4.2 Testing the PDC difference between two conditions

To compare the difference between PDCs from "InSeq" and "OutSeq" conditions, we did Bayesian inference on $H_0 : \text{Diff}_{i,j} = 0$ vs $H_a : \text{Diff}_{i,j} \neq 0$, where $\text{Diff}_{i,j} = \text{PDC}_{i,j}^{\text{InSeq}} - \text{PDC}_{i,j}^{\text{OutSeq}}$ is the difference of PDC from j-th channel to i-th channel between two conditions. An estimate of the difference, $\text{Diff}_{i,j}^{(m)}$, can be computed at each MCMC iteration m. Thus, it is possible to obtain the posterior distribution and 95% credible interval of $\text{Diff}_{i,j}$ after burn-in. If the posterior probability of the difference is unimodal and regularly behaved, we can use the 95% credible intervals as a guide for testing, i.e. we reject the null hypothesis H_0 if the 95% credible interval does not include 0 and conclude that the difference of PDC from j-th channel to i-th channel between two conditions is significant during the memory task. A more complete analysis could be conducted in a decision theoretic framework by thresholding the posterior probabilities of the differences being positive or negative, but we did not see any relevant difference between the two approaches in this setting. The posterior mean, 95% credible interval and probability of $\text{Diff}_{i,j} > 0$ are reported in Table 3.2 and Table 3.3.

Tetrode	Posterior mean	95% Credible Interval	$Pr(\text{Diff}_{i,i} > 0)$ (%)
T2	0.002	(-0.041,0.040)	46.2
T9	0.082	(0.045,0.123)	100
T8	-0.010	(-0.045,0.027)	29.3
T7	0.070	(0.033,0.101)	100
T15	-0.054	(-0.067,-0.042)	0
T13	0.040	(0.027,0.054)	100
T14	-0.034	(-0.046,-0.021)	0
T23	-0.187	(-0.218,-0.158)	0
T16	0.063	(0.021,0.107)	99.8
T22	0.151	(0.113,0.190)	100
T19	-0.051	(-0.068,-0.033)	0
T20	-0.004	(-0.049,0.043)	42.6

Table 3.2: Difference of auto-PDCs between "InSeq" and "OutSeq".

Tetrode → Tetrode	Posterior mean	95% Credible Interval	$Pr(\text{Diff}_{i,j} > 0)$ (%)
T2 → T13	0.010	(0.003,0.015)	99.4
T2 → T19	0.008	(-0.015,0.027)	77.5
T9 → T8	0.009	(-0.007,0.023)	86.8
T9 → T16	-0.016	(-0.027,-0.007)	0.1
T9 → T22	-0.016	(-0.027,-0.008)	0
T8 → T9	-0.028	(-0.046,-0.008)	1.1
T8 → T14	0.007	(0.000,0.012)	97.8
T23 → T13	0.102	(0.081,0.123)	100
T23 → T22	0.067	(0.049,0.085)	100
T16 → T19	-0.024	(-0.049,-0.003)	1.5
T22 → T23	-0.089	(-0.121,-0.058)	0
T20 → T15	-0.002	(-0.013,0.007)	35.5

Table 3.3: Difference of some cross-PDCs between "InSeq" and "OutSeq".

Based on the results, we find that there is significant difference in auto-PDCs of tetrode T9, T7, T15, T13, T14, T23, T16, T22 and T19 between two conditions. This suggests that the proportion of current oscillatory activity of these tetrodes that can be explained by their own past activity is influenced by trial conditions (i.e., whether odors were presented InSeq or OutSeq). Interestingly, these tetrodes were primarily located in medial CA1, perhaps indicating this distinction is linked to their stronger high-frequency oscillations. However, the proportion of tetrodes showing stronger modulation to InSeq or OutSeq trials was comparable (4/8 tetrodes in each case) and did not exhibit a clear relationship with tetrode position. In addition, significant differences are detected in some cross-PDCs between "InSeq" and "OutSeq" (e.g., T2 to T13, T23 to T13, T23 to T22), which are evidences that the information flowing from these tetrode locations to others is also influenced by the InSeq/OutSeq condition of the presented odor. Interestingly, the modulation was stronger on InSeq than

OutSeq trials (4/5 tetrodes), primarily involved electrodes in medial CA1 (T22, T19, T23, T14) or the transition zone (T13, T15), and included both directions along the mediolateral axis. Figure 3.18 and Figure 3.19 demonstrate the posterior densities of all auto-PDC differences and some cross-PDC differences, where red line indicates the posterior mean and purple dashed lines indicate the bound of 95% credible interval.

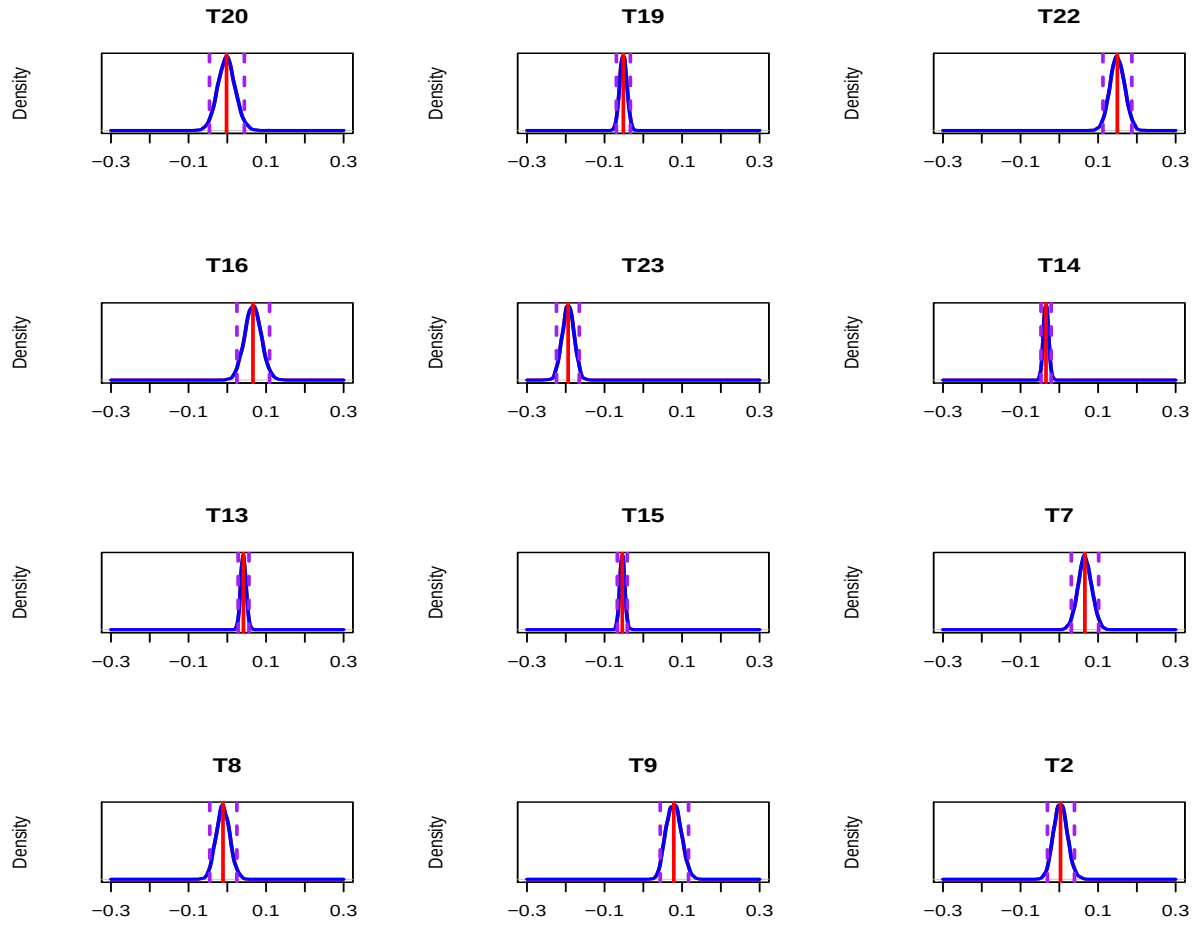

Figure 3.18: Posterior density of auto-PDC differences between "InSeq" and "OutSeq". Red line indicates the posterior mean, while purple dashed lines indicate the bound of 95% credible interval. The gray dashed line is the reference at 0.

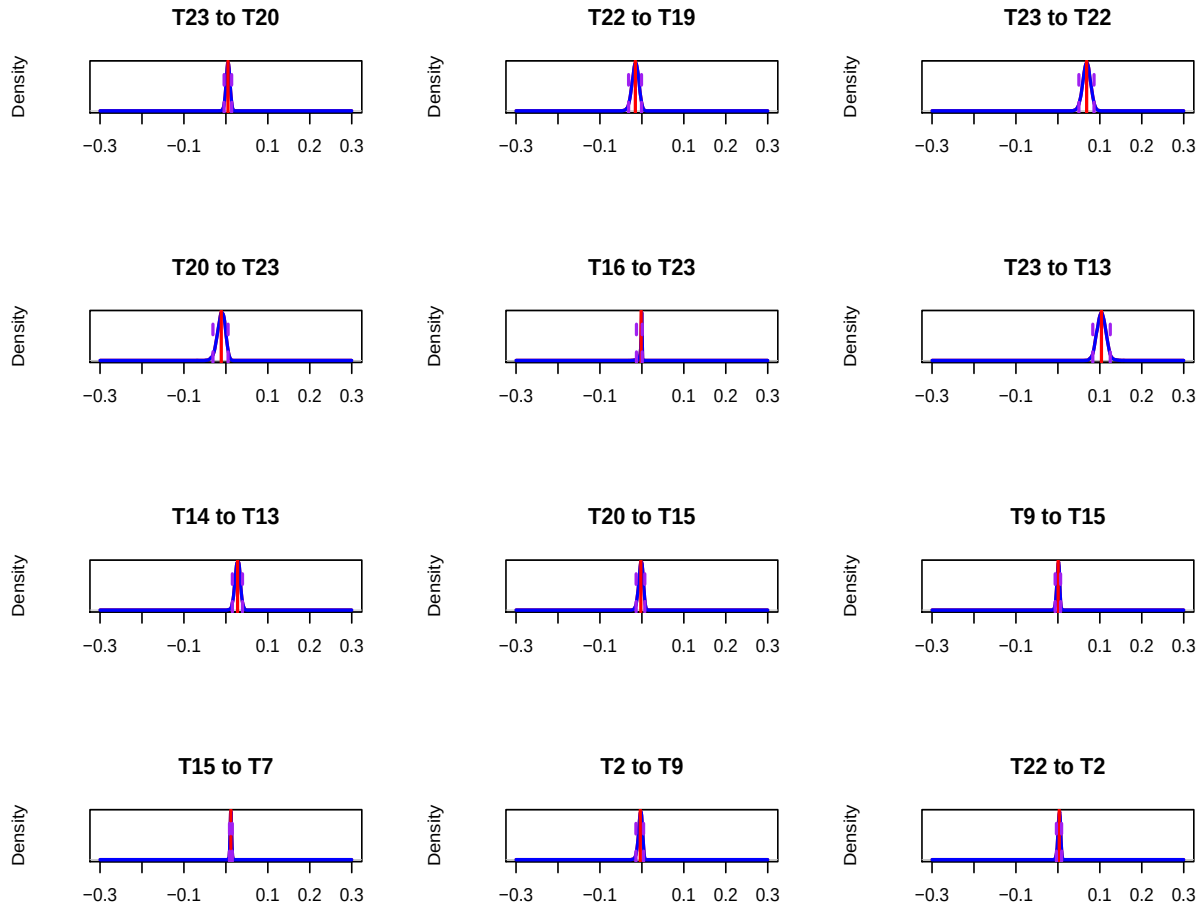

Figure 3.19: Posterior density of some cross-PDC differences between "InSeq" and "OutSeq". Red line indicates the posterior mean, while purple dashed lines indicate the bound of 95% credible interval. The gray dashed line is the reference at 0.

3.5 Conclusion

We extended traditional Bayesian hierarchical vector autoregressive models in this chapter and applied it to LFP data. This framework incorporates within-conditions correlation with between-conditions variation without introducing any additional uncertainty, which overcomes the deficiency of commonly used two-stage approach. In addition, we successfully characterized both trial- and condition-level hippocampal connectivity simultaneously with

this approach and made natural inference on the difference of condition-level connectivity across experimental conditions via MCMC samplers. Partial directed coherence was adopted to measure the directional connectivity between the channels at condition level. It gives an indication on the extent to which present frequency-specific oscillatory activity from a sender channel explains future oscillatory activity in a specific receiver channel relative to all channels in the hippocampal region. The proposed modeling approach provided novel insights into potential evolution of hippocampal connectivity during performance of a complex sequence memory task. Specifically, these results allowed us to separate CA1 into two functional units, a lateral and a medial segment, each showing stronger functional connectivity to itself than to the other. This approach also revealed that information primarily flowed in a lateral-to-medial direction across trials (within-condition), and suggested this effect was stronger on OutSeq than InSeq trials (between-conditions effect). Collectively, these results indicate that the proposed model is a promising approach to quantify the evolution of functional connectivity, both within- and between-conditions, and thus should have broad applications in neuroscience research

Chapter 4

Conclusion

4.1 Summary

Hippocampal connectivity in single-trial LFPs was characterized by vector autoregressive models in Chapter 2. The proposed hybrid LASSLE (LASSO+LSE) method takes advantage of both regularization (to control for sparsity) and least squares estimation (to improve bias and mean-squared error). This novel estimating method successfully (1.) identified the connectivity structure between channels in the hippocampus and (2.) quantified both the strength and directionality of connectivity between these channels. Partial directed coherence, a frequency-specific measure, was employed to measure the effective hippocampal connectivity. It explains the extent to which the present oscillatory activity in a sender hippocampal channel influences the future oscillatory activity in a specific receiver hippocampal channel relative to all possible receivers in the network. In addition, bootstrap-based inference approach was developed to obtain the variation of estimated trial-specific connectivity.

In Chapter 3, I further developed the modeling approach for single trial LFPs and extended it to Bayesian hierarchical vector autoregressive models for multi-trial LFPs. The adjusted

Bayesian framework allows us to incorporate within-conditions connectivity similarity with between-conditions connectivity heterogeneity in modeling as well as provide a natural way to conduct trial- and condition-level inference on effective connectivity simultaneously. This proposed approach provided insights into the alteration of hippocampal connectivity across different experimental conditions.

4.2 Limitations and future work

There are still some limitations with this study. First of all, like all other parametric approaches the robustness of fitted VAR models concerns us. Further simulation study should be conducted when the true model is not VAR(d) but something else, like state-space models or mixture of autoregressive models. Given that PDC is a measure of effective connectivity specifically for vector autoregressive models, it is not valid to test the robustness here. Therefore other model-free connectivity measures (e.g., coherence) should be involved to measure the connectivity characterized by different models and make the performance comparison. We will gain more confidence to apply VAR models in the future study of brain signals if its robustness is confirmed in the simulation.

Another limitation is how to guarantee the stationarity of estimated VAR parameters to satisfy the VAR model assumption. A VAR(d) model is stationary if

$$det(I - \Phi_1 z - \Phi_2 z^2 - ... - \Phi_d z^d) \neq 0, \quad for |z| \leq 1 \tag{4.2.1}$$

where $\{\Phi_\ell\}_{\ell=1}^d$ are VAR coefficient matrices in Equation (1.2.1) [32]. This result gives theoretical constraints on the parameters, however, it is not easy to implement for the estimates in practice. A "single-unit-root" prior was suggested in [47] to ensure there is either at least one explosive common unit root in the system or the VAR model is stationary [35].

One future direction could be further developing this prior and applying it to ensure the stationarity of BH-VAR model.

Lastly, the computation of full Bayesian approach in the study of multi-trial LFPs is very heavy at this point: 16 hours for $n = 50$ trials with $P = 12$ channels. Most of the computation burden comes from the realization of "spike-and-slab" priors. A possible solution to this could be Variational Bayesian methods which use variational posteriors to approximate the true posterior distribution analytically [38, 7, 52].

Bibliography

[1] T. A. Allen, A. M. Morris, A. T. Mattfeld, C. E. Stark, and N. J. Fortin. A sequence of events model of episodic memory shows parallels in rats and humans. *Hippocampus*, 24(10):1178–1188, 2014.

[2] T. A. Allen, A. M. Morris, S. M. Stark, N. J. Fortin, and C. E. Stark. Memory for sequences of events impaired in typical aging. *Learning & Memory*, 22(3):138–148, 2015.

[3] T. A. Allen, D. M. Salz, S. McKenzie, and N. J. Fortin. Nonspatial sequence coding in ca1 neurons. *Journal of Neuroscience*, 36(5):1547–1563, 2016.

[4] L. A. Baccalá and K. Sameshima. Partial directed coherence: a new concept in neural structure determination. *Biological cybernetics*, 84(6):463–474, 2001.

[5] L. A. Baccalá and K. Sameshima. Partial directed coherence. *Methods in Brain Connectivity Inference through Multivariate Time Series Analysis*, pages 57–73, 2014.

[6] C. A. Barnes. Memory deficits associated with senescence: a neurophysiological and behavioral study in the rat. *Journal of comparative and physiological psychology*, 93(1):74, 1979.

[7] M. J. Beal. Variational algorithms for approximate bayesian inference. 2003.

[8] V. K. Boucquey, T. A. Allen, D. J. Huffman, N. J. Fortin, and C. E. Stark. A cross-species sequence memory task reveals hippocampal and medial prefrontal cortex activity and interactions in humans. *Hippocampus*, 2015, submitted.

[9] S. Chiang, M. Guindani, H. J. Yeh, Z. Haneef, J. M. Stern, and M. Vannucci. Bayesian vector autoregressive model for multi-subject effective connectivity inference using multi-modal neuroimaging data. *Human brain mapping*, 38(3):1311–1332, 2017.

[10] G. Deshpande, S. LaConte, G. A. James, S. Peltier, and X. Hu. Multivariate granger causality analysis of fmri data. *Human brain mapping*, 30(4):1361–1373, 2009.

[11] M. Fiecas and H. Ombao. The generalized shrinkage estimator for the analysis of functional connectivity of brain signals. *The Annals of Applied Statistics*, pages 1102–1125, 2011.

[12] M. Fiecas, H. Ombao, C. Linkletter, W. Thompson, and J. Sanes. Functional connectivity: Shrinkage estimation and randomization test. *NeuroImage*, 49(4):3005–3014, 2010.

[13] N. Fortin, J. Asem, C. Ng, C. Quirk, T. Allen, and G. Elias. Distinct contributions of hippocampal, prefrontal, perirhinal and nucleus reuniens regions to the memory for sequences of events. *Society for Neuroscience Abstracts (San Diego, CA)*, 2016.

[14] J. Friedman, T. Hastie, and R. Tibshirani. Regularization paths for generalized linear models via coordinate descent. *Journal of statistical software*, 33(1):1, 2010.

[15] K. J. Friston. Functional and effective connectivity in neuroimaging: a synthesis. *Human brain mapping*, 2(1-2):56–78, 1994.

[16] W. J. Fu. Penalized regressions: the bridge versus the lasso. *Journal of computational and graphical statistics*, 7(3):397–416, 1998.

[17] E. I. George and R. E. McCulloch. Variable selection via gibbs sampling. *Journal of the American Statistical Association*, 88(423):881–889, 1993.

[18] E. I. George and R. E. McCulloch. Approaches for bayesian variable selection. *Statistica sinica*, pages 339–373, 1997.

[19] C. Gorrostieta, M. Fiecas, H. Ombao, E. Burke, and S. Cramer. Hierarchical vector auto-regressive models and their applications to multi-subject effective connectivity. *Frontiers in computational neuroscience*, 7:159, 2013.

[20] C. Gorrostieta, H. Ombao, P. Bédard, and J. N. Sanes. Investigating brain connectivity using mixed effects vector autoregressive models. *NeuroImage*, 59(4):3347–3355, 2012.

[21] C. W. Granger. Investigating causal relations by econometric models and cross-spectral methods. *Econometrica: Journal of the Econometric Society*, pages 424–438, 1969.

[22] F. Han, H. Lu, and H. Liu. A direct estimation of high dimensional stationary vector autoregressions. *The Journal of Machine Learning Research*, 16(1):3115–3150, 2015.

[23] T. Hesterberg, N. H. Choi, L. Meier, C. Fraley, et al. Least angle and l1 penalized regression: A review. *Statistics Surveys*, 2:61–93, 2008.

[24] B. Horwitz. The elusive concept of brain connectivity. *Neuroimage*, 19(2):466–470, 2003.

[25] L. Hu, N. J. Fortin, and H. Ombao. Modeling high-dimensional multichannel brain signals. *Statistics in Biosciences*, pages 1–36, 2017.

[26] K. M. Igarashi, H. T. Ito, E. I. Moser, and M.-B. Moser. Functional diversity along the transverse axis of hippocampal area ca1. *FEBS letters*, 588(15):2470–2476, 2014.

[27] V. Ivanov, L. Kilian, et al. A practitioners guide to lag order selection for var impulse response analysis. *Studies in Nonlinear Dynamics and Econometrics*, 9(1):1–34, 2005.

[28] M. Kamiński, M. Ding, W. A. Truccolo, and S. L. Bressler. Evaluating causal relations in neural systems: Granger causality, directed transfer function and statistical assessment of significance. *Biological cybernetics*, 85(2):145–157, 2001.

[29] C. Kirch. Resampling in the frequency domain of time series to determine critical values for change-point tests. *Statistics & Decisions*, 25(3/2007):237–261, 2007.

[30] A. Kolmogorov. Sulla determinazione empirica delle leggi di probabilita. *Giorn. Ist. Ital. Attuari*, 4:1–11, 1933.

[31] J.-P. Kreiss. Bootstrap procedures for ar (co)-processes. In *Bootstrapping and related techniques: proceedings of an international conference held in Trier, FRG, June 4-8, 1990*, volume 376, page 107. Springer-Verlag, 1992.

[32] H. Liitkepohl. Introduction to multiple time series analysis. *Berlin et al*, 1991.

[33] H. Liu, B. Yu, et al. Asymptotic properties of lasso+ mls and lasso+ ridge in sparse high-dimensional linear regression. *Electronic Journal of Statistics*, 7:3124–3169, 2013.

[34] J. Mairal and B. Yu. Complexity analysis of the lasso regularization path. *arXiv preprint arXiv:1205.0079*, 2012.

[35] S. Miranda-Agrippino and G. Ricco. Bayesian vector autoregressions. 2018.

[36] T. J. Mitchell and J. J. Beauchamp. Bayesian variable selection in linear regression. *Journal of the American Statistical Association*, 83(404):1023–1032, 1988.

[37] M.-B. Moser and E. I. Moser. Functional differentiation in the hippocampus. *Hippocampus*, 8(6):608–619, 1998.

[38] N. M. Nasrabadi. Pattern recognition and machine learning. *Journal of electronic imaging*, 16(4):049901, 2007.

[39] C.-W. Ng, G. A. Elias, J. S. Asem, T. A. Allen, and N. J. Fortin. Nonspatial sequence coding varies along the ca1 transverse axis. *Behavioural brain research*, 2017.

[40] J. O'Keefe. Hippocampus, theta, and spatial memory. *Current opinion in neurobiology*, 3(6):917–924, 1993.

[41] H. Ombao and S. Van Bellegem. Evolutionary coherence of nonstationary signals. *IEEE Transactions on Signal Processing*, 56(6):2259–2266, 2008.

[42] E. Paparoditis. Frequency domain bootstrap for time series. In *Empirical process techniques for dependent data*, pages 365–381. Springer, 2002.

[43] D. N. Politis et al. The impact of bootstrap methods on time series analysis. *Statistical Science*, 18(2):219–230, 2003.

[44] M. Rubinov and O. Sporns. Complex network measures of brain connectivity: uses and interpretations. *Neuroimage*, 52(3):1059–1069, 2010.

[45] X. Shao. The dependent wild bootstrap. *Journal of the American Statistical Association*, 105(489):218–235, 2010.

[46] R. H. Shumway and D. S. Stoffer. Time series analysis and its applications. *Studies In Informatics And Control*, 9(4):375–376, 2000.

[47] C. A. Sims. A nine-variable probabilistic macroeconomic forecasting model. In *Business Cycles, Indicators and Forecasting*, pages 179–212. University of Chicago Press, 1993.

[48] O. Sporns, D. R. Chialvo, M. Kaiser, and C. C. Hilgetag. Organization, development and function of complex brain networks. *Trends in cognitive sciences*, 8(9):418–425, 2004.

[49] C. J. Stam and J. C. Reijneveld. Graph theoretical analysis of complex networks in the brain. *Nonlinear biomedical physics*, 1(1):3, 2007.

[50] R. Tibshirani. Regression shrinkage and selection via the lasso. *Journal of the Royal Statistical Society. Series B (Methodological)*, pages 267–288, 1996.

[51] A. B. Tort, M. A. Kramer, C. Thorn, D. J. Gibson, Y. Kubota, A. M. Graybiel, and N. J. Kopell. Dynamic cross-frequency couplings of local field potential oscillations in rat striatum and hippocampus during performance of a t-maze task. *Proceedings of the National Academy of Sciences*, 105(51):20517–20522, 2008.

[52] M. J. Wainwright, M. I. Jordan, et al. Graphical models, exponential families, and variational inference. *Foundations and Trends® in Machine Learning*, 1(1–2):1–305, 2008.

[53] N. Wiener. The theory of prediction. *Modern mathematics for engineers*, 1956.

[54] P. Zhao, G. Rocha, and B. Yu. The composite absolute penalties family for grouped and hierarchical variable selection. *The Annals of Statistics*, pages 3468–3497, 2009.

[55] P. Zhao and B. Yu. On model selection consistency of lasso. *Journal of Machine learning research*, 7(Nov):2541–2563, 2006.

Appendix A

MCMC Algorithm

1. Update $\beta_g^{(s)}$ for all s such that $\eta_s = g$ from $\beta_g^{(s)} \sim N(\mu_\beta^{(s)}, v_\beta^{(s)})$, with
   $\mu_\beta^{(s)} = [\Sigma^{-1} \otimes (\mathbb{X}'^{(s)}\mathbb{X}^{(s)}) + \Xi_g^{-1}]^{-1}[(\Sigma^{-1} \otimes \mathbb{X}'^{(s)})\mathbf{y}^{(s)} + \Xi_g^{-1}\varphi_g]$,
   $v_\beta^{(s)} = [\Sigma^{-1} \otimes (\mathbb{X}'^{(s)}\mathbb{X}^{(s)}) + \Xi_g^{-1}]^{-1}$

2. Jointly update (γ_g, φ_g) using a joint Metropolis-Hastings step
   $min\{1, \frac{p(\gamma_g^*, \varphi_g^* | \{\beta_g^{(s)}\}_{s:\eta_s=g}, \Xi_g)}{p(\gamma_g, \varphi_g | \{\beta_g^{(s)}\}_{s:\eta_s=g}, \Xi_g)}\} = min\{1, \frac{\prod_{s:\eta_s=g} p(\beta_g^{(s)} | \varphi_g^*, \Xi_g) \left[\prod_{k=1}^{dP^2} p(\varphi_{g,k}^* | \gamma_{g,k}^*)\right] \left[\prod_{k=1}^{dP^2} p(\gamma_{g,k}^*)\right]}{\prod_{s:\eta_s=g} p(\beta_g^{(s)} | \varphi_g, \Xi_g) \left[\prod_{k=1}^{dP^2} p(\varphi_{g,k} | \gamma_{g,k}\right] \left[\prod_{k=1}^{dP^2} p(\gamma_{g,k})\right]}\}$

3. Update c_g^1 from $c_g^1 \sim IG(\chi_g^1, \psi_g^1)$, with
   $\chi_g^1 = \frac{1}{2} n_g n_{(\gamma_g)} + a_g^1$
   $\psi_g^1 = \frac{1}{2} \sum_{s:\eta_s=g} (\beta_{g(\gamma_g)}^{(s)} - \varphi_{g(\gamma_g)})^T (\beta_{g(\gamma_g)}^{(s)} - \varphi_{g(\gamma_g)}) + b_g^1$
   where n_g is the number of trials in condition g, $n_{(\gamma_g)}$ is the number of non-zero values of γ_g, $\beta_{g(\gamma_g)}^{(s)}$ and $\varphi_{g(\gamma_g)}$ are the values corresponding to non-zero values of γ_g.

4. Update c_g^0 from $c_g^0 \sim IG(\chi_g^0, \psi_g^0)$, with
   $\chi_g^0 = \frac{1}{2} n_g n_{(\gamma_g^C)} + a_g^0$
   $\psi_g^0 = \frac{1}{2} \sum_{s:\eta_s=g} (\beta_{g(\gamma_g^C)}^{(s)} - \varphi_{g(\gamma_g^C)})^T (\beta_{g(\gamma_g^C)}^{(s)} - \varphi_{g(\gamma_g^C)}) + b_g^0$
   where $n_{(\gamma_g^C)}$ is the number of zero values of γ_g, $\beta_{g(\gamma_g^C)}^{(s)}$ and $\varphi_{g(\gamma_g^C)}$ are the values corresponding to zero values of γ_g.

5. Update p_g from $p_g \sim Beta(n_{(\gamma_g)} + \alpha_g^1, dP^2 - n_{(\gamma_g)} + \alpha_g^2)$

6. Update ξ_j, $j = 1, 2, ..., P$ from $\xi_j \sim IG(d_1, d_2)$